17. Site 852[1]

Shipboard Scientific Party[2]

HOLE 852A

Date occupied: 22 June 1991

Date departed: 22 June 1991

Time on hole: 8 hr, 25 min

Position: 5°17.566′N, 110°4.579′W

Bottom felt (rig floor; m, drill-pipe measurement): 3872.7

Distance between rig floor and sea level (m): 11.7

Water depth (drill-pipe measurement from sea level, m): 3861.0

Total depth (rig floor, m): 3878.5

Penetration (m): 5.8

Number of cores (including cores with no recovery): 1

Total length of cored section (m): 5.8

Total core recovered (m): 5.86

Core recovery (%): 101.0

Oldest sediment cored:
Depth (mbsf): 5.80
Nature: clayey foraminifer nannofossil ooze
Earliest age: Pleistocene

HOLE 852B

Date occupied: 22 June 1991

Date departed: 23 June 1991

Time on hole: 14 hr, 40 min

Position: 5°17.566′N, 110°4.579′W

Bottom felt (rig floor; m, drill-pipe measurement): 3871.6

Distance between rig floor and sea level (m): 11.7

Water depth (drill-pipe measurement from sea level, m): 3859.9

Total depth (rig floor, m): 4985.0

Penetration (m): 113.4

Number of cores (including cores with no recovery): 12

Total length of cored section (m): 113.4

Total core recovered (m): 119.68

Core recovery (%): 105.5

Oldest sediment cored:
Depth (mbsf): 113.4
Nature: clayey radiolarian nannofossil ooze
Earliest age: early/late Miocene

HOLE 852C

Date occupied: 23 June 1991

Date departed: 23 June 1991

Time on hole: 14 hr, 5 min

Position: 5°17.551′N, 110°4.562′W

Bottom felt (rig floor; m, drill-pipe measurement): 3871.5

Distance between rig floor and sea level (m): 11.7

Water depth (drill-pipe measurement from sea level, m): 3859.8

Total depth (rig floor, m): 3988.8

Penetration (m): 117.3

Number of cores (including cores with no recovery): 13

Total length of cored section (m): 117.3

Total core recovered (m): 125.59

Core recovery (%): 107.1

Oldest sediment cored:
Depth (mbsf): 117.3
Nature: radiolarian nannofossil ooze
Earliest age: early/late Miocene

HOLE 852D

Date occupied: 23 June 1991

Date departed: 24 June 1991

Time on hole: 1 day, 1 hr, 9 min

Position: 5°17.550′N, 110°4.537′W

Bottom felt (rig floor; m, drill-pipe measurement): 3871.5

Distance between rig floor and sea level (m): 11.7

Water depth (drill-pipe measurement from sea level, m): 3859.8

Total depth (rig floor, m): 3987.5

Penetration (m): 116.0

Number of cores (including cores with no recovery): 12

Total length of cored section (m): 114.0

Total core recovered (m): 120.56

Core recovery (%): 105.8

Oldest sediment cored:
Depth (mbsf): 116.0
Nature: radiolarian nannofossil ooze
Earliest age: early/late Miocene

Principal results: Site 852 (proposed Site WEQ-3) is the fifth of our seven-site north-south transect along 110° W. The site is presently located at the seasonal boundary between the westward-flowing South Equatorial Current (SEC) and the eastward-flowing North Equatorial Countercurrent (NECC). This site, along with other Leg 138 sites drilled along this

[1] Mayer, L., Pisias, N., Janecek, T., et al., 1992. *Proc. ODP, Init. Repts.*, 138: College Station, TX (Ocean Drilling Program).
[2] Shipboard Scientific Party is as given in list of participants preceding the contents.

transect, will provide material for detailed studies of the history of equatorial circulation and climate over the last 10 m.y. The transect also serves as the eastern end-member of a series of studies (Legs 85 and 130) aimed at understanding the regional and global response of the equatorial Pacific Ocean to changes in climate.

Four holes were drilled at Site 852. Hole 852A is a single APC mud-line core dedicated to whole-round geochemical and physical property measurements. Hole 852B was APC-cored to 113.4 mbsf before the final APC core struck what we assumed was the basement. Hole 852C was APC-cored to 110.5 mbsf, and we attempted one XCB core to sample the interval that had not been penetrated by Hole 852B. Then, Hole 852D was APC-cored to 116.0 mbsf. We completed a single logging run using the geochemical tool in Hole 852D. Analyses of continuous GRAPE density, susceptibility, and color reflectance measurements showed that 100% of the section was recovered.

The sedimentary sequence at Site 852 spans the interval from the uppermost middle Miocene to the Pleistocene and can be described as a single lithologic unit. Pliocene and Pleistocene sediments are characterized by a mixture of foraminifer nannofossil ooze and nannofossil foraminifer ooze with common oxide-rich beds, underlain by Miocene and early Pliocene radiolarian nannofossil ooze.

Sediments from the upper 79 m and in the interval from 110 mbsf to the base of the section display stable magnetic remanence. In the upper interval, the Brunhes Chron through the top of Chron C3A was identified, which provided chronostratigraphic control for the past 5 to 6 Ma. The lower interval was correlated with the interval in the paleomagnetic time scale from the upper part of Chron C4A to the upper part of Chron 5.

Biostratigraphic age control was provided by all four of the chief planktonic microfossil groups. Calcareous nannofossils are abundant and display good or moderate preservation throughout the section. Planktonic foraminifers are abundant or common, but are poorly preserved in the Pleistocene and upper part of the Pliocene. In the lower part of the section, their preservation is poor, and barren zones were observed. Radiolarians are common, with moderate to poor preservation in the Pleistocene and Pliocene. These are more abundant and better preserved in the upper and upper middle Miocene. Abundances of diatoms vary throughout the section and are rare to few in the Pliocene and rare to abundant in the Miocene.

Sedimentation rates at Site 852 continue the trend of reduced rates as we move farther north, away from the equatorial region. Sedimentation rates during the late Pliocene and Pleistocene were relatively constant and averaged about 12 m/m.y. As seen at all other sites along the 110° W transect, rates during the late Miocene and early Pliocene (8 to 4 Ma) were higher than during the younger interval. Rates during this period ranged from 15 to about 23 m/m.y. Within this interval of generally higher rates, the interval from 6.5 to 7.5 Ma shows a marked decrease to rates of 12 m/m.y. Sedimentation rates at the base of the site, between 8 and 10 Ma, reached the lowest levels observed at the site. The overall reduced sedimentation rates throughout the history of Site 852 are consistent with estimated paleolatitudes for this site, which suggests that the site was never within the equatorial high productivity region.

The calcium, silica, and iron profiles from the geochemical logging run showed that, like all other sites along the 110°W transect, the dominant variability in the sedimentary section was that of calcite content. However, at these reduced levels of biogenic sediment accumulation, the noncarbonate fraction is much less dominated by biogenic silica, and thus, clay minerals become a more important component of the sediment. While a large fraction of the hole was logged outside the pipe, further processing will be needed to better quantify the logging results.

Site 852 is the first of the western transect sites that had not crossed under the equatorial divergence. The site reflects this northerly position by having a reduced total sediment thickness and correspondingly reduced sedimentation rates. While these reduced rates make extremely high-resolution studies more difficult, the combination of reasonable sedimentation rates, magnetic stratigraphy, and the presence of all microfossil groups provided the data needed to define regional and depositional gradients and temporal changes in equatorial circulation during the late Neogene. Thus, as the paleoceanographic placer begins to thin, we still have a profitable show. At the conclusion of Leg 138 Site 852, paleomagnetists had completed 8.95 log(m^2kt).

BACKGROUND AND SCIENTIFIC OBJECTIVES

Site 852 is located in the eastward-flowing NECC, near the northern seasonal boundary between the SEC and the NECC (Fig. 1). Our primary objective for drilling at this site was to provide a record of the history of these currents and the relationship of their patterns to climatic forcing during most of the late Neogene.

Site 852 is located on crust that formed at the East Pacific Rise approximately 12.5 Ma. Using van Andel et al.'s (1975) pole of rotation, Site 852 originated at about 2°N (Fig. 2); using Duncan and Clague's pole of rotation (1985) describes a path that should show Site 852 originating at more than 3°N. In either case, the site has never been below the equator, a fact reflected in the relatively thin accumulation of sediment.

A detailed site survey for Site 852 was conducted as part of the *Thomas Washington* Venture 1 cruise (see "Site Surveys" chapter, this volume). The region is dominated by northwest-southeast-trending topography having about 300 to 400 m of relief (Fig. 3), a structure probably inherited from the ridge crest. The selected site is located on a northwest-southeast-trending topographic high having gentle basement and surficial relief. The pelagic sediment cover along the crest of the high is continuous and approximately 110 m thick. Thicker accumulations of sediment were found in several troughs surrounding the high (Fig. 4; e.g., 1020UTC 6 September), but these troughs probably contained redeposited material and thus were eliminated as potential drilling targets.

OPERATIONS

Transit to Site 852

The transit from Site 851 to Site 852 covered 142 mi over 12.5 hr at an average speed of 11.4 kt. At 0015 hr (all times reported in operations text are local times, L, where local time = Universal Time Coordinated, UTC, minus 7 hr; all times reported in Table 1 are in UTC) 22 June, the ship slowed to 6.6 kt, and the seismic gear was deployed for the site survey. A beacon was deployed on location at 0235L 22 June, and the survey was continued for 10 min past the site. The survey covered 17 nmi at an average speed of 5.9 kt. After the survey was completed, the seismic equipment was retrieved and returned to the site, where by 0315L 22 June, the thrusters and hydrophones had been lowered. The depth to seafloor, based upon the precision depth recorder (PDR), was 3875.4 mbrf.

Hole 852A

This first hole at the site consisted of a single mud-line core dedicated to whole-round geochemical and physical property measurements. While the drill string was being lowered, a hose supplying low-pressure air to the drawworks clutch parted, and operations were stopped for 1 hr while repairs were made. By 0915L 22 June, the hose had been replaced, and the pipe was lowered to the seafloor. After positioning the bit at 3869 mbrf, a single piston core was taken at 1130L 22 June (see Table 1 for a summary of coring operations). This core contained 5.86 m of sediment and helped to establish the mud line at 3872.7 mbrf.

Hole 852B

Core 138-852B-1H was recovered in a water depth of 3817 m and from it was retrieved 8.87 m of sediment, which established the mud line at 3871.6 mbrf. APC-coring advanced to 113.4 mbsf (Core 138-852B-13H), and orientation began with the fourth core. The piston did not fully extend for Core 138-852B-13H, presumably because of contact with basement. The core barrel was empty when it was

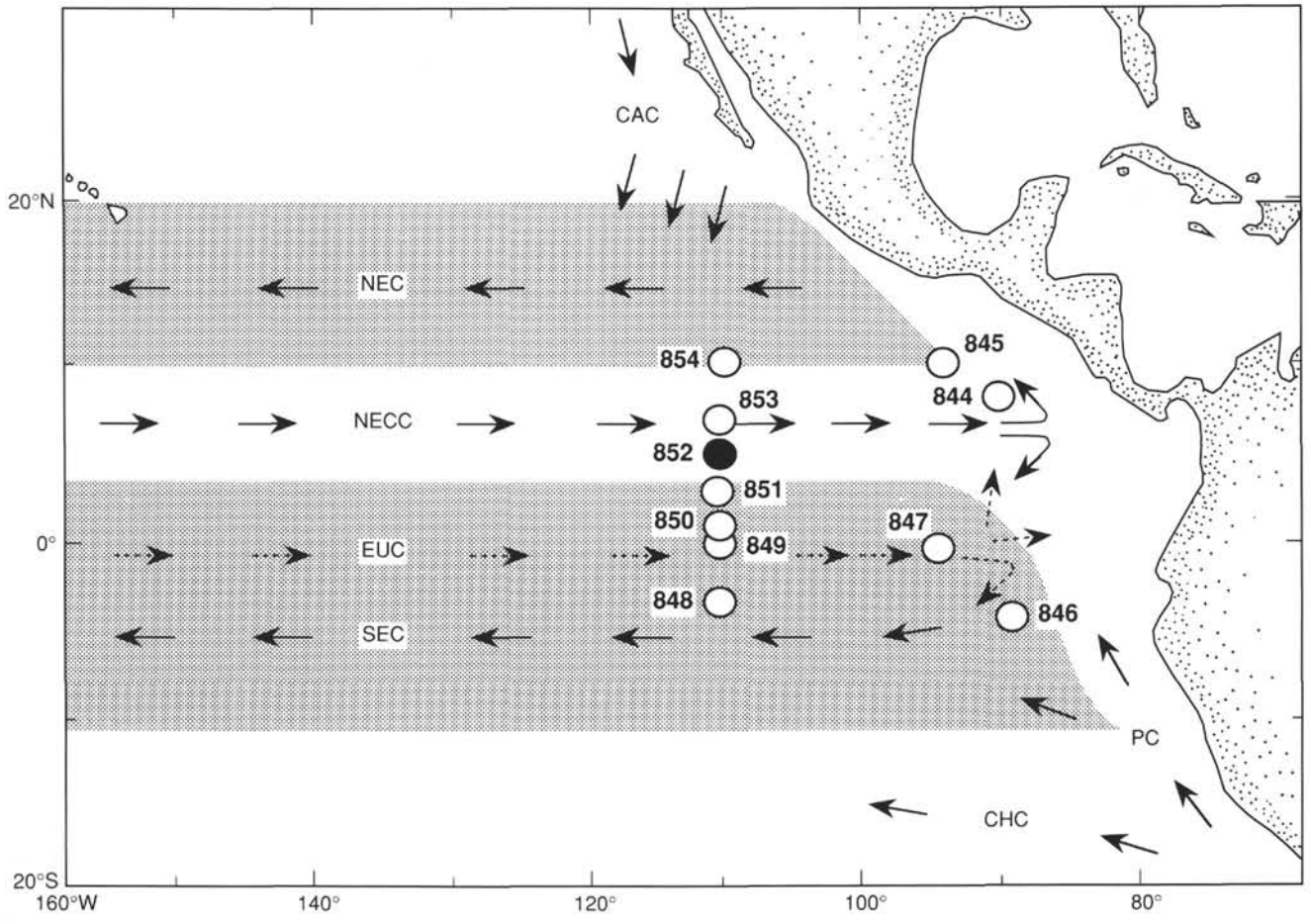

Figure 1. Location of Site 852 and generalized circulation system of the eastern equatorial Pacific Ocean. Other Leg 138 sites are shown for reference. Surface current shown as solid arrows, subsurface current as dashed arrows. CAC = California Current; NEC = North Equatorial Current; NECC = North Equatorial Countercurrent; EUC = Equatorial Undercurrent; SEC = South Equatorial Current; PC = Peru Current; and CHC = Chile Current. Shaded area illustrates general latitudinal extent of the SEC and NEC.

retrieved and thus could not be used to establish the depth of the sediment/basement interface. The coring program was terminated in Hole 852B at this point, then pipe was pulled out of the hole, with the bit clearing the mud line at 0140L 23 June (end of hole). Recovery for Hole 852B was 105.5%.

Hole 852C

Hole 852C was drilled to ensure that a continuous section was recovered and to provide enough material for high-resolution sampling. The vessel was offset 20 m south, and the bit was lowered to 3868 mbrf. Core 138-852C-1H was taken at 0240L 23 June, and from it was recovered 6.08 m of sediment, which established the mud line at 3871.5 mbrf for this hole. Piston-coring advanced to 110.5 mbsf (Core 138-852B-12H), and orientation began on the fourth core. At this point, the XCB-corer was run in the hole, because basement was less than 9 m from the base of the previous core.

The first 6 m of Core 138-852-13X was cut in 10 min, whereas the next 0.8 m took 30 min to advance. When the core barrel was retrieved, it contained 8.84 m of sediment, but no basement material. The coring program was terminated in Hole 852C at this point and the drill pipe was pulled out of the hole. The bit cleared the mud line at 1545L 23 June, ending Hole 852C. Recovery in the hole was 105.7% in the APC portion of the hole and 130% in the XCB section.

Hole 852D

Hole 852D was drilled to ensure that a continuous section was recovered and to provide enough material for high-resolution sampling. The ship was offset 20 m east, the bit was lowered to 3862 mbrf (2 mbsf), and Core 138-852D-1H was taken at 1650L 23 June. APC-coring advanced to 116.0 mbsf (Core 138-852D-12H), and orientation began on the fourth core. The depth objectives of the hole were reached after Core 138-852D-12H, and the hole was prepared for logging.

Logging of Hole 852D

The pipe was pulled to 77.7 mbsf for logging, and the hole was flushed with mud. Only the geochemical tool string was run because the hole was too short for the other tools (116.0 m total depth; Table 2). After being rigged up, the geochemical tool string was lowered down the pipe and, to avoid irradiating the section, the same GST calibration procedures as at Sites 850 and 851 were used.

The geochemical log was run with the heave compensator off, because it was not functioning properly. The hole was logged from 115.2 mbsf to the mud line. As at Site 851, the tool lost its calibration after entering the pipe (49.4 mbsf). Apparently, when the GST entered the pipe, the count rate decreased and feedback circuits raised the

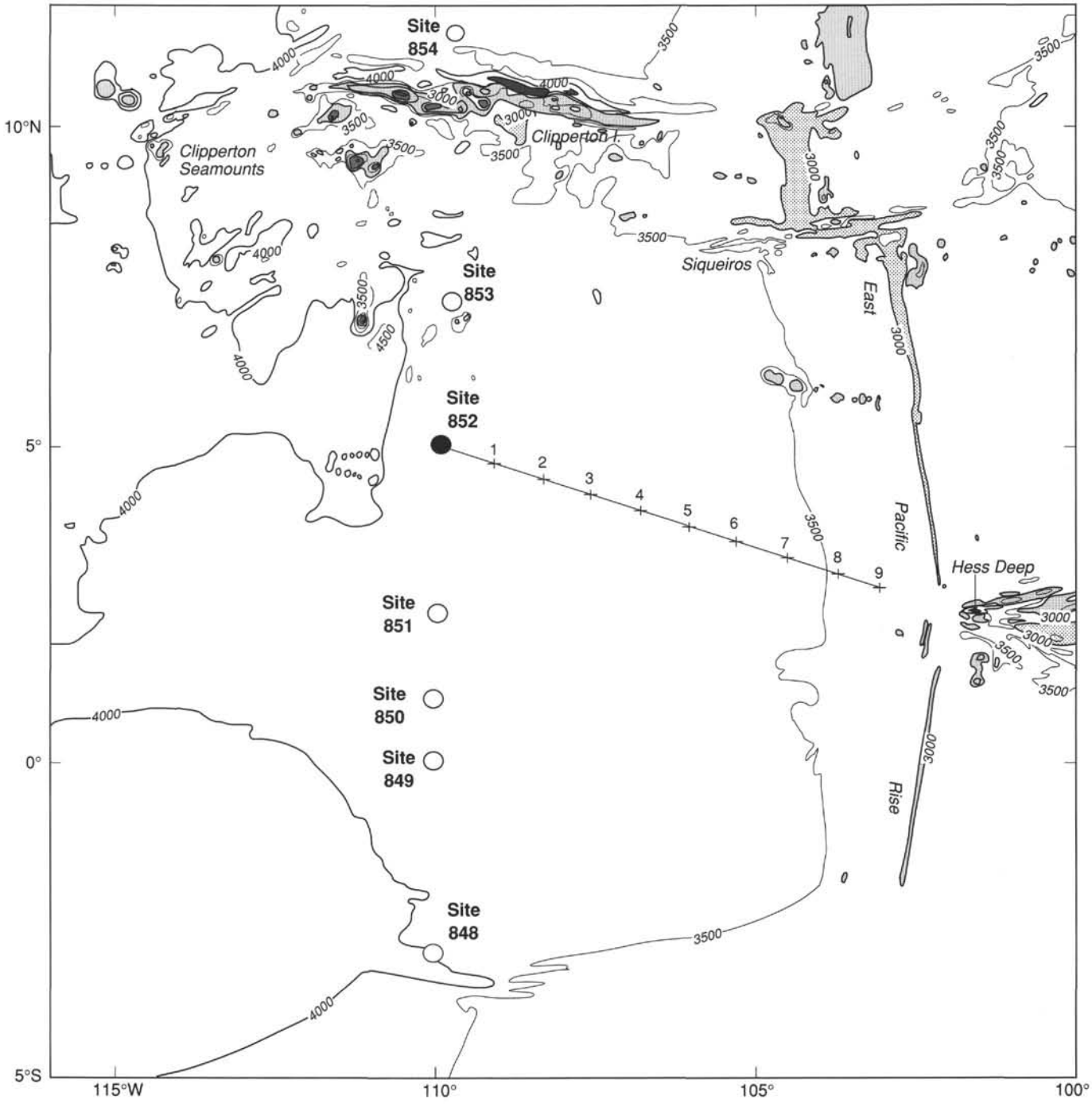

Figure 2. Generalized bathymetric map showing location of Site 852 and other Leg 138 sites drilled along the 110°W transect (from Mammerickx, 1989). Backtracked path for Site 852 (from van Andel et al., 1975) shown in 1- m.y. increments. Bathymetry in meters.

voltage of the accelerator for the neutron generator above its tolerance. Only a few meters of bad data were recorded before the problem was corrected and logging could continue from the base of the hole to the mud line. The tool was then brought on deck, and logging operations were concluded by 1045L 24 June.

After the drill floor was rigged down from logging, pipe was pulled out of the hole. The ship was offset while pipe was being pulled, and the commandable beacon was retrieved. The bit was brought on deck at 1615L, the rig floor secured for transit, hydrophones and thrusters raised, and the ship was under way toward the next site by 1645L 24 June.

LITHOSTRATIGRAPHY

Introduction

The sediments at Site 852 comprise Pliocene to Pleistocene foraminifer nannofossil and nannofossil foraminifer ooze with common oxide-rich beds, underlain by late Miocene to Pliocene nannofossil ooze and late Miocene radiolarian nannofossil ooze (Fig. 5). The sedimentary section above the basement was completely recovered.

The sediments at Site 852 were classified and divided into informal lithostratigraphic intervals primarily on the basis of visual core description, analysis of sediment composition obtained from smear

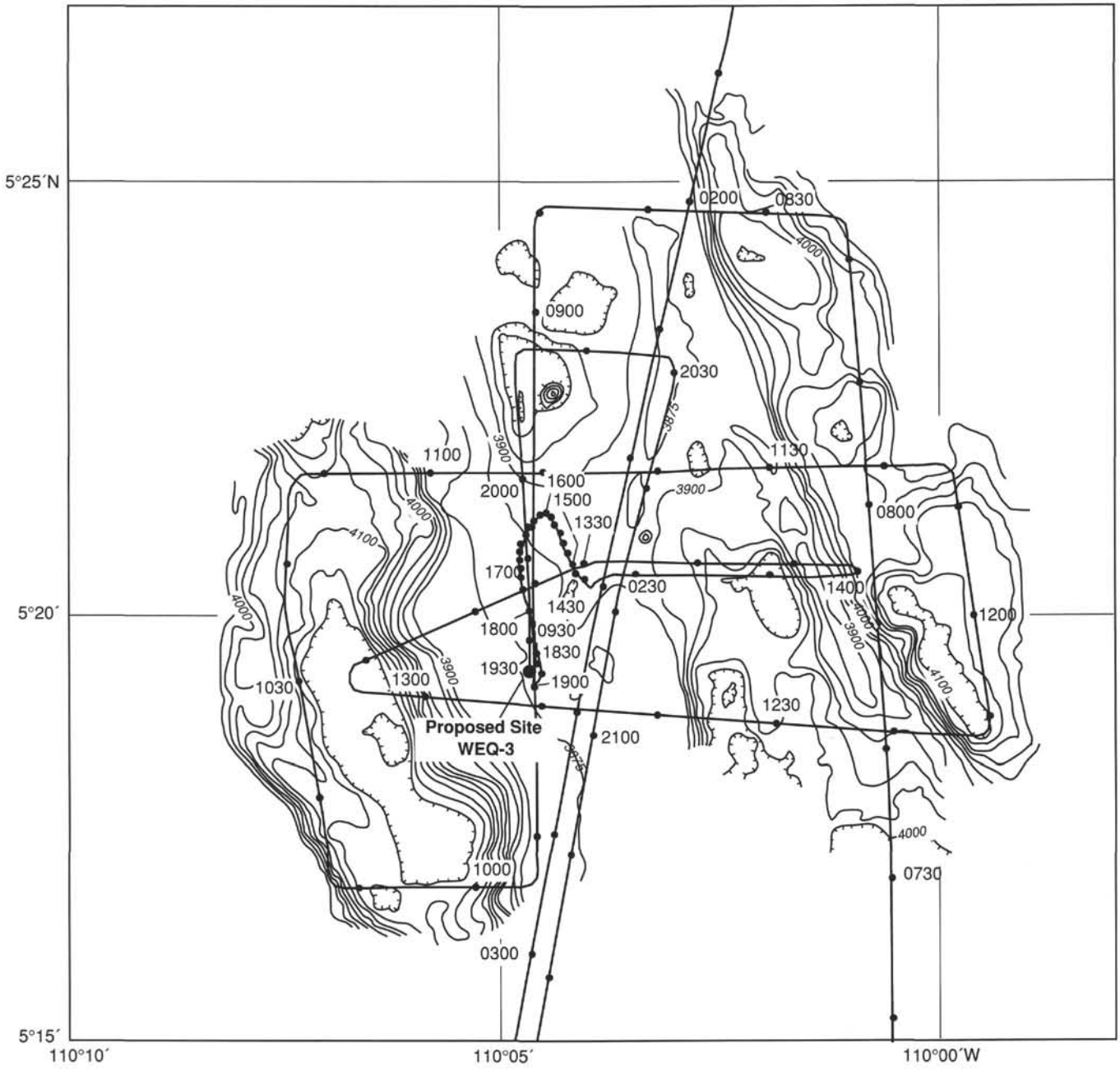

Figure 3. Hand-contoured SeaBeam map from navigation-adjusted SeaBeam contour maps collected from the *Thomas Washington* Venture 1 cruise, September 1989. Proposed Site WEQ-3 is shown.

slides (Fig. 6), and analysis of carbonate content. Other continuously measured parameters (including GRAPE density, magnetic susceptibility, automated color reflectance data and downhole logs) were used to characterize lithologies (Figs. 7 and 8). Fine-scale correlation among holes was conducted on the basis of matching continuous GRAPE density, magnetic susceptibility, and continuously measured color reflectance data, as well as on the basis of sedimentological features (see "Sedimentation Rates" section, this chapter). These multiparameter data also were used to identify coring gaps and overlaps among holes.

The sediments from Site 852 comprise one unit (Unit I), which has been divided into three intervals with characteristic lithologies (Table 3). The topmost interval (0–41.5 mbsf) is a foraminifer nannofossil ooze or nannofossil foraminifer ooze with oxide-rich beds. From 41.5 to 81 mbsf lies an interval of nannofossil ooze with foraminifers having common, dark, radiolarian-rich interbeds. From 81 to 117 mbsf, the dominant lithology is radiolarian nannofossil ooze with foraminifers from 80 to 107 mbsf, and radiolarian nannofossil ooze from 107 to 115 mbsf. The basal 2 m of sediment (115–117 mbsf) is devoid of siliceous microfossils.

Description of Units

Lithologic Unit I

Intervals:
Core 138-852A-1H
Cores 138-852B-1H through -12H-CC
Cores 138-852C-1H through -13X-CC

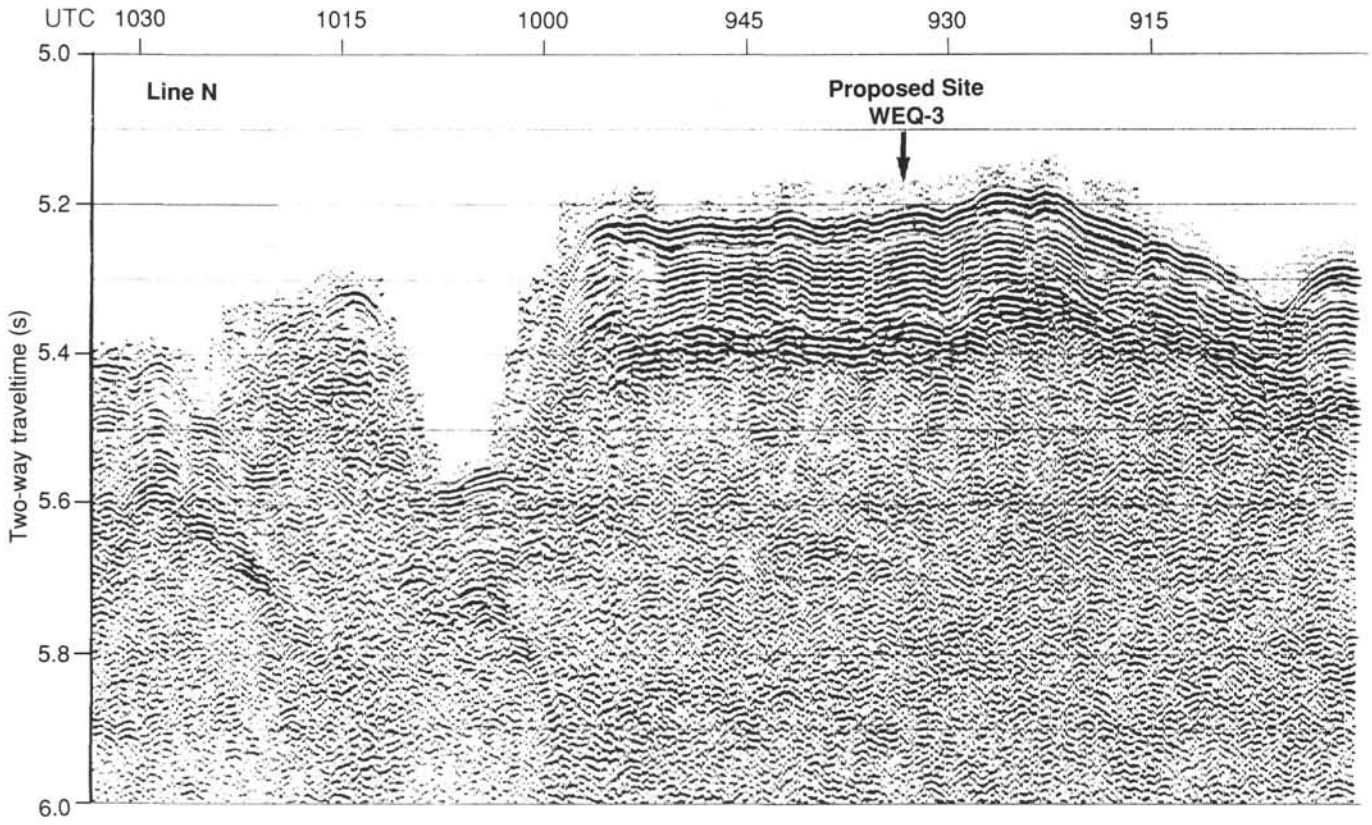

Figure 4. Analog seismic line collected with an 80-in.^{3} water gun during the *Thomas Washington* Venture 1 cruise. Proposed Site WEQ-3 is shown.

Cores 138-852D-1H through -12H-CC
Age: Pleistocene to late Miocene
Depth: 0–5.8 mbsf, Hole 852A; 0–113.4 mbsf, Hole 852B; 117.3 mbsf, Hole 852C; 0–116 mbsf, Hole 852D

The interval from 0 to 41.5 mbsf is characterized by a high abundance of foraminifers and by the intermittent presence of fine-grained Fe- and Mn-oxides. The dominant lithology varies from nannofossil foraminifer ooze to foraminifer nannofossil ooze. The top 1 m of sediment (Fig. 9) is clay-rich (20%–30%), but below this, clay is less abundant (0%–5%), other than in minor interbeds. Abundances of foraminifers from smear slide analyses vary and range from 30% to 60%, but decrease sharply at the base of the interval (Fig. 6). The dominant lithology varies from very pale brown (10YR 8/3) to dark, yellowish-brown (10YR 4/4), with increasing content of Fe- and Mn- oxides (typically 1%–5%). This color variation appears unrelated to the proportions of nannofossils and foraminifers.

Dark brown to very dark brown (10YR 3/3 to 10YR 2/2), 10- to 25-cm-thick interbeds, spaced 20 to 50 cm apart, are common throughout. These interbeds are rich in oxides (10%–50%) and, in the top 5 m, also rich in clay and radiolarians. Interbeds at the base of the interval also are clay-rich. Between 15 and 30 mbsf, a clear distinction in color is seen among the darker, oxide-rich beds. Those richer in Mn-oxides have a characteristic dark dusky red (10R 3/2) color, while those richer in Fe-oxides are dark brown to dark yellowish-brown (10YR 3/3 to 10YR 3/4). The lower boundary of the foraminifer nannofossil ooze interval was taken at the base of a group of dark yellowish-brown to very dark brown (10YR 3/3 to 10YR 2/2), clay-, oxide- and slightly more radiolarian-rich beds between 37 and 41.5 mbsf (Cores 138-852B-5H-1 to -5H-4, 35 cm; 138-852C-5H-2, 120 cm, to -5H-5, 100 cm; 138-852D-4H-6, 80 cm, to -5H-2, 20 cm). Within this zone, foraminifer contents decrease from 30% to 40% to 10% to 20%. This transition also is marked by low GRAPE (Fig. 7) and gravimetric bulk densities, high water contents (see "Physical Properties" section, this chapter), relatively low carbonate contents of 50% to 60% (see "Organic Geochemistry" section, this chapter), and a marked low percentage of reflectance (Fig. 8).

The dominant lithology between 41.5 and 82 mbsf is nannofossil ooze with foraminifers. Foraminifer content is typically within the range of 5% to 20%. Diatom content increases slightly from trace amounts above 41.5 mbsf to values of about 5% at the top of this interval (Fig. 6). Common, 10- to 20-cm-thick interbeds of radiolarian nannofossil ooze (about 15% radiolarians) occur that are more heavily burrowed than the surrounding sediments (Fig. 10). Between 41.5 and 50 mbsf, the spacing of the interbeds (which are also oxide-rich in this zone) is of the same order (20–50 cm) as the interbeds in the upper foraminifer-rich interval. However, below 50 mbsf, the spacing of the interbeds increases to 50 to 80 cm, although some more closely spaced bundles of interbeds have typical spacing of 30 cm (e.g., between 57 and 59 mbsf, Core 138-852C-7H-1, 2 cm), and a few interbeds occur between 75 and 80 mbsf.

From 41.5 to about 50 mbsf, colors range from very pale brown and light yellowish-brown (10YR 8/3 to 10YR 6/4) for the dominant lithology to a brown to pale brown (10YR 5/3 to 10YR 6/3) for the radiolarian-rich interbeds. At 50 mbsf, an abrupt color transition occurs below which the dominant lithology changes to a very light gray to light gray (N8 to 5Y 7/1), and the radiolarian-rich interbeds change from greenish-gray to light greenish-gray (5GY 6/1 to 5GY 7/1). This color change is associated with an increase in the blue percentage of reflectance values (see color section below).

At about 81 mbsf, the radiolarian content of the sediment increases significantly to about 10%. The radiolarian content continues to increase down the core and reaches values of 20% between 105 and 115 mbsf. Color changes abruptly at about 84 mbsf from light greenish-gray (5GY 7/1) to very pale brown (10YR 7/3). Disseminated Mn-oxides and dendrites are common between

Table 1. Summary of coring operations at Site 852.

Core no.	Date (June 1991)	Time (UTC)	Depth (mbsf)	Length cored (m)	Length recovered (m)	Recovery (%)
138-852A-1H	22	1830	0–5.8	5.8	5.86	101.0
Coring totals				5.8	5.86	101.0
138-852B-1H	22	1925	0.0–8.9	8.9	8.87	99.6
2H	22	2025	8.9–18.4	9.5	10.04	105.7
3H	22	2120	18.4–27.9	9.5	10.09	106.2
4H	22	2220	27.9–37.4	9.5	10.07	106.0
5H	22	2320	37.4–46.9	9.5	10.09	106.2
6H	23	0025	46.9–56.4	9.5	10.05	105.8
7H	23	0125	56.4–65.9	9.5	9.96	105.0
8H	23	0225	65.9–75.4	9.5	10.12	106.5
9H	23	0330	75.4–84.9	9.5	10.07	106.0
10H	23	0430	84.9–94.4	9.5	10.15	106.8
11H	23	0530	94.4–103.9	9.5	10.13	106.6
12H	23	0635	103.9–113.4	9.5	10.04	105.7
13H	23	0735	113.4–113.4	0.0	0.00	0.0
Coring totals				113.4	119.68	105.5
138-852C-1H	23	0940	0.0–6.0	6.0	6.08	101.0
2H	23	1040	6.0–15.5	9.5	10.08	106.1
3H	23	1130	15.5–25.0	9.5	9.63	101.0
4H	23	1235	25.0–34.5	9.5	10.11	106.4
5H	23	1340	34.5–44.0	9.5	10.08	106.1
6H	23	1440	44.0–53.5	9.5	10.13	106.6
7H	23	1540	53.5–63.0	9.5	10.13	106.6
8H	23	1640	63.0–72.5	9.5	10.14	106.7
9H	23	1735	72.5–82.0	9.5	10.08	106.1
10H	23	1830	82.0–91.5	9.5	10.09	106.2
11H	23	1930	91.51–101.0	9.5	10.09	106.2
12H	23	2030	101.01–110.5	9.5	10.11	106.4
13X	23	2200	110.51–117.3	6.8	8.84	130.0
Coring totals				117.3	125.59	107.1
138-852D-1H	23	2350	2.0–11.5	9.5	10.07	106.0
2H	24	0050	11.5–21.0	9.5	10.09	106.2
3H	24	0150	21.0–30.5	9.5	10.09	106.2
4H	24	0240	30.5–40.0	9.5	10.07	106.0
5H	24	0340	40.0–49.5	9.5	9.70	102.0
6H	24	0440	49.5–59.0	9.5	10.10	106.3
7H	24	0530	59.0–68.5	9.5	10.08	106.1
8H	24	0635	68.5–78.0	9.5	10.12	106.5
9H	24	0735	78.0–87.5	9.5	10.08	106.1
10H	24	0840	87.5–97.0	9.5	9.97	105.0
11H	24	0945	97.0–106.5	9.5	10.18	107.1
12H	24	1100	106.5–116.0	9.5	10.01	105.3
Coring totals				114.0	120.56	105.8

Table 2. Summary of logging operations at Site 852.

Date (June 1991)	Time (L)	Cumulative hours	Base of string (mbsf)	Comments
24	0400	0.0		Last core on deck.
24	0525	1.4		Start rig up.
24	0655	2.9		RIH w/geochem. string (NGT/ACT/GST/TLT).
24	0750	3.8	116.1	At TD; heave comp. left off; run out 20 ft slack. Calibrate while moving up slowly.
24	0757	3.9	115.2	GST-calibrated, start main log; no heave compensator.
24	0820	4.3	49.4	Enter pipe; GST briefly goes out of calibration again.
24	0836	4.6	0.0	Stop main log; POOH.
24	0950	5.8		Geochem. string at wellhead.
24	1045	6.8		Rigged down from logging.

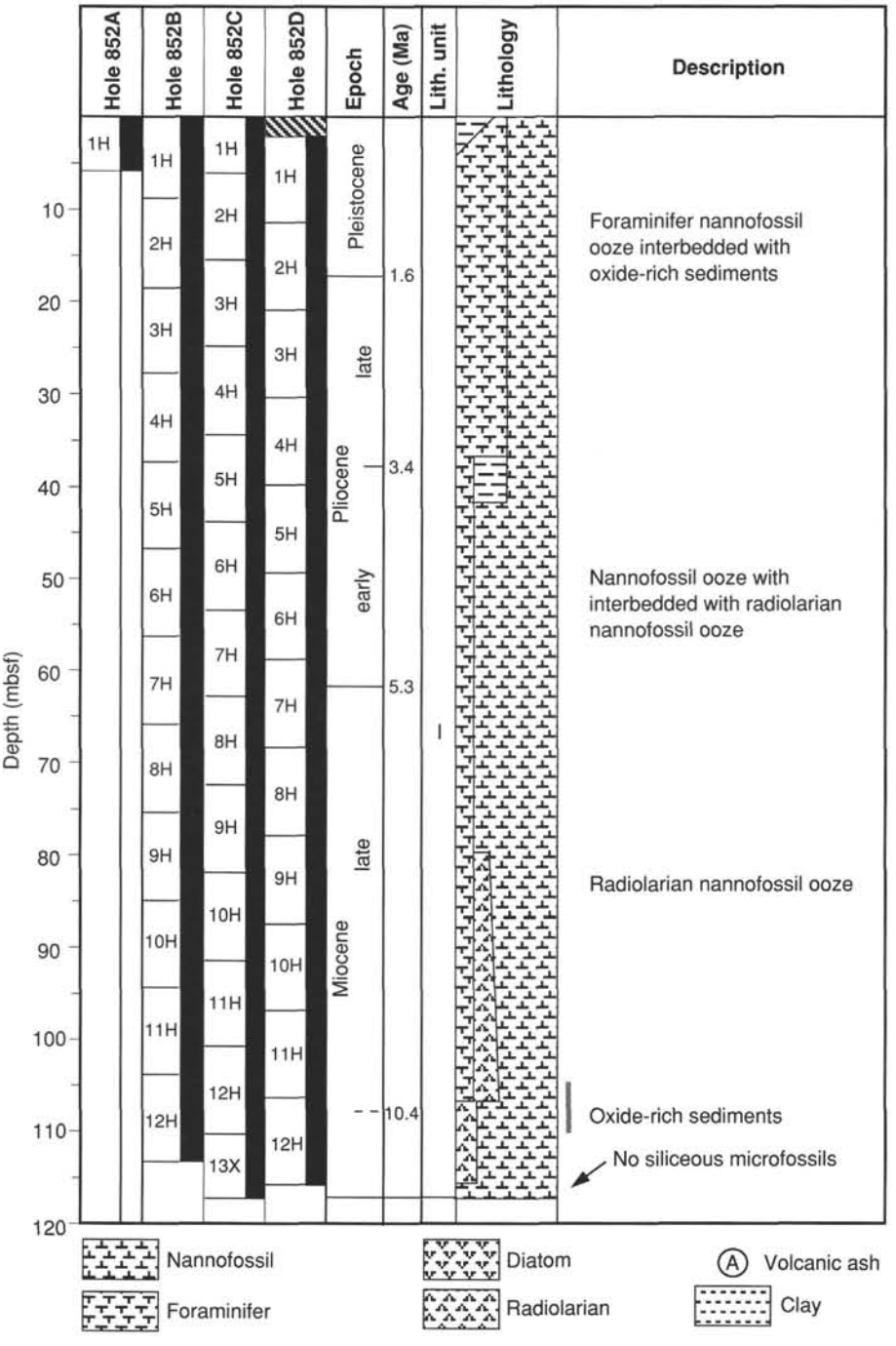

Figure 5. Lithostratigraphic summary of Site 852.

87 and 102 mbsf. From 90 to 100 mbsf, a number of pumice pods are present. Broken macrofossil (echinoderm?) fragments are present in Section 138-852B-10H-6 at 103 cm.

Between 103 and 110 mbsf, a series of darker beds is seen, and one distinctive, 40-cm-thick bed of very dark grayish-brown (10YR 3/2), oxide-rich (up to 25% Mn-oxides) radiolarian clay occurs at about 108 mbsf (Sections 138-852B-12H-3, 20 cm, -852C-12H-5, 130 cm, -852D-12H-1, 115 cm). This bed is highly bioturbated and contains well-preserved radiolarians. This interval has low carbonate contents (35%–65%) and GRAPE and gravimetric bulk densities. Foraminifer contents have been sharply reduced within this zone and remain low (0%–3%) to the base of the hole. Below these oxide-rich beds, the sediment is a light yellowish-brown to yellowish-brown (10YR 6/4 to 10YR 5/4), radiolarian nannofossil ooze having a radiolarian content of 15% to 20%. Between 101 and 116 mbsf, common pale burrow fills and bioturbated original horizons of nannofossil diatom ooze occur with strongly monospecific floras of the diatom *Thalassiothrix longissima*. The basal 2 m of sediment is nannofossil ooze with foraminifers and is barren of siliceous microfossils.

Trace Fossils

The intensity of bioturbation within the sediments recovered at Site 852 varies from strong, within and around the common darker interbeds, to very light in sections of pale sediment. Within the top 45 m, where darker, oxide-rich beds are common, bioturbation is moderate

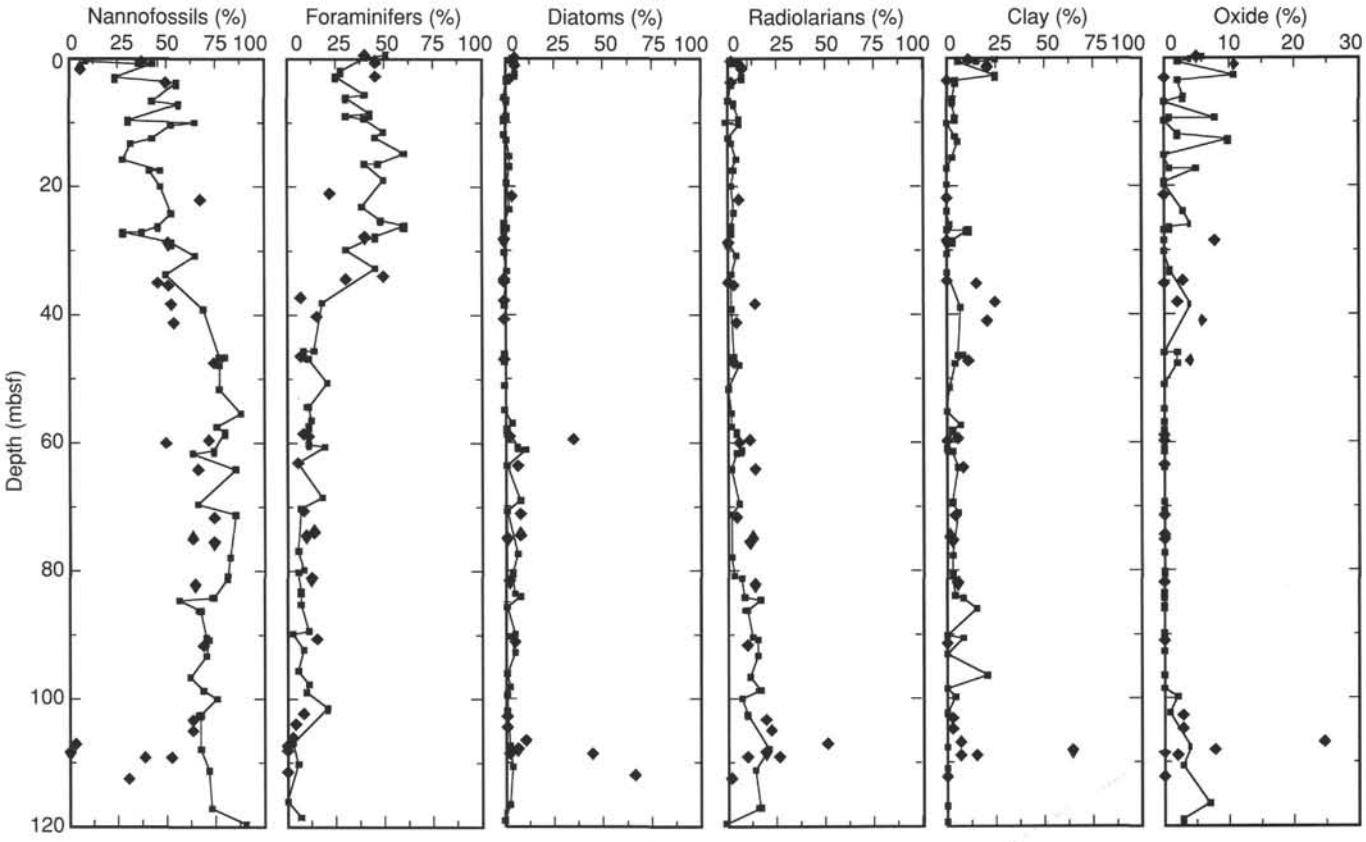

Figure 6. Summary of smear-slide analyses for Site 852. Squares joined with a line represent analyses of dominant lithologies; diamonds are minor lithologies.

to strong within the darker lithologies and light within the intervening paler sediment (Figs. 10, 11, and 12). Solid burrows are most abundant, with *Planolites* and rind burrows also common (Fig. 10). *Zoophycos* are common (Fig. 11), but the faint internal structure of the spreiten makes positive identification difficult. Isolated *Skolithos* burrows were observed throughout. *Chondrites* occurs more rarely and is mainly evident within burrow fills (Fig. 12).

Between 45 and 76 mbsf, bioturbation again is moderate to strong within darker radiolarian-rich interbeds and light within surrounding, paler lithologies. Solid burrows and *Planolites* are abundant, and *Skolithos* is common throughout (Fig. 13). *Chondrites* and *Zoophycos* (Fig. 13) are rare within this interval. A few, isolated, pyrite-rich burrows are present in the light gray to very light gray sediment between 65 and 80 mbsf. From 76 to 100 mbsf, only very slight bioturbation is evident in the very pale sediment. With the darkening of the sediment and the presence of interbeds from 100 mbsf, bioturbation is moderate to strong, with solid burrows, *Planolites*, rind burrows, and *Skolithos* common. Within the oxide- and clay-rich interval between 105 and 110 mbsf, *Chondrites* also is common, and *Zoophycos* was also observed. Below this interval to the base of the sequence, bioturbation is light to moderate, with only solid burrows and rind burrows common.

The principal differences between Site 852 and Sites 844 through 851 are the absence of open burrows (even at shallow depths) and the absence, other than in one restricted interval, of pyrite-rich burrows. The common preservation of *Skolithos* burrows indicates that levels of bioturbation were not strong. The apparent absence of bioturbation within intervals of paler sediment may in part result from the absence of color variation.

Color Reflectance Spectroscopy

The digital color reflectance data from Site 852 (Fig. 8) demonstrate strong short-period variability. The upper 50 m of the sedimen-

Table 3. Lithologic intervals at Site 852.

Lithology	Range	Depth (mbsf)	Age
Nannofossil foraminifer ooze and foraminifer nannofossil ooze	138-852A-1H 138-852B-1H to 5H-4, 35 cm 138-852C-1H to 5H-5, 100 cm 138-852D-1H to 5H-2, 20 cm	0–5.80, Hole 852A 0–42.25, Hole 852B 0–41.50, Hole 852C 0–41.50, Hole 852C	Pleistocene to late Pliocene
Nannofossil ooze with foraminifers	138-852B-5H-4, 35 cm to 9H-5, 46 cm 138-852C-5H-5, 100 cm to 9H-7, 65 cm 138-852D-5H-2, 20 cm to 9H-2, 37 cm	42–25-81.85, Hole 852B 41–50, Hole 852C 41–5-81.85, Hole 852D	late Pliocene to late Miocene
Radiolarian nannofossil ooze with foraminifers	138-852B-9H-5, 46 cm to 12H-CC 138-852C-9H-7, 65 cm to 13X-CC 138-852D-9H-2, 37 cm to 12H-CC	81–85-113.40, Hole 852B 82–0-117.30, Hole 852C 81–85-116.0, Hole 852D	late Miocene

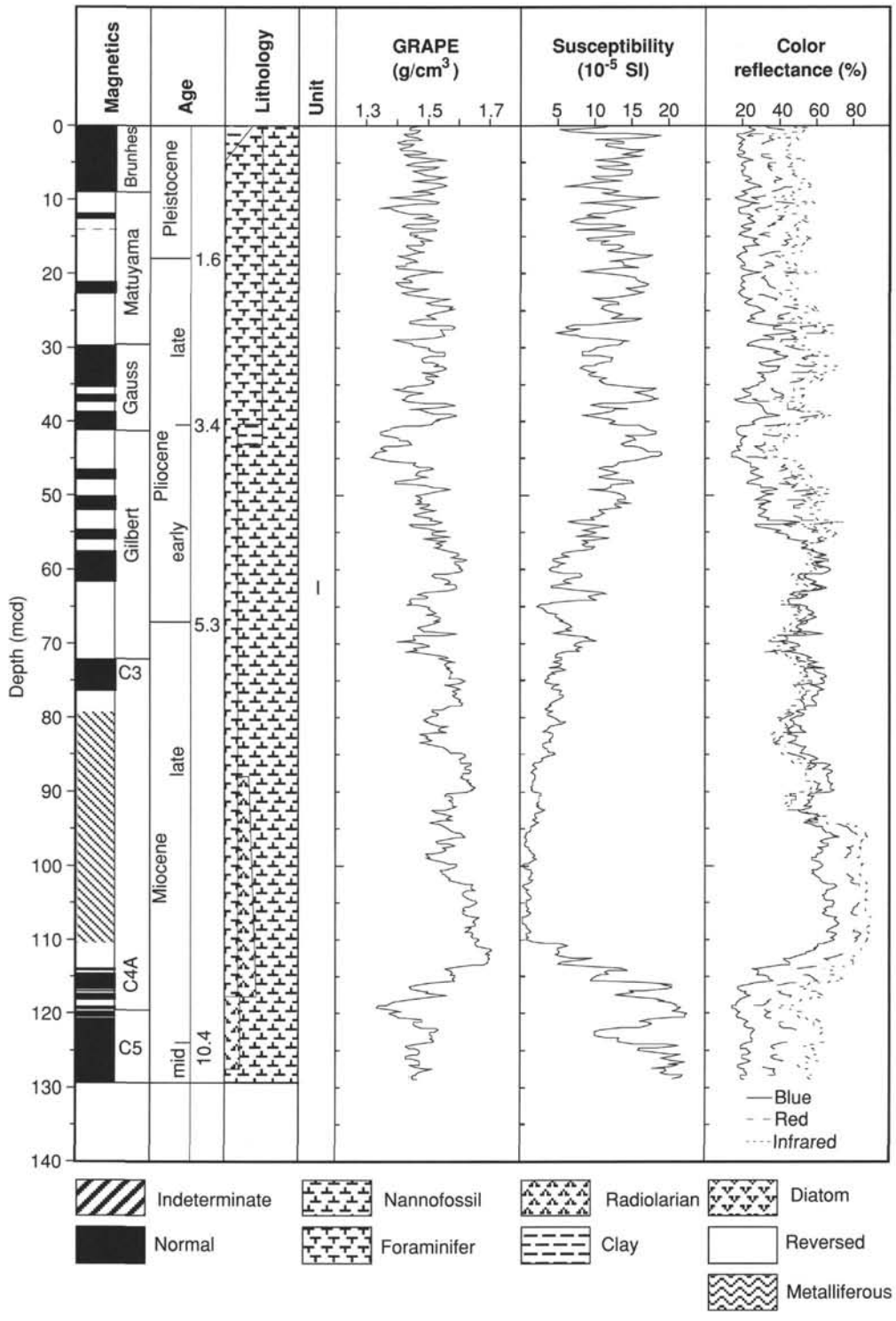

Figure 7. Composite summary of magnetics, age, graphic lithology, GRAPE, magnetic susceptibility, and percentage of color reflectance data for Site 852. Composite data consist of sections spliced together from multiple holes drilled at the site. Data are shown plotted vs. meters composite depth, the new depth scale used for constructing composite sections. GRAPE, susceptibility, and color data have been smoothed using a 20-point Gaussian filter.

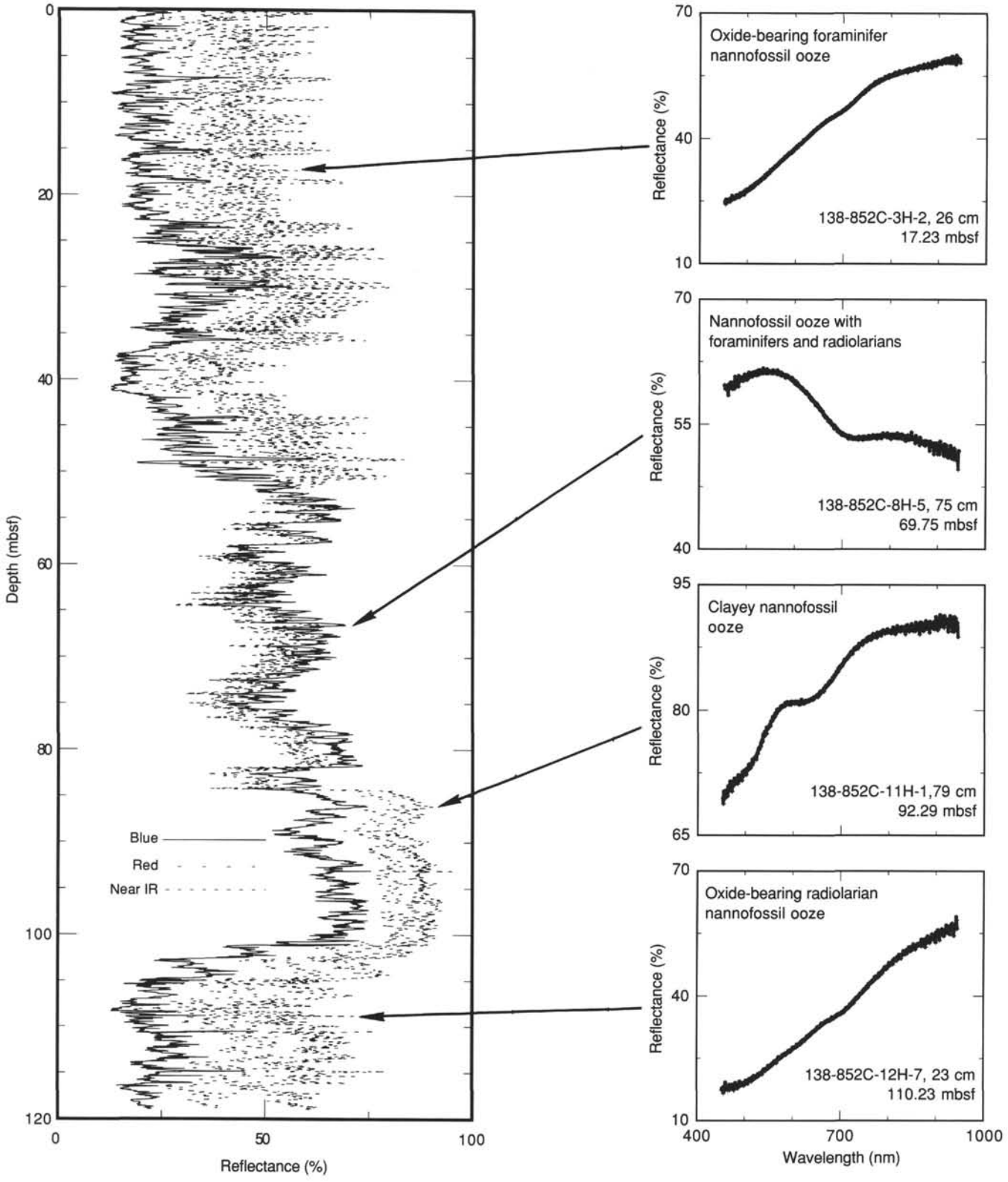

Figure 8. Percentage of reflectance of blue (450–500 nm; solid line), red (650–700 nm; dashed line), and near-infrared (850–900 nm; dotted line) color wavelength bands at Site 852 (left) with insets showing examples of color reflectance spectra for typical lithologies (right).

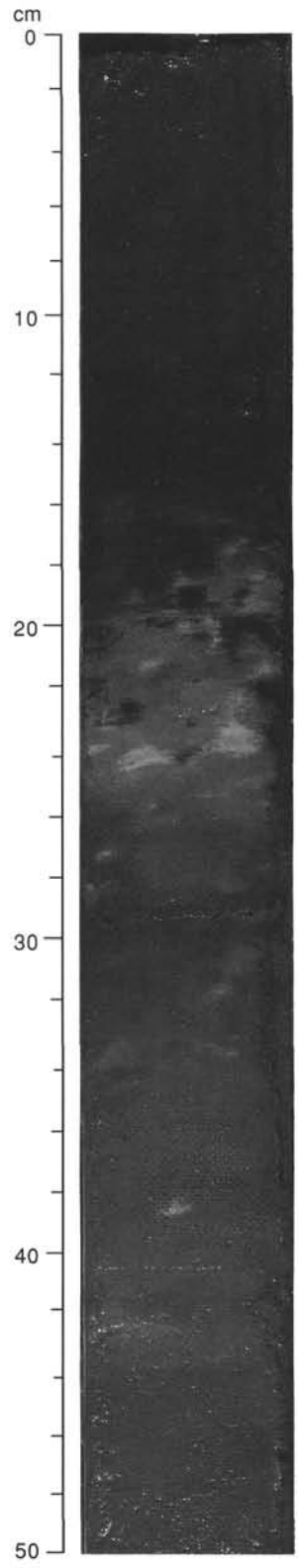

Figure 9. Topmost sediment recovered at Site 852 showing 15 cm of dark, Mn-oxide-rich, clayey nannofossil foraminifer ooze that grades down into paler, bioturbated, more nannofossil-rich sediment (Core 138-852B-1H-1, 0–50 cm).

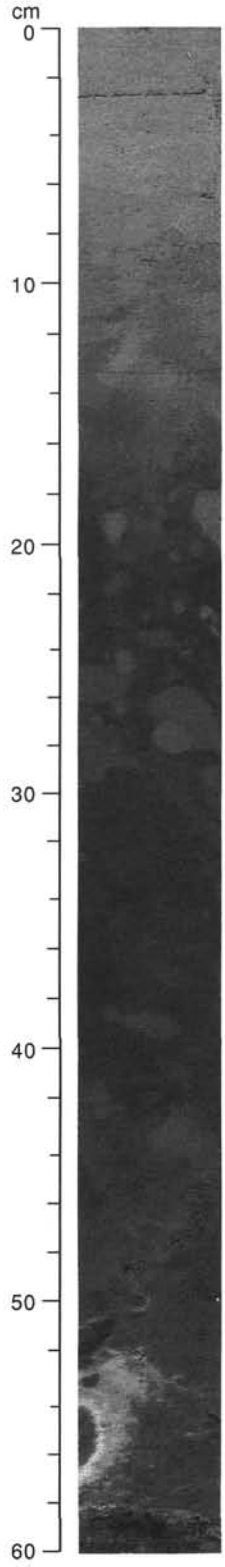

Figure 10. Darker, oxide-rich interbed within paler sediment showing significant bioturbation, including solid burrows, *Planolites,* and a rind burrow (Section 138-852B-2H-2 at 0–60 cm).

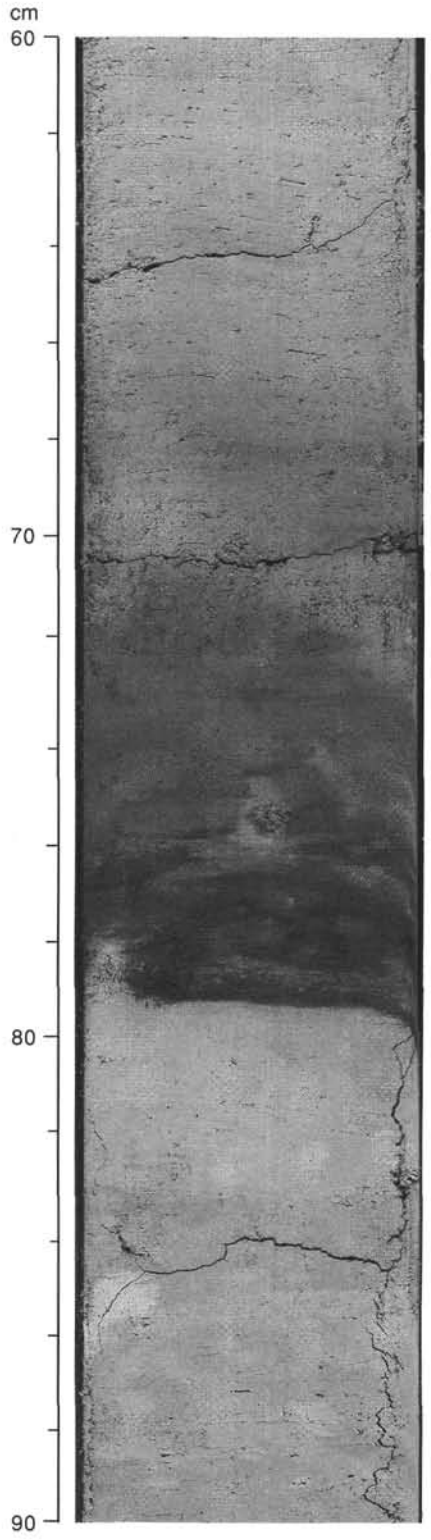

Figure 11. Darker, Mn-oxide-rich bed with *Zoophycos,* within paler foraminifer nannofossil ooze (Section 138-852B-4H-1 at 60–90 cm).

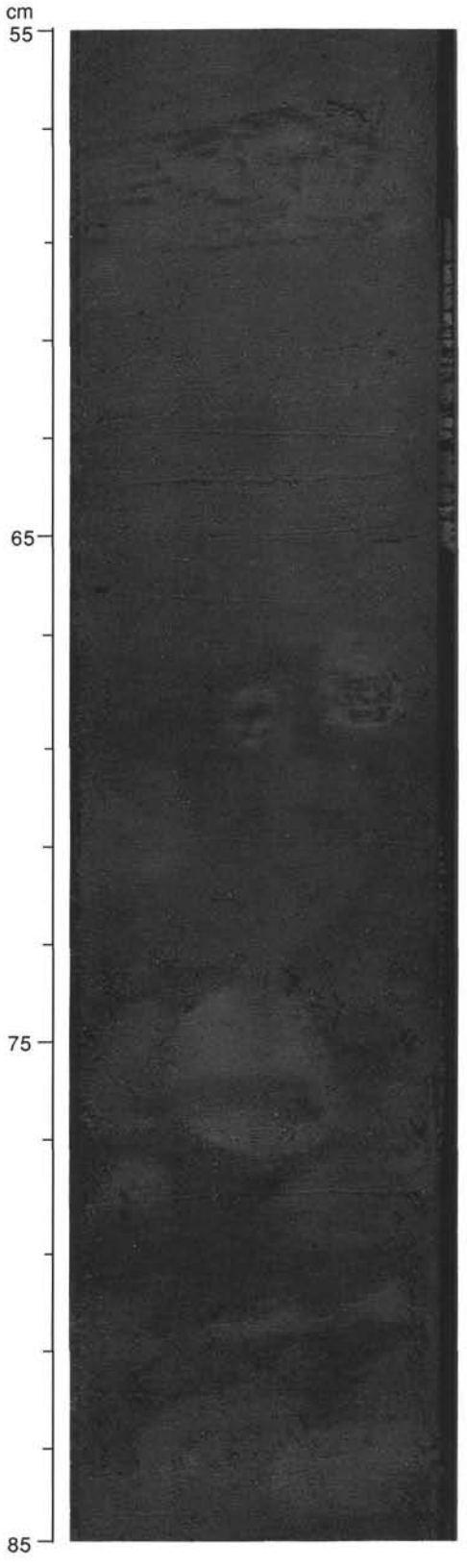

Figure 12. *Chondrites* within solid burrows in oxide-rich nannofossil foraminifer ooze (Section 138-852A-1H-2 at 55–85 cm).

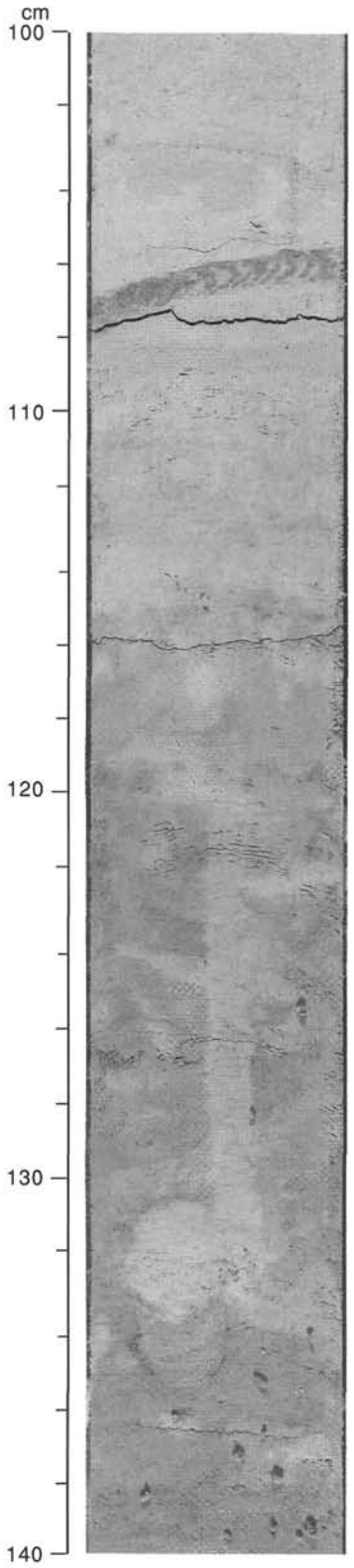

Figure 13. Single *Zoophycos* spreiten above a radiolarian-rich interbed with prominent *Skolithos* and solid burrows (Section 138-852C-8H-1 at 100–140 cm).

tary column has been dominated by this scale of change, with rhythmic interbedding of lighter and darker beds. All of this material has relatively high reflectance in the red and near-infrared bands, suggesting the presence of oxides. The interval from 51 to 82 mbsf is relatively pale and has blue reflectance percentages higher than red or near-infrared and contains sulfides. Oxides and clays are present below 82 mbsf. From 82 to 101 mbsf, the sediments are relatively reflective, especially in the near-infrared wavelengths. The example color spectrum (Fig. 8) for this interval, from 92.29 mbsf (Section 138-852C-11H-1 at 79 cm), contains relatively high yellow (600 nm) reflectance percentages, perhaps related to clays. Below 101 mbsf, the sediments are darker and apparently contain less $CaCO_3$ and more radiolarians and oxides.

Summary of Lithology

The sediments recovered at Site 852 are more clay-rich than those at Sites 848 through 851. Identification of clay in smear slides having high abundances of nannofossils proved difficult. However, the concentrations of aluminum recorded by the geochemical log were much greater than at the earlier sites (see "Downhole Measurements" section, this chapter), and the magnetic susceptibility signal was also substantially elevated (Fig 7). The sediments are highly variable and range from diatom-rich layers containing *Thalassiothrix longissima* to relatively pure nannofossil ooze and, in the younger section, rhythmically bedded nannofossil foraminifer ooze. Oxides are present through most of the sedimentary column, with the exception of the interval from 51 to 82 mbsf, where sulfides are present.

BIOSTRATIGRAPHY

A continuous sedimentary record representing the upper Pleistocene through the uppermost middle Miocene was recovered from the four Holes (852A to 852D) cored at Site 852. A well-constrained stratigraphy for this sequence is provided by calcareous nannofossils, planktonic foraminifers, radiolarians, and diatoms (Fig. 14). Here, we describe the biostratigraphic results from Holes 852B, 852C, and 852D, because only one core was recovered from Hole 852A (Pleistocene).

Abundances and preservation of the microfossil groups vary throughout the section. Calcareous nannofossils are abundant and exhibit good or moderate preservation throughout the section. Planktonic foraminifers are abundant or common and poorly preserved in the Pleistocene and Pliocene. In the Pliocene interval, their preservation is poor and their abundance varies between few to abundant, while some levels are barren. Radiolarians are common, with moderate to poor preservation in the Pleistocene/Pliocene interval. These are common to abundant in the upper to upper middle Miocene, with moderate to moderately good preservation. Abundances of diatoms vary throughout the sequence. Diatoms are rare to few in the Pliocene, rare to abundant in the Miocene, and generally absent in the lower part of the recovered sequence. Diatom preservation varies from poor to good.

A good magnetic stratigraphy was obtained from the Pliocene to lower upper Miocene sediments in Holes 852B and 852C. This stratigraphy will provide the means of calibrating selected microfossil datums and obtaining new biochronological data that can be compared with other data sets from low- and mid-latitude ocean basins.

The microfossil events recognized at Site 852 are reported in Tables 4 through 7, together with intervals of occurrence and subbottom depths.

In Figure 14, the epoch boundaries have been placed as follows:

Boundary	Hole	Depth (mbsf)	Event
Pleistocene/Pliocene	852B	20.15	Olduvai (t)
late/early Pliocene	852C	37.75	Gauss (o)
Pliocene/Miocene	852B	65.99	Gilbert (o)
late/middle Miocene	852D	114.80	B *Discoaster hamatus*

(t) = termination; (o) = onset;

Calcareous Nannofossils

Calcareous nannofossils recovered at Site 852 represent a stratigraphic succession from the upper Pleistocene (Zone CN14b from Okada and Bukry [1980] and NN20 from Martini [1971]) through the latest middle Miocene (Zones CN6 and NN8) (Fig. 14). Nannofossils are abundant and generally well or moderately well preserved throughout the entire sequence and provide a detailed and well-constrained biostratigraphy. Discoasterids and ceratolithids are common or abundant in the Pliocene and uppermost upper Miocene intervals (Cores 138-852B-2H through -9X). Discoasterids show moderate overgrowth in the

Table 4. Sample interval, ODP depth, and composite depth constraints of calcareous nannofossil events for Holes 852B, 852C, and 852D.

	Hole 852B			Hole 852C		
Event	Interval (cm)	Depth (mbsf)	Depth (mcd)	Interval (cm)	Depth (mbsf)	Depth (mcd)
T *Pseudoemiliania lacunosa*	1H-3,110–1H-4,60	4.10–5.10	4.40–4.50			
B *Gephyrocapsa* sp.3	2H-2,65–3H-2,140	11.05–11.80	11.30–12.05			
T *Gephyrocapsa* spp. >5.5 µm	2H-4,65–2H-4,140	14.05–14.80	14.30–15.05			
B *Gephyrocapsa* spp. >5.5 µm	2H-6,140–2H-7,40	17.80–18.3	18.05–18.55			
T *Calcidiscus macintyrei*	3H-1,65–3H-1,140	19.05–19.8	19.85–20.60			
B *Gephyrocapsa oceanica* s.l.	3H-1,65–3H-1,140	19.05–19.80	19.85–20.60			
T *Discoaster brouweri*	3H-2,65–3H-2,140	20.55–21.30	21.35–22.10			
T *Discoaster pentaradiatus*	2H-7,35–3H-CC	27.75–28.49	28.55–29.29			
T *Discoaster surculus*	4H-2,65–4H-2,140	30.05–30.80	32.45–33.20			
T *Discoaster tamalis*	4H-3,65–4H-3,140	31.55–32.30	33.95–34.70			
T *Sphenolithus* spp.	5H-1,80–5H-1,135	38.20–38.75	41.05–41.60			
T *Reticulofenestra pseudoumbilicus*	5H-2,80–5H-2,140	39.70–40.30	42.55–43.15			
BC *Discoaster asymmetricus*	5H-2,140–5H-3,30	40.30–40.70	43.15–43.55			
B *Ceratolithus rugosus*	6H-3,135–6H-4,35	51.25–51.75	56.20–56.70			
B *Ceratolithus acutus*	7H-1,71–7H-1,127	57.11–57.67	62.96–62.52			
T *Discoaster quinqueramus*	7H-3,75–7H-3,140	60.15–60.80	66.00–66.65			
B *Amaurolithus primus*	9H-6,140–9H-7,70	84.30–85.10	92.80–93.60			
B *Discoaster berggreni*	11H-1,40–11H-1,80	94.80–95.20	105.80–106.20			
B *Minylitha convallis*	12H-2,70–12H-2,110	106.10–106.50	118.30–118.70			
T *Discoaster hamatus*	12H-2,70–12H-2,110	106.10–106.50	118.30–118.70			
T *Coccolithus miopelagicus*				13X-5,40–13X-6,90	116.90–118.90	127.30–129.30
B *Discoaster hamatus*				13X-6,90–13X-CC	118.90–119.34	129.30–129.74

T = top occurrence; B = bottom occurrence.

Table 4 (continued).

	Hole 852D		
Event	Interval (cm)	Depth (mbsf)	Depth (mcd)
T *Pseudoemiliania lacunosa*			
B *Gephyrocapsa* sp.3			
T *Gephyrocapsa* spp. >5.5 µm			
B *Gephyrocapsa* spp. >5.5 µm			
T *Calcidiscus macintyrei*			
B *Gephyrocapsa oceanica* s.l.			
T *Discoaster brouweri*			
T *Discoaster pentaradiatus*			
T *Discoaster surculus*			
T *Discoaster tamalis*			
T *Sphenolithus* spp.			
T *Reticulofenestra pseudoumbilicus*			
BC *Discoaster asymmetricus*			
B *Ceratolithus rugosus*			
B *Ceratolithus acutus*			
T *Discoaster quinqueramus*			
B *Amaurolithus primus*			
B *Discoaster berggreni*			
B *Minylitha convallis*			
T *Discoaster hamatus*			
T *Coccolithus miopelagicus*	12H-6,80–12H-6,110	114.80–115.10	126.25–126.55
B *Discoaster hamatus*	12H-6,80–12H-6,110	114.80–115.10	126.55–126.55

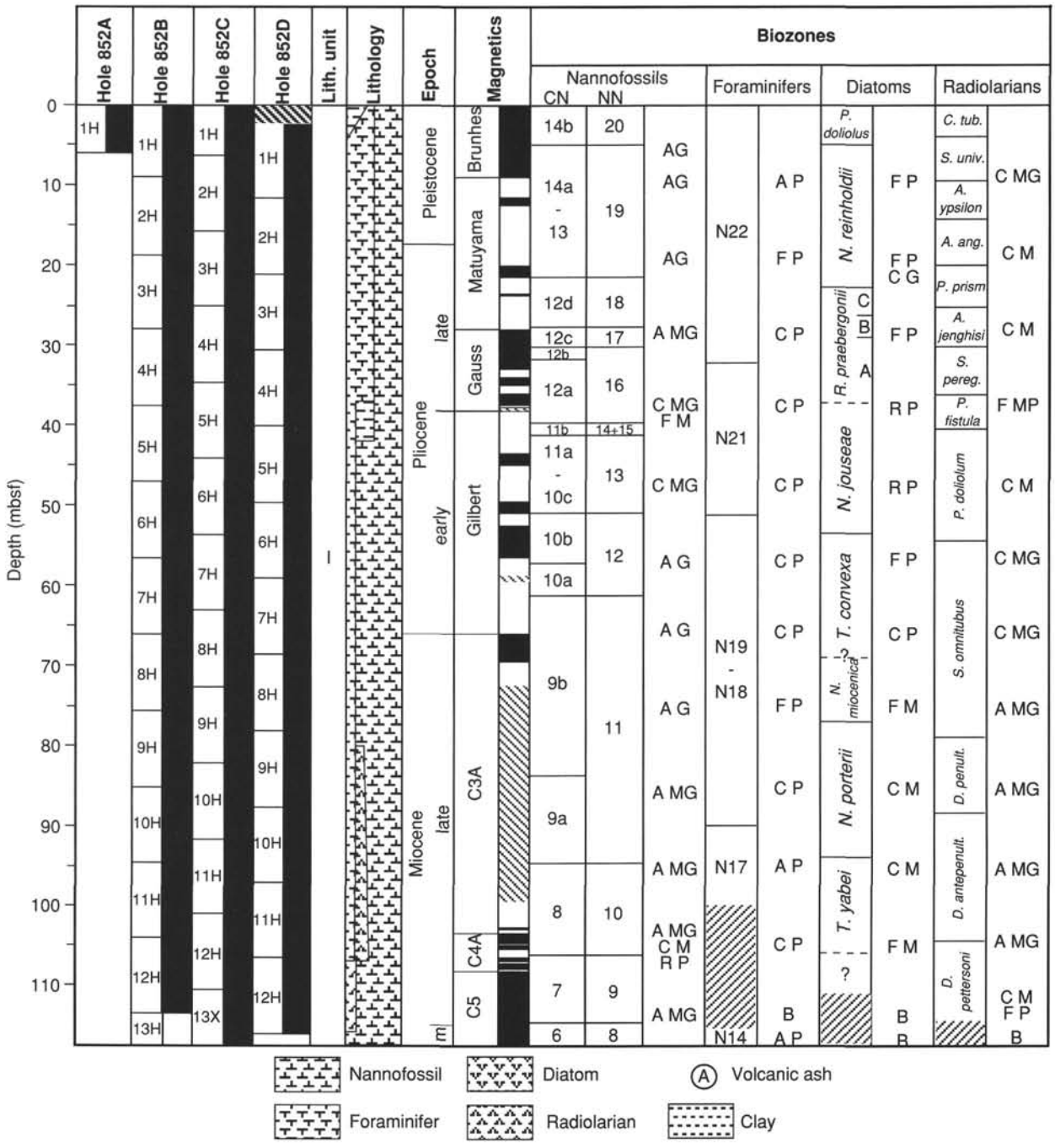

Figure 14. Biostratigraphic summary for Site 852. Depth in meters below seafloor (msbf). Hatched areas represent intervals where no zone could be assigned because of absence of marker species. Dashed lines represent uncertainty in placement of zonal boundary. Microfossil abundance is recorded as A = abundant; C = common; F = few; R = rare; B = barren. Microfossil preservation is recorded as G = good; M = moderate; MG = moderate to good; P = poor. This is a general overview of biostratigraphic results at Site 852. Data presented in the figure are based, in general, on results from Hole 852B. Placement of specific stratigraphic boundaries may differ slightly among Holes 852B, 852C, and 852D.

lowermost upper Miocene interval (Cores 138-852B-10H through -13H). Etching on placoliths was observed in some samples from the Pleistocene–Pliocene interval (Cores 138-852B-1H through -7H). In the upper Miocene interval, strong dissolution of the nannofossil assemblage was observed in Core 138-852B-12H. Also in this interval, some samples were barren of calcareous nannofossils. Common reworked nannofossils from the upper Miocene Zone CN9 to CN6 (NN11 to NN9) are present in samples from the Pleistocene and Pliocene intervals (Cores 138-852B-3H through -10H).

The nannofossil events recognized in the Site 852 succession are reported in Table 4. The identification of these events has been based on closely spaced samples (three samples per section), owing to the relatively low sedimentation rate at Site 852.

In the Pleistocene interval (Cores 138-852B-1H through -3H), the calcareous nannofossil assemblage is characterized by different morphotypes of *Gephyrocapsa* spp., helicoliths, *Pseudoemiliania lacunosa,* small reticulofenestrids, and *Calcidiscus* spp. The first occurrence of *Gephyrocapsa oceanica* s.l. was recorded between

Samples 138-852B-3H-1, 65 cm, and -3H-1, 120 cm, and approximates the Pleistocene/Pliocene boundary, placed at the top of the Olduvai. The last occurrence of *Discoaster brouweri* was recorded between Samples 138-852B-3H-2, 65 cm, and -3H-2, 140 cm, at the base of the Olduvai.

The Pliocene interval (Cores 138-852B-3H through -6H) is characterized by rich and well-preserved assemblages having common to abundant *Reticulofenestra* spp., *Calcidiscus* spp., *Coccolithus pelagicus,* discoasterids, helicoliths, ceratolithids, and sphenolithids in the lower Pliocene interval. The last occurrence of *Reticulofenestra pseudoumbilicus,* which approximates the upper/lower Pliocene bound-ary, was recorded between Samples 138-852B-5H-2, 80 cm and -5H-2, 140 cm.

The last occurrence of *Discoaster quinqueramus,* which approximates the Pliocene/Miocene boundary, was recorded between Samples 138-852B 7H-3, 75 cm, through -7H-3, 140 cm, and marks the CN10a/CN9b (NN12/NN11) zonal boundary.

A rich and diverse assemblage of discoasterids characterizes the upper Miocene interval. Ceratolithids occur throughout the interval and are represented by *Amaurolithus primus, A. delicatus,* and *A. amplificus.* The first occurrence of *A. primus* is recorded between Samples 138-852B-9H-6, 140 cm, and -9H-7, 70 cm. The first occurrence of *Discoaster berggreni* is recorded between Samples 138-852B-11H-1, 40 cm, and -11H-1, 80 cm, and represents the base of Subzone CN9a (Zone NN11). *Discoaster quinqueramus* and *D. berg-greni* are common throughout their stratigraphic range (Zones CN9 and NN11).

The last occurrence of *Discoaster hamatus* was recorded between Samples 138-852B-12H-2, 70 cm, and -12H-2, 110 cm, and marks the CN8/CN7 (Zone NN9/NN10) zonal boundary. The first occurrence of *D. hamatus,* which approximates the upper/middle Miocene boundary and the base of Zone CN7 (Zone NN9), was recorded between Samples 138-852C-13H-6, 90 cm, and -13X-CC, and -852D -12H-6, 80 cm, and 12H-6, 110 cm.

The lowermost part of the Site 852 sequence (Sample 138-852B-13H-CC) was placed in the latest middle Miocene Subzone CN6 (Zone NN8). Common specimens of *Catinaster coalitus* and *Coccolithus miopelagicus* were recorded in this sample.

Planktonic Foraminifers

Preservation of planktonic foraminifers is poor throughout the sedimentary sequence retrieved from Hole 852B. These are common to abundant in Cores 138-852B-1H-CC through -6H-CC and exhibit a high degree of fragmentation. In several intervals, the assemblages consist almost entirely of the robust species, *Globorotalia tumida,* along with numerous keel fragments of this species. Below Sample 138-852B-6H-CC, abundances of planktonic foraminifers become highly variable. Foraminifers are few in Sample 138-852B-8H-CC, common in Samples 138-852B-7H-CC, -9H-CC, and -11H-CC, and abundant in Samples 138-852B-10H-CC and -13H-CC. Sample 138-852B-12H-CC is barren.

The dominant components of the coarse fraction residues are foraminifers from Cores 138-852B-1H through -6H and radiolarians from Cores 138-852B-7H through -12H. Other consistent coarse-fraction components in Cores 138-852B-4H through -13H are rare to few echinoid spines (common in Samples 138-852B-7H-CC and -11H-CC) and sponge spicules (common in Sample 138-852B-12H-CC). Volcanic glass is rare in Sample 138-852B-11H-CC and abundant in Sample 138-852B-12H-CC. Manganese micronodules are common throughout the lowest stratigraphic interval from Sample 138-852B-10H-CC through -13H-CC.

Planktonic foraminiferal datums identified in the sequence are given in Table 5. The base of Pleistocene Zone N22 has been equated to the last occurrence of *Globorotalia limbata* in Sample 138-852B-3H-CC and the base of upper Pliocene Zone N21 to the last occurrence of *Sphaeroidinellopsis* spp. in Sample 138-852B-5H-CC. The first occurrence of *Globorotalia tumida* in Sample 138-852B-9H-CC marks the base of lower Pliocene Zone N18. Sample 138-852B-10H-CC, which contains *Globorotalia plesiotumida* and *Neogloboquadrina acostaensis,* was assigned to Zone N17. Cores 138-852B-11H and -12H were placed in an unzoned interval. Sample 138-852B-11H-CC yielded a dissolved assemblage containing mainly the robust forms *Globoquadrina venezuelans* and *Sphaeroidinellopsis* spp. Sample 138-852B-12H-CC is barren of planktonic foraminifers. The presence of *Globorotalia siakensis* in Sample 138-852B-13H allowed us to assign the sediments just above the basement to the uppermost middle Miocene Zone N14.

Radiolarians

Radiolarians sampled in Site 852 range in age from the Quaternary (*Collosphaera tuberosa* Zone) to the late middle Miocene (*Diartus pettersoni* Zone). The most recent radiolarian zone (*Buccinosphaera invaginata*) was not identified. The oldest material recovered that could be identified to the zonal level (*D. pettersoni* Zone) is from Sample 138-852C-13X-5, 110 cm.

Preservation of radiolarians is no better than moderately good in samples from this site. Within the Pleistocene–Pliocene section, radiolarians are common, but their preservation is generally moderate or poor to moderate. Reworking of older radiolarians (upper Miocene) into the Pleistocene–Pliocene part of the section was found in most samples from Cores 138-852B-1H through -6H. This section may be complete, however, with all the major zones and radiolarian datums recognized in the samples studied (Table 6). Occurrences of *Spongaster pentas* and *S. berminghami* were scattered at this site, making it impossible for us to use the first and last occurrences of these species for correlation with other sites. The occurrence of *Acrobotrys tritubus* is more consistent at this site than at others, but because of its scattered occurrence at other sites, its first and last appearances cannot be used as reliable datums for correlation.

Radiolarians were common to abundant in the upper to upper middle Miocene part of the section, and preservation was generally moderate or moderately good. Below Core 138-852B-12X preservation decreases somewhat and the section becomes barren of siliceous microfossils in and below Sample 138-852C-13X-6, 110 cm. The oldest reliable datum (Table 6) is the last appearance of *Cyrtocapsella japonica* (between Samples 138-852-12X-4, 110 cm, and -12X-5, 110 cm). This datum has an estimated age of 9.0 Ma (±0.1) in the central Pacific Ocean Site

Table 5. Sample, ODP depth, and composite depth constraints of planktonic foraminifer events for Hole 852B.

	Hole 852B		
Event	Interval	Depth (mbsf)	Depth (mcd)
T *Globorotalia limbata*	2H-CC–3H-CC	18.94–28.49	19.19–29.29
T *Sphaeroidinellopsis* spp.	4H-CC–5H-CC	37.97–47.49	40.37–50.34
B *Globorotalia tumida*	9H-CC–10H-CC	85.47–95.05	93.97–105.05
T *Neogloboquadrina siakensis*	12H-CC–13H-CC	113.94–113.40	126.14–113.40

T = top occurrence; B = bottom occurrence.

Table 6. Sample, ODP depth, and composite depth constraints of radiolarian events for Holes 852B, 852C, and 852D.

	Hole 852B			Hole 852C		
Event	Interval	Depth (mbsf)	Depth (mcd)	Interval	Depth (mbsf)	Depth (mcd)
T *Stylatractus universus*	1H-2–1H-4	2.8–5.8	2.6–5.6			
B *Collosphaera tuberosa*	1H-6–1H-CC	8.8–9.076	8.6–8.87			
T *Lamprocyrtis neoheteroporos*	2H-3–2H-4	13.25–14.75	13–14.5			
T *Anthocyrtidium angulare*	2H-3–2H-4	13.25–14.75	13–14.5			
T *Theocorythium vetulum*	2H-3–2H-4	13.25–14.75	13–14.5			
B *Lamprocyrtis nigriniae*	2H-3–2H-4	13.25–14.75	13–14.5			
B *Theocorythium trachelium*	2H-CC–3H-1	19.19–20.3	18.94–19.5			
B *Pterocorys minythorax*	2H-4–2H-6	14.75–17.75	14.5–17.5			
B *Anthocyrtidium angulare*	3H-1–3H-3	20.3–21.84	19.5–22.5			
T *Pterocanium prismatium*	3H-1–3H-3	20.3–21.84	19.5–22.5			
T *Lamprocyrtis heteroporos*	2H-4–2H-6	14.75–16.88	14.5–17.5	1H-CC–2H-CC	6.08–16.08	6.08–16.88
T *Anthocyrtidium jenghisi*	3H-4–3H-6	26.53–27.8	24–27	3H-CC–4H-CC	25.13–35.11	26.53–36.31
B *Theocalyptra davisiana*	3H-6–3H-7	27.8–28.41	27–27.61			
T *Stichocorys peregrina*	4H-1–4H-2	31.4–32.9	29–30.5			
T *Anthocyrtidium pliocenica*	4H-6–4H-CC	38.9–40.37	36.5–37.97			
B *Lamprocyrtis neoheteroporos*	4H-4–4H-6	36.31–38.9	33.5–36.5	4H-CC–5H-CC	35.11–44.58	36.31–48.08
B *Lamprocyrtis heteroporos*	4H-4–4H-6	36.31–38.9	33.5–36.5	4H-CC–5H-CC	35.11–44.58	36.31–48.08
T *Phormostichoartus fistula*	4H-6–4H-CC	38.9–40.37	36.5–37.97			
T *Lychnodictyum audax*	5H-1–5H-2	41.35–42.47	38.5–40			
T *Spongaster pentas*	5H-3–5H-4	44.35–45.85	41.5–43			
T *Phormostichoartus doliolum*	5H-3–5H-4	44.35–45.85	41.5–43			
B *Amphirhopalum ypsilon*	5H-3–5H-4	44.35–45.85	41.5–43			
B *Spongaster tetras*	5H-5–5H-6	47.35–48.85	44.5–46			
T *Didymocyrtis penultima*	5H-4–5H-5	45.85–47.35	43–44.5			
B *Pterocanium prismatium*	6H-4–6H-5	57.45–58.95	52.5–54			
T *Spongaster berminghami*						
B *Spongaster pentas*	6H-5–6H-6	58.95–59.13	54–55.5	5H-CC–6H-CC	44.58–54.13	48.08–59.13
T *Solenosphaera omnitubus*	6H-5–6H-6	58.95–59.13	54–55.5	5H-CC–6H-CC	44.58–54.13	48.08–59.13
T *Siphostichartus corona*	7H-3–7H-4	66.14–67.64	60.29–61.79			
T *Acrobotrys tritubus*	7H-CC–8H-2	72.21–74.25	66.36–67.5			
T *Stichocorys johnsoni*	8H-4–8H-5	78.25–79.75	71.5–73			
Stichocorys delmontensis > *S. peregrina*	9H-2–9H-3	86.5–88	78–79.5			
T *Calocycletta caepa*	9H-1–9H-2	85–85.92	76.5–78			
B *Solenosphaera omnitubus*	9H-6–9H-7	92.5–93.1	84–84.6			
T *Diartus hughesi*	10H-2–10H-3	97.5–99	87.5–89			
B *Acrobotrys tritubus*	10H-3–10H-4	99–100.5	89–90.5			
B *Spongaster berminghami*						
T *Stichocorys wolffii*	12H-1–12H-2	117.2–118.18	105–106.5			
T *Botryostrobus miralestensis*	10H-CC–11H-2	105.05–108.4	95.05–97.4			
T *Diartus pettersoni*	11H-5–11H-6	112.5–114	101.5–103.00			
Diartus pettersoni >*D. hughesi*	11H-CC–12H-1	115.53–117.2	104.53–105			
B *Diartus hughesi*	11H-CC–12H-1	115.53–117.2	104.53–105			
T *Cyrtocapsella japonica*	12H-4–12H-5	121.7–123.2	109.5–111			

T = top occurrence; B = bottom occurrence.

573 (Johnson and Nigrini, 1985). The last occurrences of *Carpocanium cristata* and *Lithopera thornburgi* were not observed at this site, and based on this, we think that the basement age here is somewhat younger than at sites farther south on this transect.

Diatoms

Diatoms are scattered in the Quaternary through upper Miocene sediments recovered from Site 852. Abundances of diatoms vary through the section, with generally rare or few specimens present in the Pliocene interval and few to abundant specimens present in the Miocene interval. Preservation of diatoms is also variable, with diatoms exhibiting poor to good preservation throughout the recovered sequence.

The diatom assemblage at Site 852 is dominated by specimens of *Azpeitia nodulifer, Hemidiscus cuneiformis, Thalassiothrix longissima,* or by an increase in the abundance of *Ethmodiscus* fragments. Additional characteristic species include *Nitzschia fossilis, Nitzschia reinholdii, Pseudoeunotia doliolus, Rhizosolenia praebergonii, Thalassiosira convexa,* and *Thalssiosira oestrupii.*

The scattered occurrence of diatoms and, often, the absence of age-diagnostic species limits stratigraphic resolution attainable using diatoms. Hole 852A consists of one mud-line core that represents the *P. doliolus* Zone. The sequence recovered from Holes 852B through 852D represents the interval from the *P. doliolus* Zone through the *Thalassiosira yabei–Actinocyclus moronensis* interval.

Samples 138-852A-1H-CC, -852B-1H-1, 120–121 cm, and -1H-2, 120–121 cm, and -852C-1H-2, 24–25 cm, and -1H-CC were assigned to the *P. doliolus* Zone, based on the occurrence of *P. doliolus* stratigraphically above the last occurrence of *N. reinholdii.* The *P. doliolus/N reinholdii* zonal boundary was placed between Samples 138-852B-1H-2, 120–121 cm, and -1H-5, 120–121 cm; -852C-1H-CC and -2H-CC; and -852D-1H-CC and -2H-CC, allowing us to assign Samples 138-852B-1H-5, 120–121 cm, through -3H-1, 120–121 cm, and -852C-2H-CC and -852D-2H-CC to the *N. reinholdii* Zone.

Samples 138-852B-3H-5, 120–121 cm, through -4H-2, 120–121 cm; -852C-3H-CC and -4H-CC; and -852D-3H-CC and -4H-CC were assigned to the *Rhizosolenia praebergonii* Zone. The occurrence of *T. convexa* in Sample 138-852B-3H-7, 120–121 cm, without *Nitzschia jouseae* suggests the placement of this sample in Subzone

Table 6 (continued).

Event	Hole 852D Interval	Depth (mbsf)	Depth (mcd)
T *Stylatractus universus*			
B *Collosphaera tuberosa*			
T *Lamprocyrtis neoheteroporos*			
T *Anthocyrtidium angulare*			
T *Theocorythium vetulum*			
B *Lamprocyrtis nigriniae*			
B *Theocorythium trachelium*			
B *Pterocorys minythorax*			
B *Anthocyrtidium angulare*	2H-CC–3H-CC	21.59–31.09	21.84–31.14
T *Pterocanium prismatium*	1H-CC–2H-CC	12.07–21.59	10.97–21.84
T *Lamprocyrtis heteroporos*			
T *Anthocyrtidium jenghisi*			
B *Theocalyptra davisiana*			
T *Stichocorys peregrina*			
T *Anthocyrtidium pliocenica*			
B *Lamprocyrtis neoheteroporos*			
B *Lamprocyrtis heteroporos*			
T *Phormostichoartus fistula*			
T *Lychnodictyum audax*	3H-CC–4H-CC	31.09–40.57	31.14–42.47
T *Spongaster pentas*			
T *Phormostichoartus doliolum*			
B *Amphirhopalum ypsilon*			
B *Spongaster tetras*			
T *Didymocyrtis penultima*			
B *Pterocanium prismatium*			
T *Spongaster berminghami*			
B *Spongaster pentas*			
T *Solenosphaera omnitubus*			
T *Siphostichartus corona*			
T *Acrobotrys tritubus*			
T *Stichocorys johnsoni*			
Stichocorys delmontensis			
> *S. peregrina*			
T *Calocycletta caepa*	7H-CC–8H-CC	69.08–78.62	75.48–85.92
B *Solenosphaera omnitubus*			
T *Diartus hughesi*			
B *Acrobotrys tritubus*			
B *Spongaster berminghami*			
T *Stichocorys wolffii*	10H-CC–11H-CC	97.47–107.18	107.42–118.18
T *Botryostrobus miralestensis*			
T *Diartus pettersoni*			
Diartus pettersoni >*D. hughesi*			
B *Diartus hughesi*			
T *Cyrtocapsella japonica*			

B. The occurrence of *T. convexa, N. jouseae,d and R. praebergonii* in Samples 138-852B-4H-2, 120–121 cm, and -852C-4H-CC indicates that these samples are equivalent to Subzone A of the *R. praebergonii* Zone.

The base of the *R. praebergonii* Zone could not be identified because poor preservation and scattered diatoms occur in Samples 138-852B-4H-CC and -5H-3, 120–121 cm. However, the occurrence of *N. jouseae* without *R. praebergonii* in Sample 138-852B-5H-2, 120–121 cm, suggests that this interval may be equivalent to the *N. jouseae* Zone. Preservation and abundance of diatoms improve in the upper portion of Core 138-852B-6H and allowed us to place this interval into the *N. jouseae* Zone.

Samples 138-852B-6H-5, 120–121 cm, through -8H-4, 120–121 cm; -852C-6H-CC through -8H-CC were tentatively placed in the *T. convexa* Zone. Samples in this interval vary in abundance and preservation of diatoms. The occurrence of *T. miocenica, T. convexa,* and *Nitzschia miocenica* without *Thalassiosira praeconvexa* in Samples 138-852B-8H-4, 120–121 cm, and -852C-8H-CC supports this zonal assignment.

The base of the *T. convexa* Zone was not identified. Sample 138-850B-8H-CC contains *T. praeconvexa* and *N. miocenica* without *T. miocenica* and *T. convexa,* which suggests that one may place this sample into Subzone B of the *N. miocenica* Zone. However, this zonal placement is tentative until additional shore-based analyses can be completed.

The occurrence of *Nitzschia cylindrica* without *N. mioceneica* or without the *Thalassiosira yabei* Group in Samples 138-852B-9H-CC and -10H-6, 120–121 cm, suggests that these samples correspond to the *Nitzschia porteri* Zone. The occurrence of the *T. yabei* Group in Samples 138-852B-10H-CC and -11H-3, 120–121 cm; -852C-10H-CC and -11H-CC; and -852D-10H-CC and -11H-CC allowed us to place these samples into the *T. yabei* Zone. The base of this zone approximates the last occurrence of *Denticulopsis hustedtii* s.l. between Samples 138-852B-11H-CC and -12H-2, 143 cm. Diatoms are generally absent from the remainder of the samples examined from the lowermost portion of the recovered sequence. One exception is Sample 138-852B-13H-2, 27 cm, which contains abundant, but poorly preserved specimens of *Thalassiostrix longissima.* Age-diagnostic species were not observed in this sample.

Table 7. Sample interval, ODP depth, and composite depth constraints of diatom events for Holes 852B, 852C, and 852D.

Event	Hole 852B			Hole 852C		
	Interval	Depth (mbsf)	Depth (mcd)	Interval	Depth (mbsf)	Depth (mcd)
T *Nitzschia reinholdii*	1H-2–1H-5	2.70–7.20	2.9–7.4			
T *Nitzschia fossilis*	1H-2–1H-5	2.70–7.20	2.9–7.4	1H-CC–2H-CC	6.08–16.08	6.08–16.88
T *Rhizosoleria praebergonii*	3H-1–3H-5	19.6–25.6	20.4–26.4	2H-CC–3H-CC	16.08–25.13	16.88–26.53
B *Pseudoeunotia doliolus*	3H-1–3H-5	19.6–25.6	20.4–26.4	2H-CC–3H-CC	16.08–25.13	16.88–26.53
T *Thalassiosira convexa*	3H-5–3H-7	25.6–27.8	26.4–28.6	3H-CC–4H-CC	25.13–35.11	26.53–36.31
T *Nitzschia jouseae*	3H-CC–4H-2	28.49–30.6	28.6–33.0	3H-CC–4H-CC	25.13–35.11	26.53–36.31
B *Rossiella praebergonii*				4H-CC–5H-4, 1	35.11–39.01	36.31–42.51
B *Thalassiosira convexa* var. *zonoaka*	5H-2–5H-5	40.1–44.6	42.95–47.45	5H-4–5H-CC	39.01–44.58	42.51–48.08
B *Asteromphalis elegans*						
T *Nitzschia cylindrica*	6H-4–6H-5	52.6–54.1	57.55–58.6	5H-CC–6H-CC	44.58–54.13	48.08–59.13
B *Nitzschia jouseae*	6H-4–6H-5	52.6–54.1	57.55–58.6	5H-CC–6H-CC	44.58–54.13	48.08–59.13
T *Nitzschia miocenia*	8H-1–8H-4	67.1–71.6	73.85–78.35	7H-CC–8H-CC	63.63–73.14	68.73–79.84
T *Nitzschia miocenica* var. *elongata*				7H-CC–8H-CC	63.63–73.14	68.73–79.84
B *Nitzschia miocenica*	8H-CC–9H-3, 75	76.02–79.15	82.15–87.65	8H-CC–9H-CC	73.14–82.58	79.84–90.78
T *Rossiella paleacea*						
T *Actioneyclus ellipticus* var. *javaraticus*	10H-1–10H-2	86.1–87.6	96.1–97.6	9H-CC–10H-CC	82.58–92.09	90.78–102.04
B *Nitzschia cylindrica*	10H-6–10H-CC	93.6–94.4	103.6–104.4			
T *Thalassiosira yabei*	10H-6–10H-CC	93.6–94.4	103.6–104.4	9H-CC–10H-CC	82.58–92.09	90.78–102.04
T *Denticulopsis hustedtii*	12H-1–12H-2	105.1–106.8	117.3–119.0			

T = top occurrence; B = bottom occurrence.

Table 7 (continued).

Event	Hole 852D		
	Interval	Depth (mbsf)	Depth (mcd)
T *Nitzschia reinholdii*			
T *Nitzschia fossilis*	1H-CC–2H-CC	12.07–21.09	10.97–21.84
T *Rhizosoleria praebergonii*	2H-CC–3H-CC	21.59–31.09	21.84–31.14
B *Pseudoeunotia doliolus*	2H-CC–3H-CC	21.59–31.09	21.84–31.14
T *Thalassiosira convexa*	2H-CC–3H-CC	21.59–31.09	21.84–31.14
T *Nitzschia jouseae*			
B *Rossiella praebergonii*			
B *Thalassiosira convexa* var. *zonoaka*			
B *Asteromphalis elegans*			
T *Nitzschia cylindrica*	5H-CC–6H-CC	49.70–59.60	53.0–64.10
B *Nitzschia jouseae*	5H-CC–6H-CC	49.70–59.60	53.0–64.10
T *Nitzschia miocenia*			
T *Nitzschia miocenica* var. *elongata*			
B *Nitzschia miocenica*			
T *Rossiella paleacea*	8H-CC–9H-CC	78.62–88.08	85.92–97.13
T *Actioneyclus ellipticus* var. *javaraticus*	9H-CC–10H-CC	78.72–88.08	97.13–107.42
B *Nitzschia cylindrica*			
T *Thalassiosira yabei*	9H-CC–10H-CC	88.08–97.47	97.13–107.42
T *Denticulopsis hustedtii*			

PALEOMAGNETISM

Measurements

Following the usual procedures, we measured paleomagnetism in the archive halves of the cores using the pass-through magnetometer. The natural remanent magnetization (NRM) was measured in all the cores from Holes 852A and 852B and in Cores 1H to 8H from Holes 852C and 852D. All the sections were AF demagnetized at 15 mT. No discrete samples could be measured because of time constraints.

Measurements of low-field susceptibility were performed every 5 cm in all the cores from Holes 852A, 852B, 852C, and 852D.

Results

Results of paleomagnetic values obtained at this site vary markedly between three intervals. In the interval from 0 to 70 mbsf (0–76 mcd), the magnetization intensity after 15 mT AF demagnetization was between 1 and 5 mA/m, and susceptibility was between 5 and 10×10^{-5} SI. Both parameters exhibit a decrease below 55 mbsf (60 mcd). Over the entire interval, the magnetization was easily measurable, and the strong vertical overprint induced by coring was almost entirely removed after demagnetization to 15 mT. This result is shown by the presence of symmetrical positive and negative inclinations in close agreement with the polarity reversal pattern shown by the declination shifts. Moreover, the inclinations measured are consistent with the latitude of the site. Because no discrete samples were progressively demagnetized at this site, we cannot demonstrate completely that our blanket treatment was sufficient to isolate the characteristic component of magnetization. However, the coherent pattern of the polarity intervals, the overall downcore consistency of the directions, and the reproducibility of the results among holes (Figs. 15, 16, and 17) strongly suggest that no other component of magnetization is present. The declinations were corrected by using the multishot orientation (Table 8). In some cases, however, a significant deviation of the declination from the north-south axis persisted after corrections (e.g., Cores 138-852B-5H and -11H) and in these

cases, an SOR orientation was used. The cause of these intermittent failures of the multishot remains unexplained.

As a result of the good quality of the magnetic signal, the correlation of the polarity intervals with the magnetic polarity time scale (MPTS) was relatively straightforward. All polarity changes from the Brunhes/Matuyama boundary to C3A-n1 were identified (Table 9; Figs. 15, 16, 17, and 18). In addition, small-scale features are present in all three holes, such as the directional changes at 23 mbsf (24 mcd), which might correspond to the Reunion Subchron.

The interval from 70 to 100 mbsf (76–111 mbsf) is characterized by very low remanence intensity that reaches values as low as 0.1 mA/m, the limit of despair for our cryogenic magnetometer. The low values in magnetization also correspond to low values in susceptibility (Fig. 19). In Figure 20, we compare the downhole evolution of the red/blue percentage ratio of reflectances with changes in magnetic susceptibility. A progressive loss of magnetism between 55 mbsf (60 mcd) to about 84 mbsf (92.5 mcd) and a progressive change in sediment color from red-brown to blue-gray probably are related to the disappearance of magnetic oxides and/or changes in magnetic mineralogy. Between 84 and 100 mbsf (92.5 to 111 mcd), the sediment is almost white and has the lowest recorded intensities. Surprisingly, this interval contains a significant clay component.

In the deepest interval, between 100 and 113.6 mbsf (111–125.3 mcd), a drastic change takes place from white to brown at 100 mbsf (111 mcd), accompanied by a sudden recovery of susceptibility and a more progressive increase in remanence intensity. Over this interval, we were able to determine a magnetic polarity sequence, and a correlation was made with the MPTS. This correlation was constrained by various biostratigraphic datums (see "Biostratigraphy" section, this chapter). This interval encompasses the upper part of Chronozone C5 and the lower part of Chronozone C4A (Figs. 15, 16, 17, and 18). As we have consistently found at other sites, a short reverse polarity interval can be seen at the top of Chronozone 5.

Table 8. Orientations for Site 852 cores.

Core no.	Aximuthal orientation (0°–360°)	Deviation from direction (0°–360°)	Vertical drift (°)
[a]138-852B-1H	0		
[a]2H	160		
[a]3H	140		
4H	050	275	1.0
5H	(102)	294	1.0
[a]5H	20		
6H	220	348	0.7
7H	220	351	0.9
8H	103	286	1.1
9H	017	300	0.4
10H	299	331	0.8
11H	(298)	345	0.6
[a]11H	217		
12H	143	302	0.9
13H	072	281	0.8
[a]138-852C-1H	110		
[a]2H	065		
[a]3H	095		
4H	187	100	2.3
5H	155	094	2.3
6H	120	106	2.2
7H	017	118	2.9
8H	090	103	2.2
9H	166	108	2.5
10H	105	105	2.5
11H	320	109	2.9
12H	145	110	2.1
[a]138-852D-1H	270		
[a]2H	215		
[a]3H	065		
4H	(328)	281	4.0
[a]4H	157		
5H	260	284	4.2
6H	174	284	4.9
7H	198	285	4.8
8H	195	285	4.7
9H	243	283	4.2
10H	269	283	3.8
11H	022	278	4.2
12H	002	275	3.7

[a]Secondary orientation (SOR) angle is the value used to adjust average measured declination to 0° or 180° for normal or reversed chronozones, respectively, when no multishot orientation was available. For multishot orientation, the measured declination was corrected by adding to it the multishot azimuthal orientation and the local geomagnetic deviation (8.9°). Multishot azimuth values in () are considered to be erroneous, and for our interpretation, we used the SOR value in the following line.

SEDIMENTATION RATES

A sedimentary section about 120 m thick that covers the time interval from the late Pleistocene to the bottom of the late Miocene was recovered at Site 852. Biostratigraphic age control was provided by all four of the chief planktonic microfossil groups.

The composite depth section for Site 852 is given in Table 10. This composite was formed by comparing shipboard measurements of GRAPE density, magnetic susceptibility, and percentages of reflectance (from the automated color analyzer) at adjacent holes. These comparisons then were integrated to form a single composite depth section for the site (a detailed discussion about the construction of composite sections during Leg 138 is presented in Hagelberg et al., this volume).

For the holes and cores listed in Column 1 of Table 10, Column 2 gives the ODP sub-bottom depth of the core top and bottom (in meters below seafloor, or mbsf). Note that the depth given in Column 2 corresponds to the depth of the bottom of the recovered core. This depth places the core catchers in their correct position in the composite depth section and is not the same as the standard ODP core-catcher depth. Column 3 shows the length of core recovered. Column 4 gives the composite depth of the core top and bottom (in meters composite depth, or mcd). Column 5 indicates the amount of offset between the ODP depth and the composite depth. Conversion from ODP sub-bottom depths to composite depths can be made by adding the offset listed in Column 5 for a given core.

GRAPE density, susceptibility, and percentage of reflectance data all produced records having relatively high amplitudes and variability through much of the section in Holes 852A (1 core), 852B (13 cores), 852C (13 cores), and 852D (12 cores) at Site 852 (Fig. 21, back pocket). Overlap of adjacent holes was maintained throughout the cored interval at Site 852, down to 129.74 mcd. Although minor distortion within individual cores occurs, a continuous, high-resolution record can easily be sampled at Site 852 using this composite record.

The sedimentation rate record for Site 852 was based mainly on a good paleomagnetic record from the Brunhes down to C3A-n2 (older than 5.68 Ma) and from the top of C4A-n1 (younger than 7.90 Ma) to the base of the section within C5-n1 (older than 9.92 Ma). In the interval having no paleomagnetic data between 79.2 (5.68 Ma) and 114.35 mcd (7.90 Ma), the first appearances of *Amaurolithus primus* (6.42 Ma) and of *Discoaster berggreni* (7.5 Ma) were used as controls. In the lowest part of the section, the last appearance of *Coccolithus miopelagicus* (9.94 Ma) at 128.3 mcd was used to constrain the sedimentation rate. Using this datum, the base of the recovered section (129.74 mcd in Core 138-852C-13X) has an estimated age of 10.1 Ma. Table 11 gives the control points selected to generate the age-vs.-depth plots shown in Figures 22A through 22D, where the depth ranges within which the datums for the observed four microfossil groups are shown.

The pattern of sedimentation rate variation vs. age (Fig. 23) and depth (Fig. 24) has some resemblance to those in Sites 848, 849, and

Table 9. Reversal boundary depths from Site 852.

Interval (cm)	Depth (mbsf)	Depth (mcd)	Interpretation	Age (Ma)	Comments
138-852B-2H-2, 105	11.45	11.70	Jaramillo (t)	0.91	
2H-3, 50	12.40	12.65	Jaramillo (o)	0.98	
3H-2, 25	20.15	20.95	Olduvai (t)	1.66	
3H-3, 35	21.75	22.55	Olduvai (o)	1.88	
3H-4, 58	23.48	24.28	Reunion (t)	2.06	
3H-4, 68	23.58	24.38	Reunion (o)	2.09	
4H-4, 68	33.08	35.48	Kaena (t)	2.92	
4H-5, 02	33.92	36.32	Kaena (o)	2.99	Section boundary
4H-5, 98	34.88	37.28	Mammoth (t)	3.08	
4H-6, 68	36.08	38.48	Mammoth (o)	3.18	
5H-5, 22	43.62	46.47	Cochiti (t)	3.88	
5H-5, 150	44.90	47.75	Cochiti (o)	3.97	Section boundary
6H-2, 115	49.55	54.50	Sidufjall (t)	4.40	
6H-3, 105	50.95	55.90	Sidufjall (o)	4.47	
6H-4, 105	52.45	57.40	Thvera (t)	4.57	
6H-7, 65	56.55	61.50	Thvera (o)	4.77	
7H-7, 80	65.99	71.84	C3A-n1 (t)	5.35	
8H-3, 60	69.50	76.25	C3A-n1 (o)	5.53	
11H-6, 102	102.82	113.82	N->R		
11H-6, 112	103.02	114.02	R->N		
11H-7, 05	103.45	114.45	C4A-n1 (t)	7.90	
12H-1, 68	104.58	116.78	C4A-n1 (o)	8.21	
12H-1, 118	105.08	117.28	C4A-n2 (t)	8.41	
12H-2, 28	105.68	117.88	C4A-n2 (o)	8.50	
12H-2, 122	106.62	118.82	C4A-n3 (t)	8.71	
12H-3, 12	107.02	119.22	C4A-n3 (o)	8.80	
12H-3, 38	107.28	119.48	C5-n1 (t)	8.92	
12H-3, 102	107.92	120.12	R->N (t)		Reversed in C5-n1
12H-3, 118	108.08	120.28	N->R (o)		
138-852C-2H-2, 80	8.30	9.10	Brunhes/Matuyama	0.73	
2H-4, 50	11.00	11.80	Jaramillo (t)	0.91	
2H-4, 135	11.85	12.65	Jaramillo (o)	0.98	
2H-5, 130	13.30	14.10	Cobb (midpoint)	1.10	
3H-3, 130	19.80	21.20	Olduvai (t)	1.66	
3H-4, 125	21.25	22.65	Olduvai (o)	1.88	
3H-5, 130	22.80	24.20	Reunion (midpoint)	2.08	
4H-3, 55	28.55	29.75	Matuyama/Gauss	2.47	
4H-7, 25	34.25	35.45	Kaena (t)	2.92	
5H-3, 25	37.75	41.25	Gauss/Gilbert	3.40	
5H-6, 90	42.90	46.40	Cochiti (t)	3.88	
6H-1, 115	45.15	50.15	Nunivak (t)	4.10	
6H-2, 135	46.85	51.85	Nunivak (o)	4.24	
6H-4, 95	49.45	54.45	Sidufjall (t)	4.40	
6H-5, 85	50.85	55.85	Sidufjall (o)	4.47	
6H-6, 80	52.30	57.30	Thvera (t)	4.57	
7H-3, 02	56.52	61.62	Thvera (o)	4.77	Section boundary
8H-2, 100	65.50	72.20	C3A-n1 (t)	5.35	
8H-5, 62	69.62	76.32	C3A-n1 (o)	5.53	
8H-7, 50	72.50	79.20	C3A-n2 (t)	5.68	
12H-2, 22	102.72	113.72	N->R (t)		
12H-2, 48	102.98	113.98	R->N (o)		
12H-2, 85	103.35	114.35	C4A-n1 (t)	7.90	
12H-4, 10	105.60	116.60	C4A-n1 (o)	8.21	
12H-4, 35	105.85	116.85	N->R (t)		
12H-4, 50	106.00	117.00	R->N (o)		
12H-4, 80	106.30	117.30	C4A-n2 (t)	8.41	
12H-5, 10	107.10	118.10	C4A-n2 (o)	8.50	
12H-5, 105	108.05	119.05	C4A-n3 (t)	8.71	
12H-5, 140	108.40	119.40	C4A-n3 (o)	8.80	Near section break
12H-6, 15	108.65	119.65	C5-n1 (t)	8.92	
12H-6, 085	109.35	120.35	R->N (t)		Reversed in C5-n1
12H-6, 100	109.50	120.50	N->R (o)		
138-852D-1H-6, 60	10.10	9.00	Brunhes/Matuyama	0.73	
2H-1, 95	12.45	12.70	Jaramillo (o)	0.98	
2H-2, 90	13.90	14.15	Cobb (midpoint)	1.10	
2H-7, 35	20.85	21.10	Olduvai (t)	1.66	
3H-2, 10	22.60	22.65	Olduvai (o)	1.88	Near section break
3H-3, 20	24.22	24.27	Reunion (t)	2.06	
3H-3, 35	24.35	24.40	Reunion (o)	2.09	
3H-6, 110	29.60	29.65	Matuyama/Gauss	2.47	
4H-3, 5	33.55	35.45	Kaena (t)	2.92	
4H-3, 90	34.40	36.30	Mammoth (t)	3.08	
4H-5, 0	36.50	38.40	Mammoth (o)	3.18	Near section break
4H-6, 25	43.05	44.95	Cochiti (t)	3.88	
5H-4, 20	44.50	47.80	Cochiti (o)	3.97	
5H-5, 105	46.85	50.15	Nunivak (t)	4.10	

Table 9 (continued).

Interval (cm)	Depth (mbsf)	Depth (mcd)	Interpretation	Age (Ma)	Comments
5H-6, 115	48.45	51.75	Nunivak (o)	4.24	
6H-1, 45	49.95	54.45	Sidufjall (t)(?)	4.40	Near core top
6H-2, 35	51.35	55.85	Sidufjall (o)	4.47	
6H-3, 30	52.80	56.10	Thvera (t)	4.57	
6H-6, 30	57.30	60.60	Thvera (o)	4.77	
7H-5, 65	65.65	72.05	C3A-n1 (t)	5.35	
11H-4, 145	102.95	113.95	N->R		Near section break
11H-5, 15	103.15	114.15	R->N		
11H-5, 55	103.55	114.55	C4A-n1 (t)	7.90	
11H-6, 110	105.60	116.60	C4A-n1 (o)	8.21	
11H-7, 20	106.20	117.20	C4A-n2 (t)	8.41	
12H-1, 85	107.35	119.10	C4A-n3 (t)	8.71	
12H-1, 120	107.70	119.45	C4A-n3 (o)	8.80	
12H-2, 0	108.00	119.75	C5-n1 (t)	8.92	Near section break
12H-2, 065	108.65	120.40	R->N		Reversed in C5-n1
12H-2, 080	108.80	120.55	N->R		

T = termination; O = onset.

Table 10. Depths of top and bottom of each core in Site 852 in the composite depth section.

Core no.	ODP depth (mbsf)	Core length (m)	Composite depth (mcd)	Δ (m)
138-852A-1H	0–5.86	5.86	0–5.86	0.00
-852B-1H	0–8.87	8.87	0.20–9.07	0.20
2H	8.90–18.94	10.04	9.15–19.19	0.25
3H	18.40–28.49	10.09	19.20–29.29	0.80
4H	27.90–37.97	10.07	30.30–40.37	2.40
5H	37.40–47.49	10.09	40.25–50.34	2.85
6H	46.90–56.95	10.05	51.85–61.90	4.95
7H	56.40–66.36	9.96	62.25–72.21	5.85
8H	65.90–76.02	10.12	72.65–82.77	6.75
9H	75.40–85.47	10.07	83.90–93.97	8.50
10H	84.90–95.05	10.15	94.90–105.05	10.00
11H	94.40–104.53	10.13	105.40–115.53	11.00
12H	103.90–113.94	10.04	116.10–126.14	12.20
13H	113.40–113.40	0.00		
138-852C-1H	00–6.08	6.08	0.00–6.08	0.00
2H	6.00–16.08	10.08	6.80–16.88	0.80
3H	15.50–25.13	9.63	16.90–26.53	1.40
4H	25.00–35.11	10.11	26.20–36.31	1.20
5H	34.50–44.58	10.08	38.00–48.08	3.50
6H	44.00–54.13	10.13	49.00–59.13	5.00
7H	53.50–63.63	10.13	58.60–68.73	5.10
8H	63.00–73.14	10.14	69.70–79.84	6.70
9H	72.50–82.58	10.08	80.70–90.78	8.20
10H	82.00–92.09	10.09	91.95–102.04	9.95
11H	91.50–101.59	10.09	102.05–112.14	10.55
12H	101.00–111.11	10.11	112.00–122.11	11.00
13H	110.50–119.34	8.84	120.90–129.74	10.40
-852D-1H	2.00–12.07	10.07	0.90–10.97	-1.10
2H	11.50–21.59	10.09	11.75–21.84	0.25
3H	21.00–31.09	10.09	21.05–31.14	0.05
4H	30.50–40.57	10.07	32.40–42.47	1.90
5H	40.00–49.70	9.70	43.30–53.00	3.30
6H	49.50–59.60	10.10	54.00–64.10	4.50
7H	59.00–69.08	10.08	65.40–75.48	6.40
8H	68.50–78.62	10.12	75.80–85.92	7.30
9H	78.00–88.08	10.08	87.05–97.13	9.05
10H	87.50–97.47	9.97	97.45–107.42	9.95
11H	97.00–107.18	10.18	108.00–118.18	11.00
12H	106.50–116.51	10.01	118.25–128.26	11.75

Note: See text for details.

Table 11. Control points for sedimentation rates at Site 852.

Composite depth (mcd)	Sediment rate (m/m.y.)	Age (Ma)	Remarks
0		0.0	Core top
9.05	12.40	0.73	B Brunhes Chron
11.75	15.00	0.91	T Jaramillo Subchron
12.67	13.14	0.98	B Jaramillo Subchron
21.08	12.37	1.66	T Olduvai Subchron
22.62	7.00	1.88	B Olduvai Subchron
29.7	12.00	2.47	B Matuyama Chron
35.46	12.80	2.92	T Kaena Subchron
36.31	12.14	2.99	B Kaena Subchron
37.32	11.22	3.08	T Mammoth Subchron
38.44	11.20	3.18	B Mammoth Subchron
41.25	12.77	3.4	B Gauss Chron
46.4	10.73	3.88	T Cochiti Subchron
47.78	15.33	3.97	B Cochiti Subchron
50.15	18.23	4.1	T Nunivak Subchron
51.8	11.79	4.24	B Nunivak Subchron
54.47	16.69	4.4	T Sidujfall Subchron
55.87	20.00	4.47	B Sidujfall Subchron
57.33	14.60	4.57	T Thvera Subchron
61.64	21.55	4.77	B Thvera Subchron
72.03	17.91	5.35	T C3A-n1
76.28	23.61	5.53	B C3A-n1
79.2	19.47	5.68	T C3A-n2
93.2	18.92	6.42	B *Amaurolithus primus*
106.0	11.90	7.5	B *Discoaster berggreni*
114.45	21.00	7.9	T C4A-n1
116.66	7.13	8.21	B C4A-n1
117.26	3.00	8.41	T C4A-n2
117.99	8.11	8.5	B C4A-n2
118.99	4.76	8.71	T C4A-n3
119.26	3.00	8.8	B C4A-n3
119.63	3.08	8.92	T C5-n1
128.3	8.50	9.94	T *Coccolithus miopelagicus*

T = top; B = bottom.

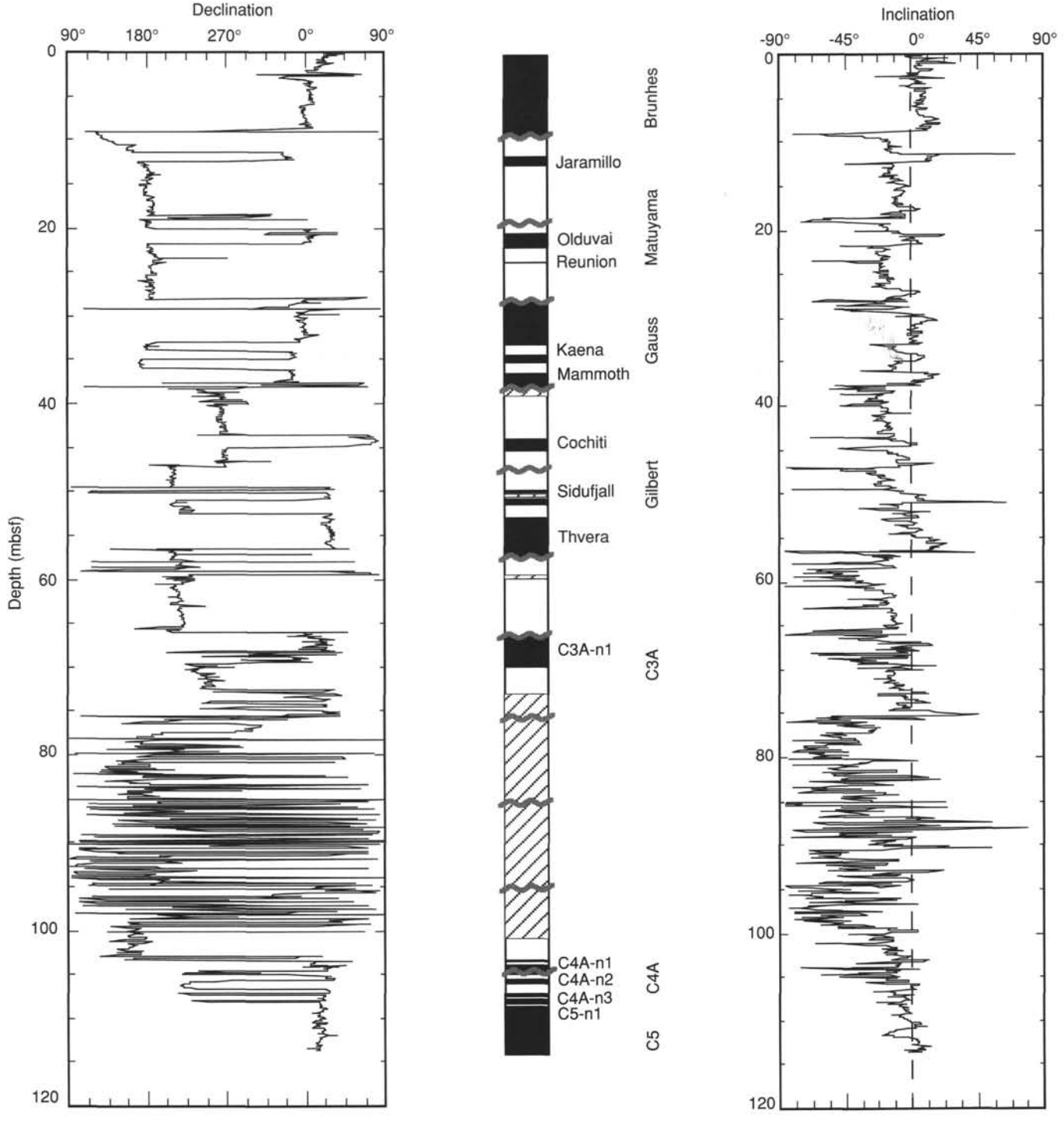

Figure 15. Declination and inclination profiles from the pass-through magnetometer (demagnetized at 15 mT) and identification of polarity chronozones in Hole 852B. Black = normal, white = reverse, hatched = no data or no interpretation. Dashed lines indicate core boundaries. Declinations have been rotated as described in Table 8. Declinations from Cores 5H and 11H have been rotated by using the secondary orientation.

850; two peaks of high sedimentation rate occurred in the earliest Pliocene and in the late Miocene. The lowest sedimentation rate was found in the interval from 8 to 9 Ma. In the upper part of the section (0–45 mcd; 0 to 4 Ma), the sedimentation rate was uniform at about 12 m/m.y. Between 4 and 5 Ma, during which interval several magnetic reversals were found to provide control points for the age-vs.-depth plots, the sedimentation rate appeared to change erratically, in contrast to the smoothly varying sedimentation rate that was observed in Site 848, where high-resolution paleomagnetic data also were available.

INORGANIC GEOCHEMISTRY

Ten interstitial-water samples were collected at Site 852: two from Hole 852A at 1.5 and 4.5 mbsf, six from Hole 852B from 27.4 mbsf to 112.9 mbsf, and two from just above the basement in Hole 852C

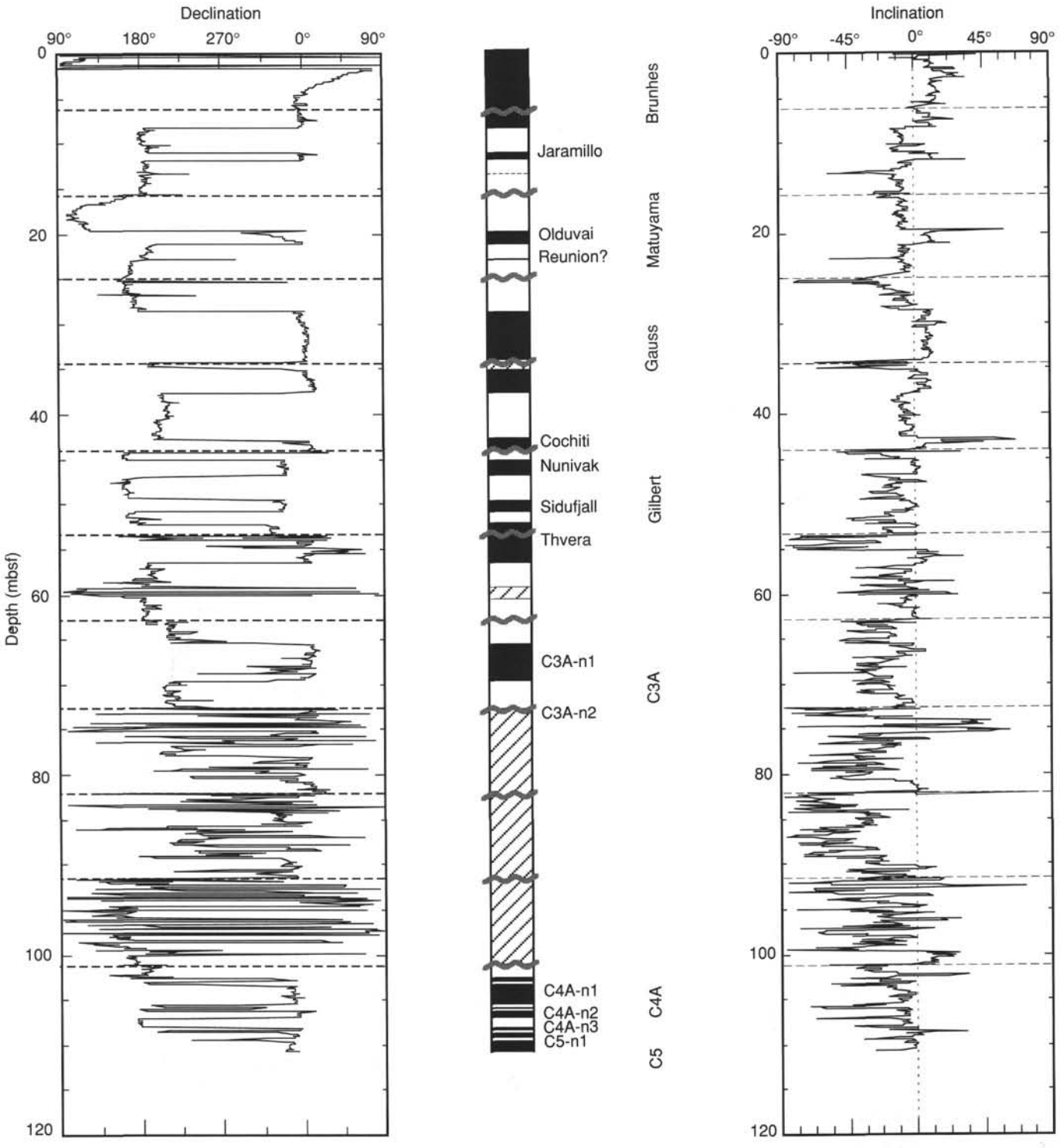

Figure 16. Declination and inclination profiles from the pass-through magnetometer (demagnetized at 15 mT) and identification of polarity chronozones in Hole 852C. Black = normal, white = reverse, hatched = no data or no interpretation. Dashed lines indicate core boundaries. Declinations have been rotated as described in Table 8.

(Table 12). Results of pore-water measurements from these three holes are here considered to constitute a single depth profile.

An interstitial-water sample was taken from Sections 1 and 3 of the solitary core making up Hole 852A. Section 138-852A-1H-1 consists of dark brown clayey nannofossil foraminifer ooze. The rest of this core is composed of yellowish-brown foraminifer nannofossil ooze. Both of these lithologies contain minor amounts of iron oxides and volcanic glass (see "Lithostratigraphy" section, this chapter).

Interstitial-water sampling in Hole 852B began with a sample from the bottom of the third core (Section 138-852B-3H-6), where the sediment is pale yellow to dark brown nannofossil foraminifer ooze. Minor amounts of clay were found throughout this core, and

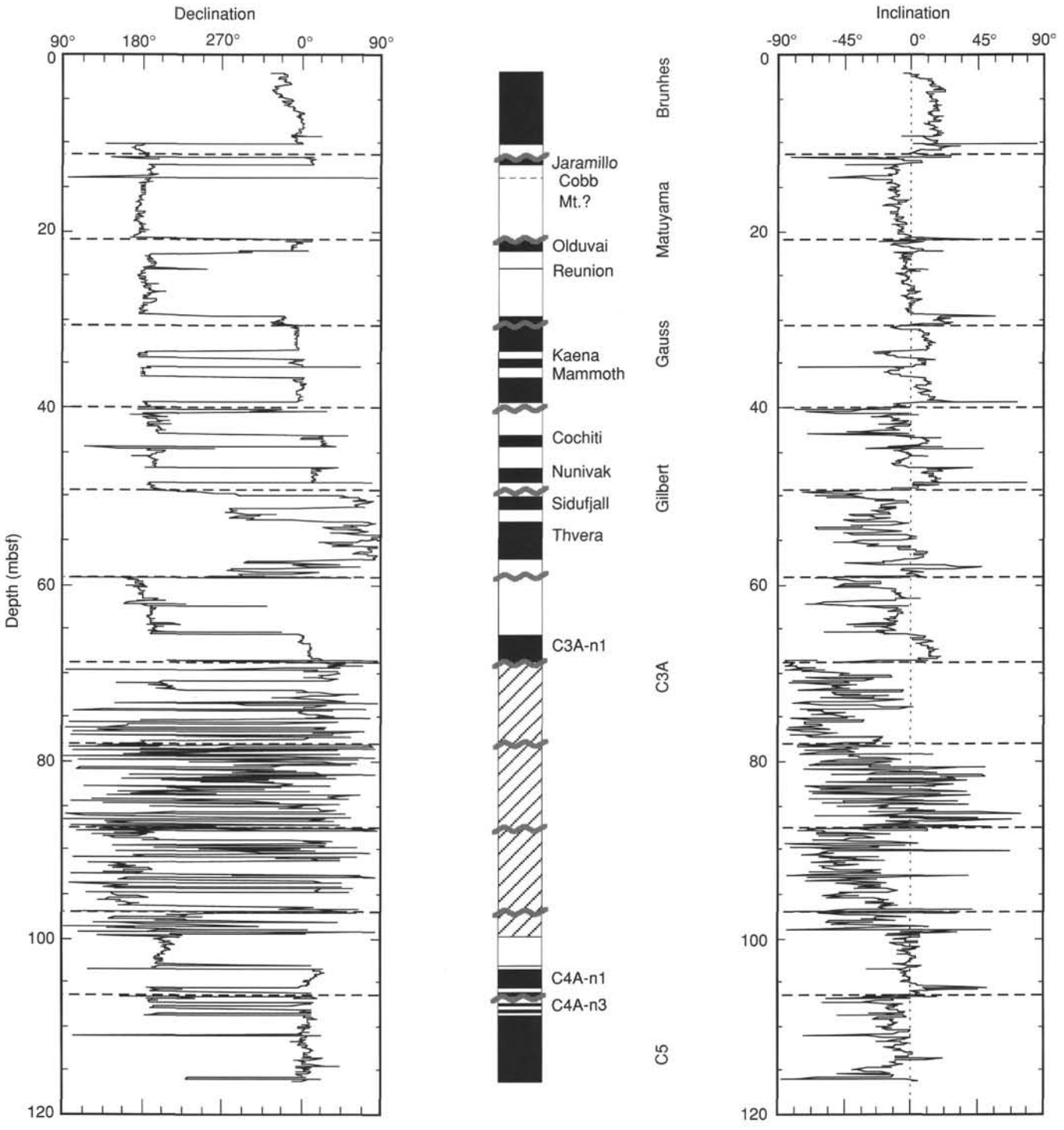

Figure 17. Declination and inclination profiles from the pass-through magnetometer (demagnetized at 15 mT) and identification of polarity chronozones in Hole 852D. Black = normal, white = reverse, hatched = no data or no interpretation. Dashed lines indicate core boundaries. Declinations have been rotated as described in Table 8.

we attributed these color variations to changes in the amount of this component, not to major shifts in lithology (see "Lithostratigraphy" section, this chapter). One interstitial-water sample was taken from Cores 138-852B-6H and -852B-9H. One sample was taken from every core below this depth, until coring was stopped by the basement after Core 138-852B-12H.

In general, sediments in Hole 852B consist of foraminifer nannofossil ooze with varying amounts of oxide. Unlike at the previous three sites, chert was not sampled at this location. Oxides appear as a minor lithology throughout these holes, which is consistent with the lower sedimentation rate found at this site (see "Sedimentation Rates" section, this chapter).

Noticeable hydrothermal influence begins in Core 138-852B-10H with the appearance of thin clasts of hematite and manganese dendrites, which continue in Core 138-852B-11H. Metalliferous radiolarian ooze with diatoms was found in Sections 2 and 3 of

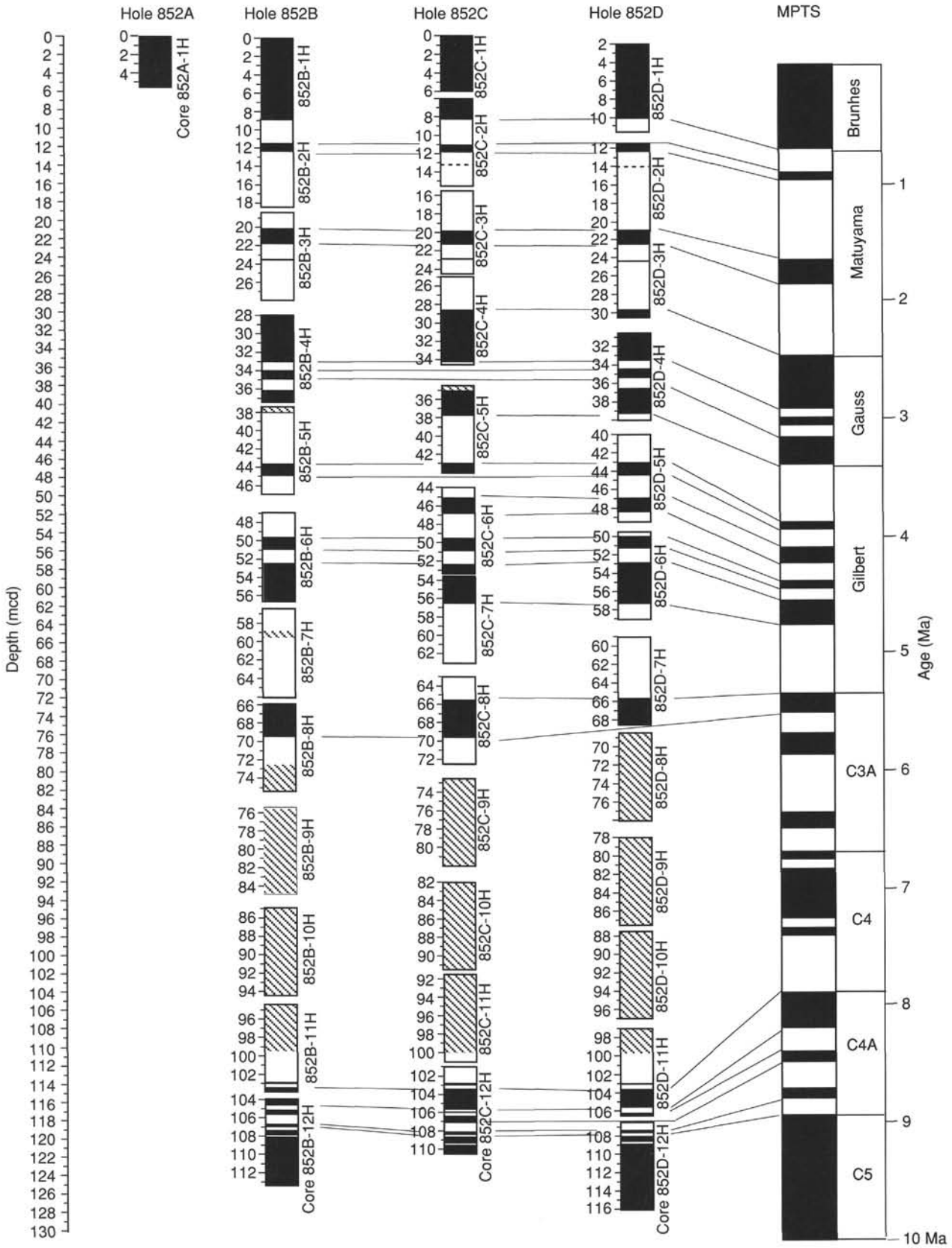

Figure 18. Magnetostratigraphic synthesis at Site 852. Depths in individual cores are in meters below seafloor (mbsf). Cores are located at appropriate composite depth (scale at far left). Black zones indicate normal polarity; white zones indicate reverse polarity; hatched zones have not been interpreted. MPTS = magnetic polarity time scale.

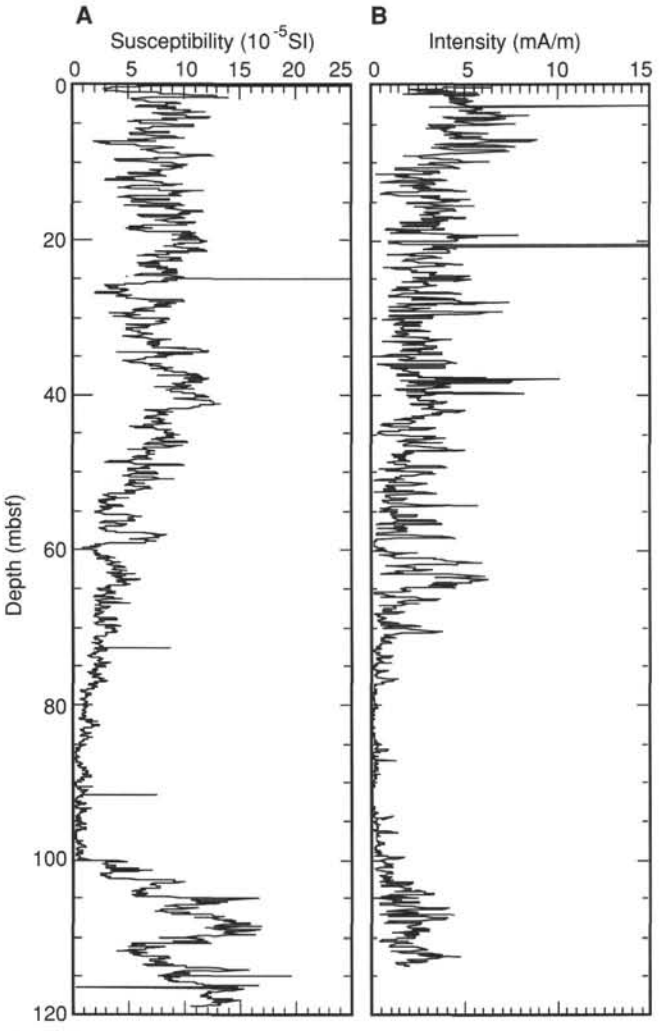

Figure 19. Changes down the core in (**A**) low-field susceptibility and (**B**) intensity of remanence after demagnetization at 15 mT measured in Hole 852B.

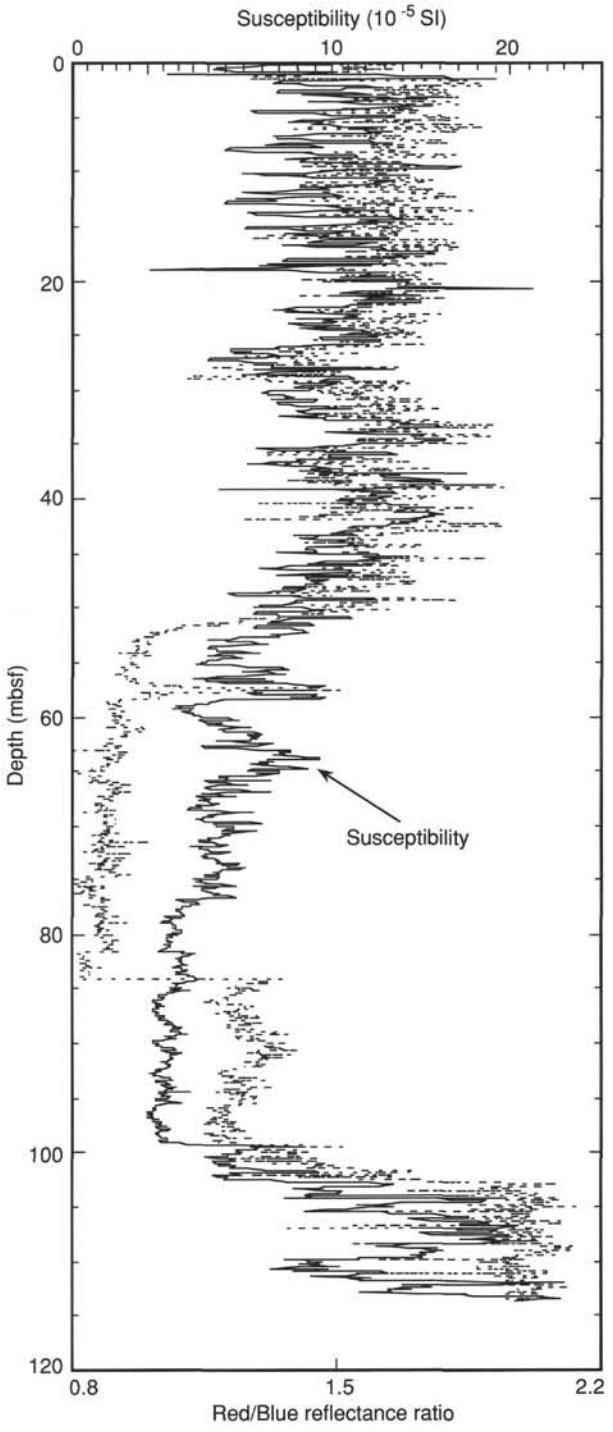

Figure 20. Relationship between color changes (characterized by red reflectance/blue reflectance ratio) in sediments from Hole 852B and variations in the amount of magnetic material, as expressed by susceptibility variations (solid line).

Core 138-852B-12H, the last core in this hole from which sediment was recovered.

Two additional pore-water samples were taken from the bottom of Hole 852C. The sample from Section 4 was taken within a layer that consists of radiolarian nannofossil ooze with oxides; however, siliceous nannofossils disappear at the top of Section 138-852C-13X-6. The last pore-water sample at this site was taken from the nannofossil ooze that makes up the bottom of Section 138-852C-13X-6 and the core catcher. We did not recover basalt from either of these holes.

The last three interstitial-water samples from Site 852 (Table 12) were taken at approximately the same depth, but different coring techniques were used. The two samples from Hole 852C were squeezed from an XCB barrel (Core 138-852C-13X), while the sample just above these two was taken from an APC core (Core 138-852B-12H). Concentrations of pore water in these three samples are similar and fit into the profiles of each parameter. These and other data collected during Leg 138 demonstrate that shipboard sampling procedures (see "Explanatory Notes" chapter, this volume) adequately compensated for disturbances during coring. These results also attest to the internal consistency of the shipboard measurements of pore water during this leg.

The smell of H_2S was completely absent at this site, and ammonia levels were below 10 μM (Table 12). These observations, together with the low sedimentation rate (see "Sedimentation Rates" section, this chapter) and low organic carbon content (see "Organic Geochemistry" section, this chapter), would suggest that the sediments at Site 852 might be oxidizing throughout. This prediction is borne out by the chemistry of the pore water (Table 12).

The total spread in interstitial sodium (Fig. 25A) and chloride (Fig. 25B) concentrations at this site are 1.7% and 1.6%, respectively. While these changes are somewhat greater than the analytical preci-

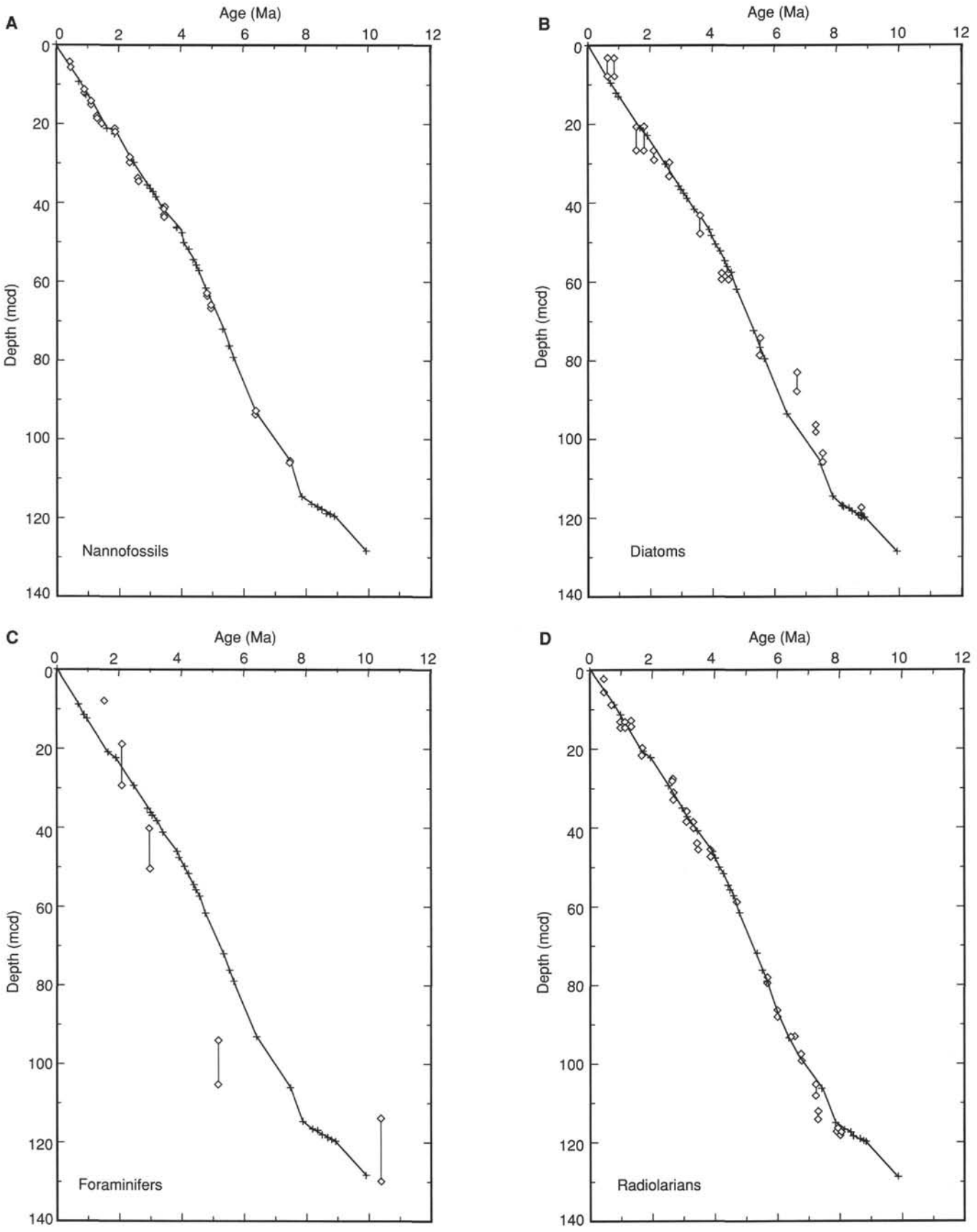

Figure 22. Plot of age vs. composite depth for Site 852, based on calibration points in Table 11, compared with microfossil datums. **A.** Nannofossils. **B.** Diatoms. **C.** Foraminifers. **D.** Radiolarians. For radiolarians, only datums that have appeared consistently in earlier sites (844 through 848) of Leg 138 are shown. Age control points from Table 11 are indicated by crosses. For each datum, the depth limits within which it was observed are indicated; where only a single symbol is visible, limits were too close to indicate at this plot scale.

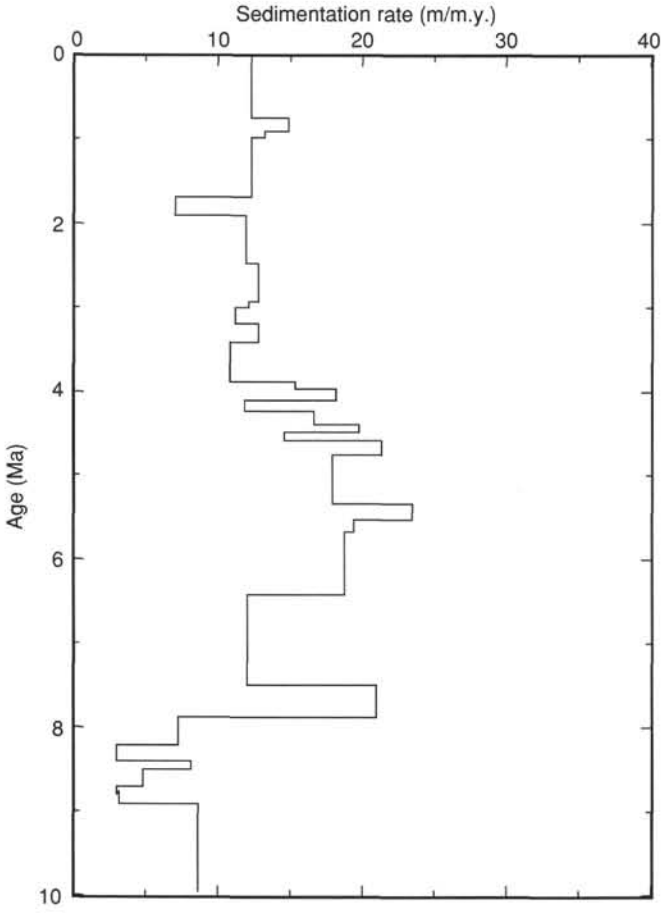

Figure 23. Linear sedimentation rate vs. age, based on data in Table 11.

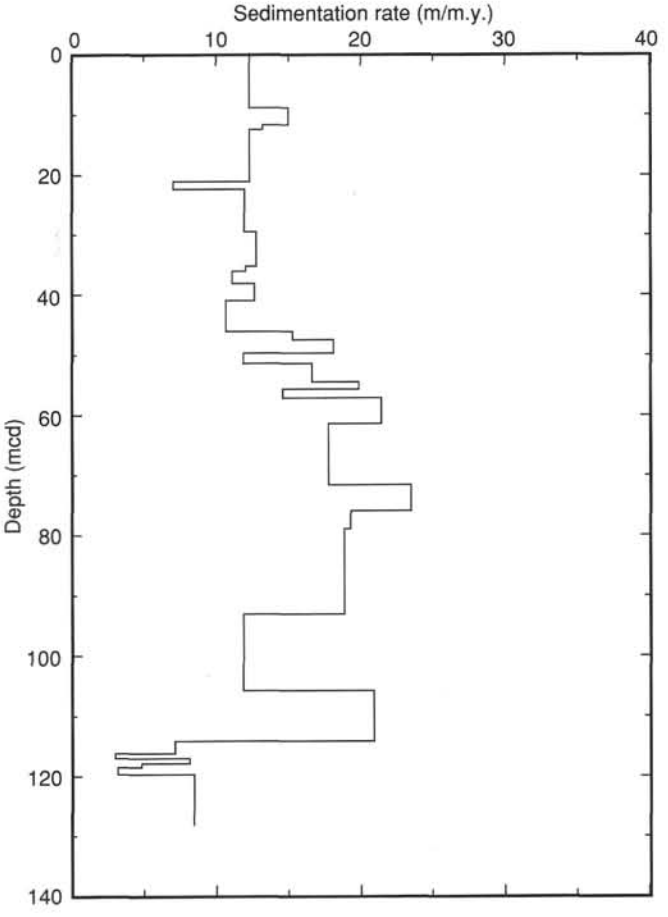

Figure 24. Linear sedimentation rate vs. composite depth, based on data in Table 11.

sion (0.5%), they are still small. For all practical purposes, these elements are not being produced or consumed at this site, nor is there any indication of vertical advection.

However, a systematic trend of decreasing salt between 80 mbsf and basement does seem to occur. This shift is matched by a similar trend in alkalinity (Fig. 25C), which might indicate that this decrease constitutes a real change. Decreasing alkalinity and salt in basal sediments would indicate either reaction and diffusive exchange with the crust, or advection of seawater within the crust or at the crust/sediment contact.

Above 80 mbsf, alkalinity at this site is constant, but somewhat higher than the bottom water (Fig. 25C). This profile indicates that early diagenesis is confined to the upper sediment layers. Near the sediment/water interface, oxygen and nitrate are consumed to oxidize organic matter (Froelich et al., 1979). This process may be supplemented with a small amount of sulfate reduction at this site (Fig. 25D). The observation that a similar alkalinity was found from the surface to 80 mbsf suggests that the pore water being buried is not in direct communication with the bottom water and, thus, production of alkalinity must occur at some distance below the interface.

Because sulfate is not being reduced to any great extent at this site, one would not expect to see the decreasing concentrations of magnesium and calcium associated with the precipitation of calcium carbonate (Baker, 1986; Suess, von Huene, et al., 1988; Pedersen and Shimmield, 1991). Concentrations of magnesium (Fig. 26A) and calcium (Fig. 26B) at Site 852 are consistent with this scenario. Calcium actually increases slightly at 25 mbsf, but molecular diffusion alone might explain the rest of this profile.

Potassium (Fig. 26C) decreases in a linear fashion all the way to the basement. This profile is suggestive of potassium removal within the crust and diffusive communication with the sediment column (McDuff, 1981), although the change with depth is subtle.

Silica (Fig. 26D) increases downhole, apparently in response to continuous re-equilibration during the metamorphism of biogenic silica (Kastner, 1981). Interestingly, the silica trend reverses itself at the same depth as the inflections in sodium (Fig. 25A), chloride (Fig. 25B), and alkalinity (Fig. 25C).

Strontium (Fig. 27B) at Site 852 increases in response to the recrystallization of biogenic calcite (Elderfield and Gieskes, 1982; Baker et al., 1982; Gieskes et al., 1986; Baker, 1986). The lithium profile at Site 852 (Fig. 27A) is similar to those developed for other Leg 138 sites and shows that lithium decreases sympathetically as strontium increases.

In summary, profiles of alkalinity and sulfate at Site 852 suggest that early diagenesis has been confined to the top few meters of sediment. The small increase in alkalinity generated by this process is not large enough to precipitate diagenetic calcium carbonates. As a result, concentrations of calcium and magnesium do not decrease with depth. Strontium increases because of recrystallization, while lithium decreases sympathetically, as at other Leg 138 sites. Concentrations of all parameters return to bottom-water values at the crust/sediment contact.

ORGANIC GEOCHEMISTRY

Carbonate and Organic Carbon

Inorganic and organic carbon were measured in Hole 852B following the methods outlined in the "Explanatory Notes" chapter (this volume). From the inorganic carbon data, we calculated the weight percent of calcium carbonate (%$CaCO_3$). Percentages of organic

Table 12. Interstitial-water geochemical data for Holes 852A, 852B, and 852C.

Core, section, interval (cm)	Depth (mbsf)	pH	Salinity	Chloride (mM)	Sodium (mM)	Alkalinity (mM)	Sulfate (mM)	Magnesium (mM)	Calcium (mM)
138-852A-1H-1, 145–150	1.5	7.09	35.5	556	477	2.909	28.37	53.54	10.36
1H-3, 145–150	4.5	7.18	35.8	558	478	2.922	27.82	53.40	10.42
138-852B-3H-6, 145–150	27.4	7.18	36.5	559	480	3.052	28.55	52.98	11.26
6H-6, 145–150	55.9	7.14	35.8	561	481	2.891	27.95	52.95	11.12
9H-6, 145–150	84.4	7.09	36.3	564	485	2.926	28.09	53.34	10.82
10H-6, 145–150	93.9	7.13	35.5	562	482	2.896	28.12	53.43	10.65
11H-6, 145–150	103.4	7.17	36.0	561	481	2.611	28.44	53.67	10.57
12H-4, 145–150	112.9	7.21	35.5	557	478	2.408	28.28	52.89	10.47
138-852C-13X-4, 145–150	116.5	7.21	35.8	555	477	2.473	28.49	53.05	10.47
13X-4, 96–104	119.0	7.22	35.5	555	477	2.449	28.28	53.14	10.37

Table 12 (continued).

Core, section, interval (cm)	Potassium (mM)	Strontium (μM)	Lithium (μM)	Silica (μM)	Ammonia (μM)
138-852A-1H-1, 145–150	11.3	88	28.1	639	<10
1H-3, 145–150	11.2	93	25.5	636	<10
138-852B-3H-6, 145–150	11.1	106	21.7	678	<10
6H-6, 145–150	11.0	117	21.3	712	<10
9H-6, 145–150	10.5	112	23.2	836	<10
10H-6, 145–150	10.4	106	23.8	801	<10
11H-6, 145–150	10.6	101	25.9	754	<10
12H-4, 145–150	10.4	92	27.0	633	<10
138-852C-13X-4, 145–150	10.5	96	27.2	684	<10
13X-4, 96–104	10.4	92	25.6	645	<10

carbon ($\%C_{org}$) were determined by measuring the amount of carbon in the dried residues from Coulometer analyses after treatment with 2N HCl (see "Explanatory Notes" chapter, this volume). The analytical results are listed in Table 13 (CD ROM, back pocket) with respect to both ODP depth (mbsf) and to composite depth (mcd; see "Sedimentation Rates" section, this chapter). If a duplicate analysis was performed on a given sample, both the mean value of the original analysis and the duplicate are listed in Table 13 (CD ROM, back pocket). Duplicate percentage of $CaCO_3$ analyses are listed in Table 14. The results indicate a reproducibility of 0.8%.

Figures 28 and 29 show percentages of $CaCO_3$ and C_{org} at Site 852 vs. ODP depth and vs. composite depth and age, respectively, based on datum levels identified at Site 852 (see "Sedimentation Rates" and "Paleomagnetism" sections, this chapter). The record of percentage of $CaCO_3$ at Site 852 shows high values (65%–80%) in the upper 100 m of the section. As was the case at other sites on the western transect, the carbonate record has been accentuated by several intervals of significantly lower percentages of $CaCO_3$ (30%–50%; Fig. 28). Concentrations of organic carbon are low (0.0%–0.1%) throughout. According to shipboard chronostratigraphy, the pronounced low-carbonate interval near 9 Ma may be coeval with intervals of low percentages of $CaCO_3$ at other sites along the western transect.

Accumulation Rates

We calculated the average values of several sedimentary parameters in time intervals delimited by the chronostratigraphic levels discussed in the "Sedimentation Rates" section (this chapter) to estimate sediment mass accumulation rates (MARs). The average values of percentages of $CaCO_3$, C_{org}, linear sedimentation rate (LSR), dry-bulk density (DBD), bulk-sediment mass accumulation rate (bulk MAR), non-$CaCO_3$ MAR, and C_{org} MAR for 32 time intervals since 10 Ma are listed in Table 15. The mean values are presented vs. composite depth in Figure 30 and vs. age in Figure 31. Superimposed on the mean values are estimates of the instantaneous MAR calculated for each sample. The mean accumulation rates of bulk sediment are significantly lower than those at Sites 849 through 851 and similar to those at Site 848. However, the characteristic and well-defined maximum in MARs in the period from 7 to 4 Ma that was observed at the other sites also is evident at Site 852, where upper Pliocene and Pleistocene carbonate accumulation rates, on average, are one-half those of values in the upper Miocene and lower Pliocene.

Gas Geochemistry

One sample for gas analysis was taken from each core of Hole 852B. We measured no hydrocarbon gas above the detection limits.

PHYSICAL PROPERTIES

Introduction

Physical properties measured routinely in whole-round sections at Site 852 include GRAPE density, compressional-wave velocity (using the MST), and thermal conductivity. Discrete samples were taken from split cores for measuring index properties: wet-bulk density, dry-bulk density, water content, porosity, and void ratio. Also in the split cores, compressional-wave velocity was determined using the digital sonic velocimeter (DSV), and shear strength was measured using a Wykeham-Farrance vane shear device. Our methods of analysis are described in the "Explanatory Notes" chapter (this volume).

Physical properties were determined twice in each section of the cores from Hole 852B. Cores from Hole 852C were sampled once per section. Index property samples were always taken at the same depth interval as those for velocity measurements. No shear strength tests nor thermal conductivity determinations were performed in sections from Hole 852C. Here, we describe the downhole distribution of the physical properties from Hole 852B, because each section of its cores was measured twice, which provided the highest resolution profiles of any hole.

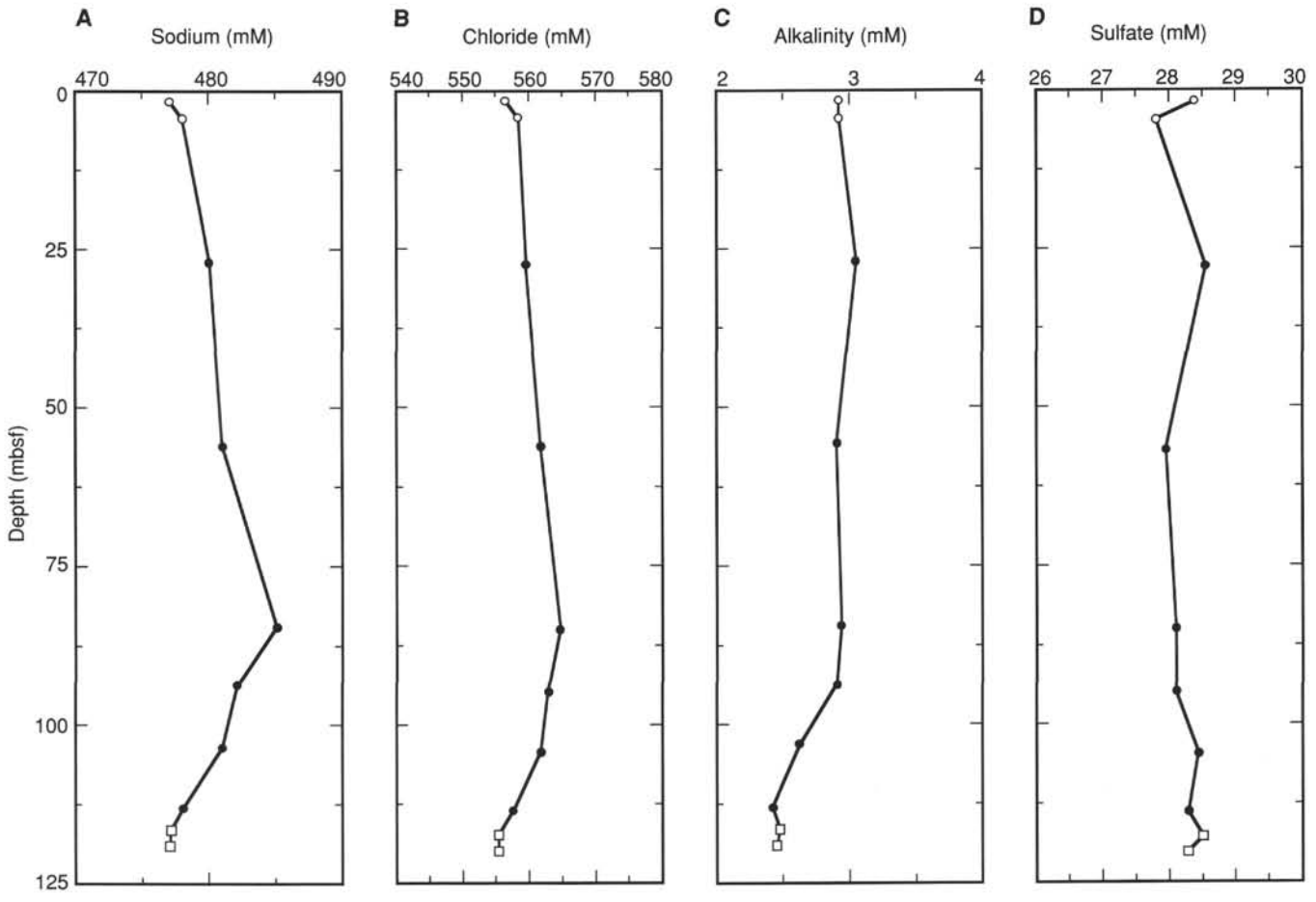

Figure 25. Interstitial-water geochemical data with sub-bottom depths for Holes 852A (open circles), 852B (solid circles), and 852C (open squares). **A.** Sodium. **B.** Chloride. **C.** Alkalinity. **D.** Sulfate.

Index Properties

Wet-bulk density values range from 1.21 to 1.66 g/cm^3 and generally increase with depth (Table 16, CD ROM, back pocket; Fig. 32), although a significant decrease occurs in the basal 20 m of sediment.

Water content, expressed relative to dry weight (Fig. 33; Table 16, CD ROM, back pocket), varies between 346% and 67% and generally decreases downhole. Intervals having water contents significantly greater than the mean occur between 15 and 20 mbsf, 35 and 45 mbsf, and 105 and 110 mbsf.

Porosity (the volumetric expression for the water content) ranges between 65% and 90%, with a mean value near 77%. Porosity generally decreases with depth (Fig. 34; Table 16, CD ROM, back pocket), except for a large increase that occurs in the basal 20 m of sediment. The downhole variation in porosity shows the same trends as in water content.

Grain density (Fig. 35; Table 16, CD ROM, back pocket) varies between 2.51 and 2.83 g/cm^3, with a mean value of 2.71 g/cm^3. Average grain density values may decrease slightly with depth below 40 mbsf. An interval of low grain densities can be seen between 105 and 110 mbsf (grain densities < 2.60 g/cm^3). This depth interval also is characterized by lower wet-bulk densities and high water contents.

Compressional-Wave Velocity

Compressional-wave velocity was measured perpendicular to bedding in split cores from Holes 852B and 852C. These measurements were performed in Cores 138-852B-1H through -8H and 138-852C-1H through -7H. Compressional-wave velocity values range between 1484 and 1545 m/s (Fig. 36; Table 17, CD ROM, back pocket). Velocity values are constant down to 60 to 80 mbsf, at which point they increase to the base of the hole. Values lower than the mean occur between 40 and 60 mbsf and at about 100 mbsf.

Shear Strength

Shear strength values range between 7.5 and 92.2 kPa (Fig. 37; Table 18, CD ROM, back pocket). These values increase downhole through the first 20 m, below which mean values remain constant. Variability, however, is much greater in the lower 60 m of the section. A zone characterized by high shear strength values (shear strength >70 kPa) occurs below 100 mbsf.

Thermal Conductivity

Thermal conductivities were determined routinely for four sections (Sections 1, 3, 5, and 7) from each core in Hole 852B to a depth of 113 mbsf. These values vary between and 0.83 and 1.45 W/[m • K]) and have a mean value of 1.07 W/(m • K). The profile for thermal conductivity generally mirrors that for wet-bulk density and is inversely related to water content and porosity (Fig. 38; Table 19, CD ROM, back pocket).

Relationships of Physical Properties and Lithology

The downhole distribution of physical properties at Site 852 indicates that two factors control physical property data: gravitational

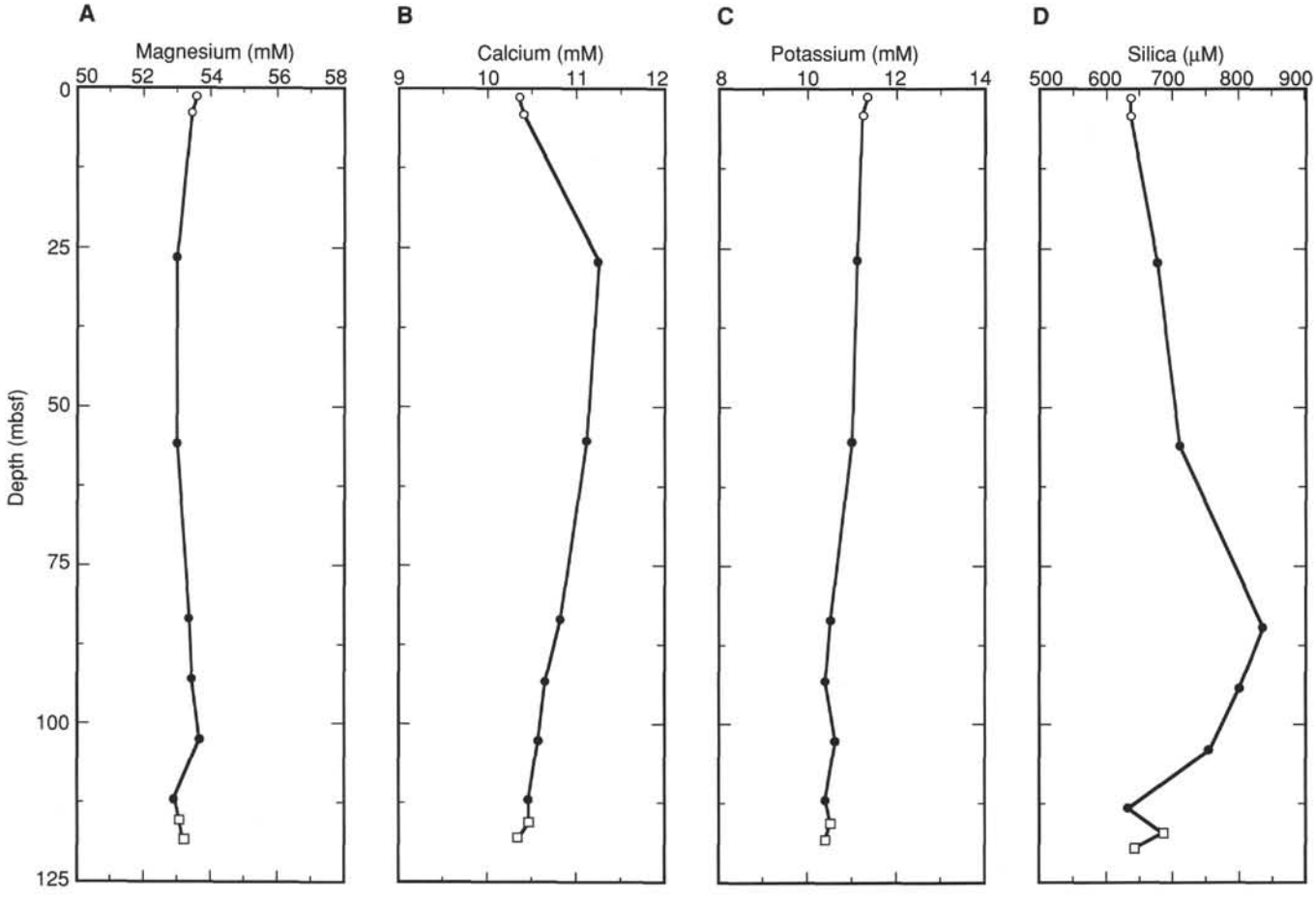

Figure 26. Interstitial-water geochemical data with sub-bottom depths for Holes 852A (open circles), 852B (solid circles), and 852C (open squares). **A.** Magnesium. **B.** Calcium. **C.** Potassium. **D.** Silica.

compaction and lithologic variation. Gravitational compaction causes a reduction of water content and porosity with burial depth. Shear strength, wet-bulk density, and thermal conductivity increase downhole from consolidation processes. Lithologies rich in siliceous or clay material (e.g., interbedded intervals at about 40 and 60 mbsf) have higher water content, porosity, and compressional-wave velocity values, whereas wet-bulk densities and thermal conductivities are lower. Grain density, the "material constant," is also lower for intervals rich in siliceous material, because the density of biogenic opal is much less than that of carbonate. The low wet-bulk densities and grain densities and high water contents and porosities below 100 mbsf correspond to a sharp increase in siliceous material (radiolarian nannofossil ooze). The interlocking nature of the siliceous tests provides a stronger, more open framework that is less affected by compaction than calcareous ooze.

DOWNHOLE MEASUREMENTS

Hole 852D was logged only with the geochemical tool string. The hole was logged openhole from 116 to 49.4 mbsf and logged to the mud line through pipe. Even though the section is thin, much of the same late Miocene time interval that was logged in other holes can be located in the openhole logged section at Site 852. The age of the top of the openhole section is about 4.5 Ma, and the base of the logged section is almost 10 Ma (see "Sedimentation Rates" section, this chapter).

The slow sedimentation rates at Site 852 reduce the temporal resolution of the logs, yet most features can be traced from site to site. However, features in the Ca log are present at this site that distinguish this log from those from Leg 138 sites farther south (Fig. 39). In particular, the high carbonate interval between 86 and 102 mbsf (6.2–7.5 Ma) shows much more structure in Site 851.

Quality of Data

Data from the geochemical logging are uniformly good in the openhole section. We calibrated the GST by letting out about 5 to 7 m of slack after the tool string was set down on the bottom of the hole and we began logging upward with slack wire. We finished the calibration at about the same time the tool string was lifted from the bottom of the hole. The calibration data appear as spikes and noise in the raw records below the actual starting depths for individual logging tools in the string. This method of calibration eliminated ACT-induced activation of the borehole and poor NGT data. In Table 20, we list where the good data start for each of the logging tools. The GST briefly went out of calibration when it entered the pipe; a section of spikes can be found in the interval between about 39 and 49 mbsf.

Depth Shifts To Match Core and Logs

The log data were shifted downward by 2.1 m so that a peak in the aluminum log at 107 mbsf matches the extreme low value in carbonate found near the bottom of the sediment section. In Figure 40, we show the core measurements as percentages of noncarbonate (100-$CaCO_3$%) so that peaks should match. With this depth shift, the major peak matches, but many of the minor noncarbonate minima and maxima do not match well. This lack of correlation is partly the result of opal

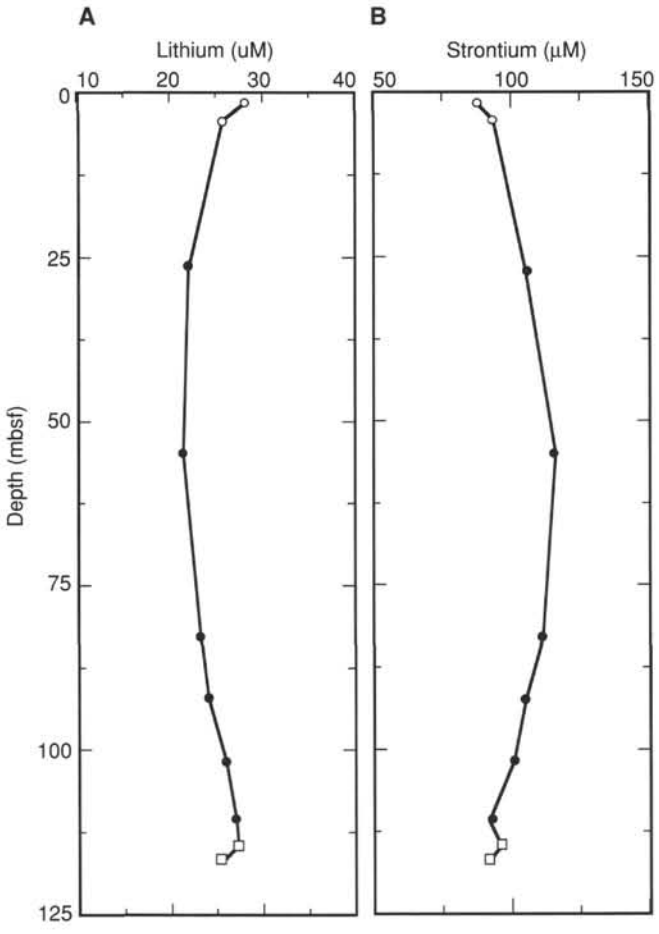

Figure 27. Interstitial-water geochemical data with sub-bottom depths for Holes 852A (open circles), 852B (solid circles), and 852C (open squares). **A.** Lithium. **B.** Strontium.

in the noncarbonate fraction. One can only estimate the abundance of opal after reprocessing the logging data post-cruise or after discrete measuring of core material.

Sediments of Hole 852D

As with all the other sites of Leg 138, the most prominent features in the chemical logs at Site 852 are associated with calcite content. The noncarbonate fraction, however, is more clay-rich and opal-poor than any of the equatorial sites. Ca-yield is high between 89.5 and 104.5 mbsf, and the aluminum peak associated with low shipboard calcite measurements occurs between 105.5 and 109.5 mbsf. The low Ca interval is not well-resolved near the base of the hole when one compares the Ca yield from the GST to the shipboard calcite record.

The low Ca-yield section at the base of the hole also has high contents of Fe and Si (Fig. 39). Neither the Fe nor the Si record matches the noncarbonate record in detail, but part of the absence of a match may be an artifact of poor data. When the uncalibrated neutron porosity from the GST tool is plotted beside the noncarbonate profile (Fig. 41), one can find an interval at about 106 mbsf, where the GST data may be appear poor. Porosity in the interval decreases to a level of zero and splits an interval that otherwise did have relatively high porosity.

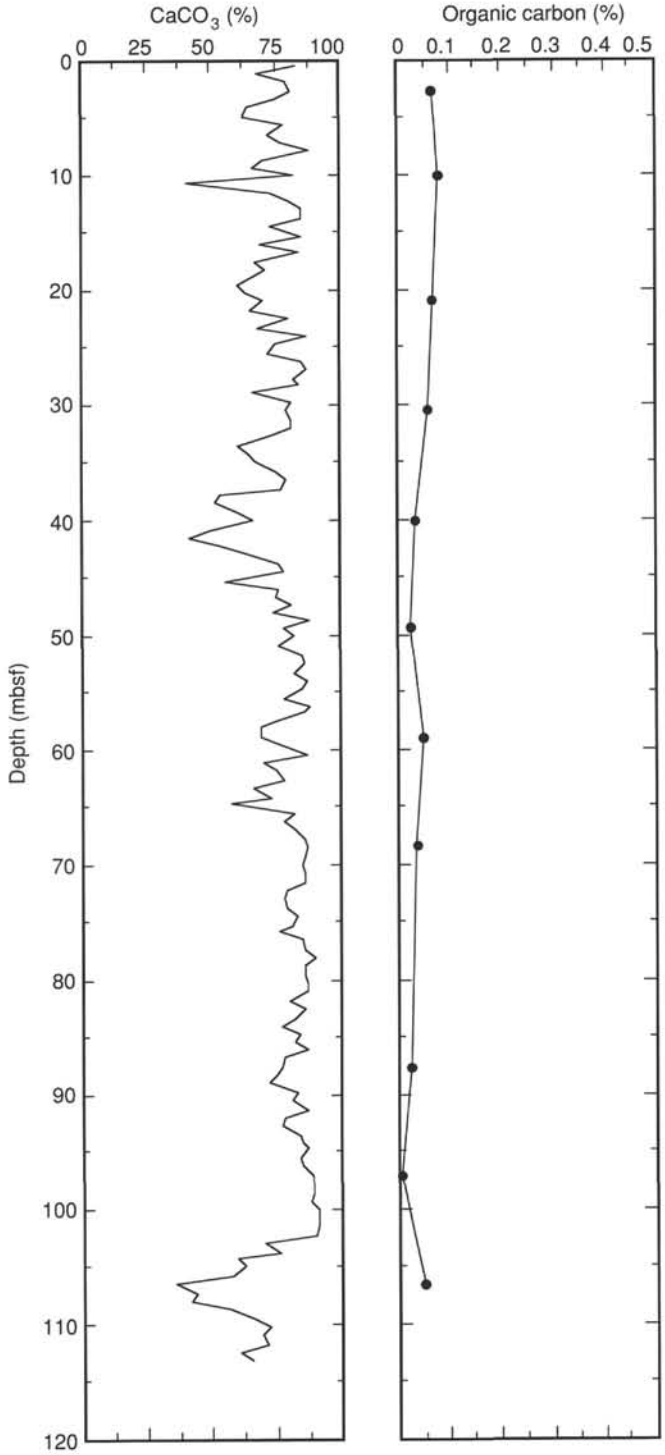

Figure 28. Downhole records of percentages of $CaCO_3$ and C_{org} vs. ODP depth for Site 852.

A rough estimate of clay abundance at Site 852 (compared to other equatorial sites, e.g., Sites 851 and 852, Fig. 42) can be obtained by comparing their Al profiles. The Al content of Site 852 is about an order of magnitude higher than that at Site 851 for sediments of approximately the same age. This clay also seems to be a mixture of several different components, as will be discussed later when the aluminum log is compared to natural gamma-ray activity data.

Table 14. Duplicate analyses of percentage of $CaCO_3$ in samples from Site 852.

Core, section, interval (cm)	depth (mbsf)	depth (mcd)	First run $CaCO_3$ (%)	Second run $CaCO_3$ (%)	Absolute value of $CaCO_3$ (difference)
138-852B-1H-1, 33–35	0.34	0.54	83.51	84.61	1.10
1H-1, 111–113	1.12	1.32	68.82	68.48	0.34
1H-2, 104–106	2.55	2.75	82.25	81.82	0.42
1H-3, 33–35	3.34	3.54	75.24	76.00	0.76
1H-3, 104–106	4.05	4.25	65.70	64.94	0.76
1H-4, 33–35	4.84	5.04	63.16	61.90	1.27
1H-6, 33–35	7.84	8.04	88.75	89.17	0.42
2H-1, 104–106	9.93	10.18	83.01	81.91	1.10
2H-2, 32–34	10.73	10.98	41.46	41.63	0.17
2H-2, 102–104	11.43	11.68	74.06	73.21	0.84
2H-4, 102–104	14.43	14.68	74.48	73.89	0.59
2H-5, 32–34	15.23	15.48	86.05	85.37	0.68
2H-6, 32–34	16.73	16.98	84.36	84.19	0.17
2H-7, 34–36	18.25	18.50	71.94	70.93	1.01
3H-1, 103–105	19.44	20.24	61.22	61.64	0.42
3H-2, 32–34	20.23	21.03	64.09	63.50	0.59
3H-3, 32–34	21.73	22.53	66.46	65.86	0.59
3H-4, 103–105	23.94	24.74	86.55	88.83	2.28
4H-1, 104–106	28.95	31.35	66.46	67.72	1.27
4H-2, 104–106	30.45	32.85	79.63	79.37	0.25
5H-2, 103–105	39.94	42.79	67.55	67.13	0.42
5H-3, 103–105	41.44	44.29	43.40	42.05	1.35
5H-4, 30–32	42.21	45.06	54.80	54.13	0.68
5H-6, 32–34	45.23	48.08	56.49	56.07	0.42
6H-2, 33–35	48.74	53.69	88.49	89.34	0.84
6H-2, 98–100	49.39	54.34	78.19	78.78	0.59
7H-2, 119–121	58.89	64.74	69.66	70.34	0.68
7H-3, 117–119	60.37	66.22	87.23	88.07	0.84
7H-6, 102–104	64.72	70.57	58.18	58.01	0.17
8H-2, 100–102	68.41	75.16	88.41	86.81	1.60
8H-4, 32–34	70.73	77.48	85.96	87.65	1.69
9H-2, 102–104	77.93	86.43	90.44	91.20	0.76
9H-5, 32–34	81.73	90.23	79.88	80.89	1.01
10H-2, 103–105	87.44	97.44	78.19	77.77	0.42
12H-2, 102–104	106.43	118.63	36.14	35.80	0.34
Average					0.77

Note: Average difference between original and duplicate analyses was 0.8% or %$CaCO_3$. Average value of original and duplicate analyses is reported in Table 13.

Porosity Effects on Raw GST Data

High Fe-yield can be found in the high Ca-yield section between 89.5 and 104.5 mbsf (Fig. 39). Even the Ca-yield in this section is significantly higher than what one would expect from comparing the logging data to shipboard carbonate measurements. Except for relatively short intervals, the entire section between 50 and 104 mbsf of shipboard measurements has carbonate maxima that reach about 90% calcite. The high Ca-, Fe-, and Si-yields over the interval from 89.5 to 104.5 mbsf are the result of porosity changes that will be corrected during shore-based data processing. The shipboard relative yields are the normalized sum of all the rock-forming element yields plus chlorine and hydrogen from the water.

Figure 43 illustrates the correlations between an uncalibrated neutron porosity measurement from the GST and the yields of several of the elements measured by the GST. Normally, in eastern Pacific Ocean sediments, one finds an inverse correlation between calcite content and porosity, because clays and opal-rich sediments have higher water contents than do carbonates. Usually, one should find a positive correlation between elements like Fe and Si and porosity, for the same reason. The noncarbonate fraction should be high in porosity and high in aluminosilicates.

What we observe, however, is that a positive correlation exists between neutron porosity and elements contained in pore waters (H and Cl), but a negative correlation between porosity and all the components of the solid phases. Fe, Si, and Ca (not shown), all are anti-correlated to porosity. Lower porosity will affect elemental yields because more neutrons interact with the borehole solids and produce more characteristic gamma rays from them than high-porosity intervals. Porosity effects also appear in GST records from the other sites, but these are not as apparent as at Site 852.

Natural Gamma-Ray Activity and Clays at Site 852

The natural gamma-ray activity of Hole 852D sediments gives one a glimpse of the complex nature of the noncarbonate fraction at the site (Fig. 44). The natural gamma-ray activity and concentrations of Al do not correlate with each other, but this absence of correlation does not reflect uranium contents as it did at other Leg 138 sites. Except for two small intervals in Hole 852D, uranium contents do not significantly affect the natural gamma-ray log. Uranium contents are essentially constant, except for a spike at about 68 mbsf and an interval between 85 and 87 mbsf. Both of these intervals appear as peaks in the natural gamma-ray log.

Were the clay composition constant, good correlations should be observed between potassium, aluminum, and thorium. No obvious correlation exists among the three. Al content is high and relatively stable between 52 and 77 mbsf, but potassium has a distinct broad maximum

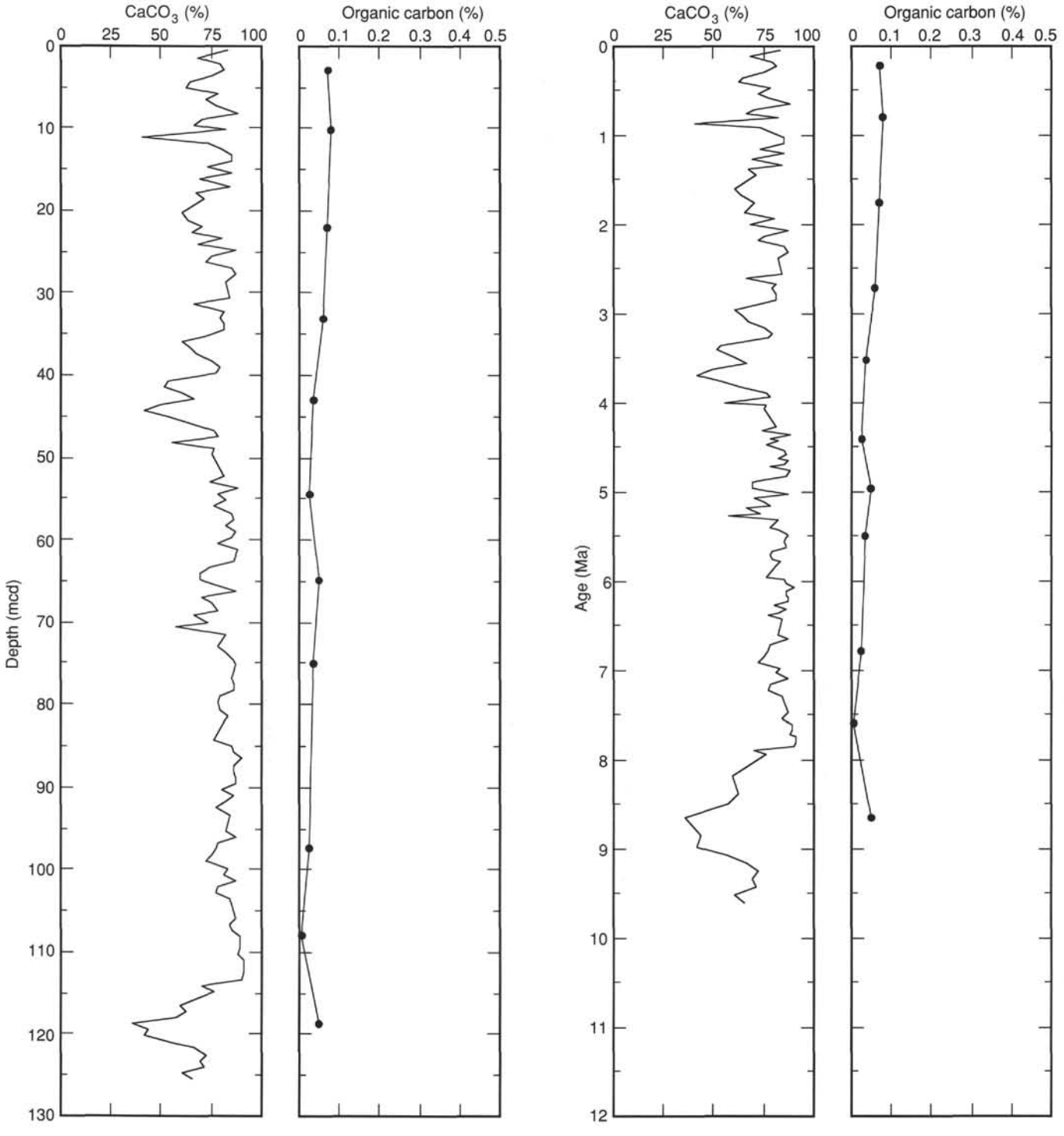

Figure 29. Plots of percentages of $CaCO_3$ and C_{org} vs. composite depth and age for Site 852.

at 65 mbsf, and the interval between 68 and 80 mbsf has very low potassium contents. The potassium profile correlates with natural gamma-ray activity if one removes the uranium spikes. The thorium profile is vaguely shaped like that of potassium, although it is highest at the top of the openhole section and seems to have more structure than potassium in the interval between 80 and 95 mbsf. All this variety in the noncarbonate fraction clearly indicates that the noncarbonate fraction is made up of several components that vary temporally.

SEISMIC STRATIGRAPHY

Modeling Procedures

We generated synthetic seismograms from velocity and density models for Site 852 to correlate reflectors in the seismic section to stratigraphic changes. Because of the thin sediment cover at this site, no downhole geophysical logging was done. A density model was

Table 15. Average values of sedimentary parameters calculated over time intervals defined by chronostratigraphic levels in Table 11.

Composite depth (mcd)	Age (Ma)	Mean $CaCO_3$ (%)	Mean C_{org} (%)	Sed. rate (m/m.y.)	Mean DBD (g/cm^3)	Mean bulk MAR ($g/cm^2/k.y.$)	Mean $CaCO_3$ MAR ($g/cm^2/k.y.$)	Mean Non-$CaCO_3$ MAR ($g/cm^2/k.y.$)	Mean C_{org} MAR ($mg/cm^2/k.y.$)
0	0								
9.05	0.73	75.61	0.07	12.40	0.56	0.70	0.53	0.17	0.49
11.75	0.91	66.11	0.08	15.00	0.49	0.74	0.49	0.25	0.59
12.67	0.98	80.30		13.14	0.48	0.63	0.51	0.12	
21.08	1.66	74.67	0.07	12.37	0.54	0.66	0.49	0.17	0.46
22.62	1.88	66.16		7.00	0.47	0.33	0.22	0.11	
29.70	2.47	80.15		12.00	0.65	0.78	0.63	0.15	
35.46	2.92	78.65	0.06	12.80	0.62	0.80	0.63	0.17	0.48
36.31	2.99	60.80		12.14	0.44	0.53	0.32	0.21	
37.32	3.08	65.02		11.22	0.46	0.52	0.34	0.18	
38.44	3.18	71.90		11.20	0.57	0.63	0.45	0.18	
41.25	3.40	70.56		12.77	0.55	0.71	0.50	0.21	
46.40	3.88	55.82	0.04	10.73	0.41	0.44	0.24	0.19	0.18
47.78	3.97	77.90		15.33	0.63	0.97	0.75	0.21	
50.15	4.10	69.79		18.23	0.52	0.95	0.67	0.29	
51.80	4.24			11.79					
54.47	4.40	81.12	0.03	16.69	0.63	1.06	0.86	0.20	0.32
55.87	4.47	82.58		20.00	0.66	1.32	1.09	0.23	
57.33	4.57	81.19		14.60	0.63	0.92	0.75	0.17	
61.64	4.77	84.99		21.55	0.74	1.59	1.35	0.24	
72.03	5.35	74.81	0.05	17.91	0.59	1.06	0.79	0.27	0.53
76.28	5.53	84.43	0.04	23.61	0.75	1.78	1.50	0.28	0.71
79.20	5.68	84.76		19.47	0.76	1.48	1.26	0.23	
93.20	6.42	83.71		18.92	0.77	1.46	1.22	0.24	
106.05	7.50	81.92	0.03	11.90	0.77	0.92	0.75	0.17	0.27
114.45	7.90	87.68	0.01	21.00	0.86	1.80	1.58	0.22	0.18
116.66	8.21	68.02		7.13	0.65	0.46	0.31	0.15	
117.26	8.41	62.66		3.00	0.58	0.17	0.11	0.06	
117.99	8.50	57.59		8.11	0.53	0.43	0.25	0.18	
118.99	8.71	35.97	0.05	4.76	0.40	0.19	0.07	0.12	0.10
119.26	8.80			3.00					
119.63	8.92	43.83		3.08	0.43	0.13	0.06	0.07	
128.30	9.94	63.47		8.50	0.56	0.47	0.30	0.17	

created by using laboratory densities only. Over the interval from 0 to 113.4 mbsf, a 10-point boxcar-filtered GRAPE density value from Hole 852B was used.

A velocity model was created using only laboratory velocity data collected with the DSV, which were corrected to *in-situ* conditions for changes of sound speed as a function of temperature and pressure. Because of problems with the temperature tool, the temperature gradient and bottom-water temperature from Site 849 were used for these corrections.

The accuracy of our traveltime-to-depth conversion was evaluated by generating synthetic seismograms and subsequently comparing them to the seismic record collected over the site. Synthetic seismograms were generated using the above merged velocity and density data. These data were resampled at a 1-ms sample interval (approximately 60 cm) and then used to calculate acoustic impedance and reflection coefficients and, finally, a synthetic seismogram. Density and velocity values typical of basalt (2.5 g/cm^3 and 3000 m/s, respectively) were added at the basement depth (113.4 mbsf) to generate a basement reflector in the synthetic seismogram. The model used to generate the synthetic seismogram assumes plane waves, no multiples, and no signal attenuation; this model is described in Mayer et al. (1985). The final synthetic seismogram was filtered from 70 to 250 Hz, the same filter parameters as the field record collected at Site 852.

Results

A comparison of the synthetic seismogram with the seismic profile collected at Site 852 shows a reasonable match between the two (Fig. 45). A nearly one-to-one correspondence exists between most reflectors, with the exception between reflectors 5 and 6, where the synthetic seismogram indicates two reflectors that broadly straddle the one reflector indicated on the filtered field record. An excellent match is found at the basement. This suggests that the traveltime-to-depth conversion was fairly accurate, with the average velocity to basement being accurate.

Given a fairly reasonable velocity model, the origin of some of the reflectors at Site 852 can be analyzed. We emphasize that these results are preliminary and will be undoubtedly modified after more careful analysis. Seven major reflectors or reflector packages were identified. These reflectors were selected on the basis of amplitude and lateral coherency in the seismic record in the immediate area of Site 852. We measured the two-way traveltime in the synthetic seismogram of the top and bottom of each reflector, and by using the assumed velocity model, we determined the depth range of each reflector.

Our velocity, density, and acoustic impedance models were compared to the depth ranges calculated from this traveltime to determine any changes in physical properties causing the selected seismic reflectors. All the reflectors found at Site 852 are caused by large changes in density, because the velocity profile is relatively invariate (Fig. 46). Between reflectors 5 and 6, a density minimum occurs at about 73 mbsf and a density maximum at 81 mbsf; these values correspond to the two reflectors found in the synthetic seismogram that do not directly correlate to the filtered field record. The depths (synthetic, mbsf, and mcd) and ages (based on magnetostratigraphy and biostratigraphy of Site 852; see "Sedimentation Rates" section,

Table 20. Summary of good logging data, Hole 852D.

Log type	Depth (mbsf)
Gamma-ray/ U-Th-K	0–101.3
Aluminum	0–107.6
Geochemistry	0–115.4

Note: Assumes seafloor at 3871.5 mbrf and shifted +2.1 m to match aluminum log and low carbonate value at 107 mbsf.

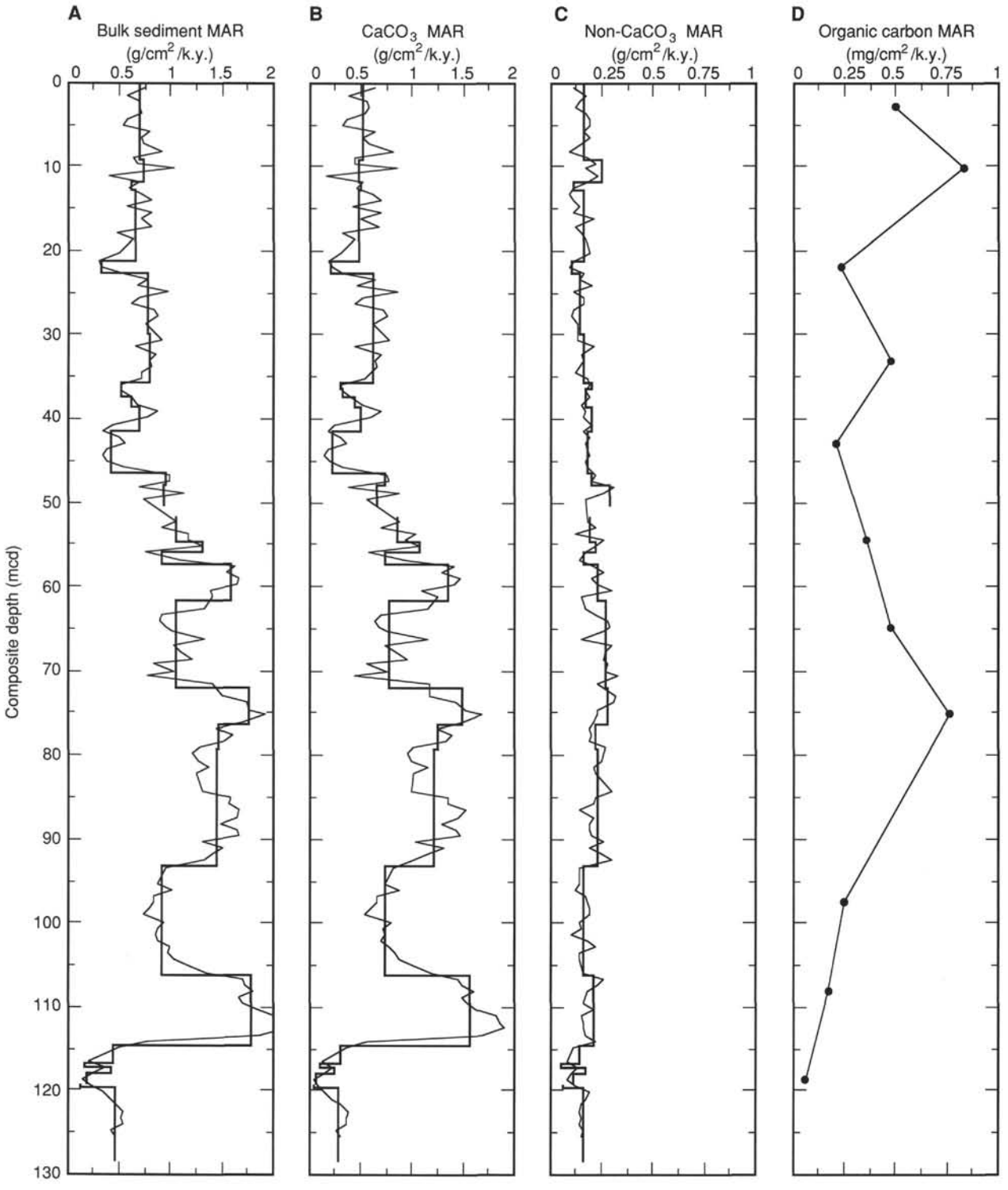

Figure 30. Mass accumulation rates of bulk sediment (**A**), $CaCO_3$ (**B**), non-$CaCO_3$ (**C**), and C_{org} (D) vs. composite depth at Site 852. Note different units for C_{org}. Thick line is mean value between each stratigraphic datum plane (based on data in Table 11); thin line shows discrete accumulation rates calculated for each sample.

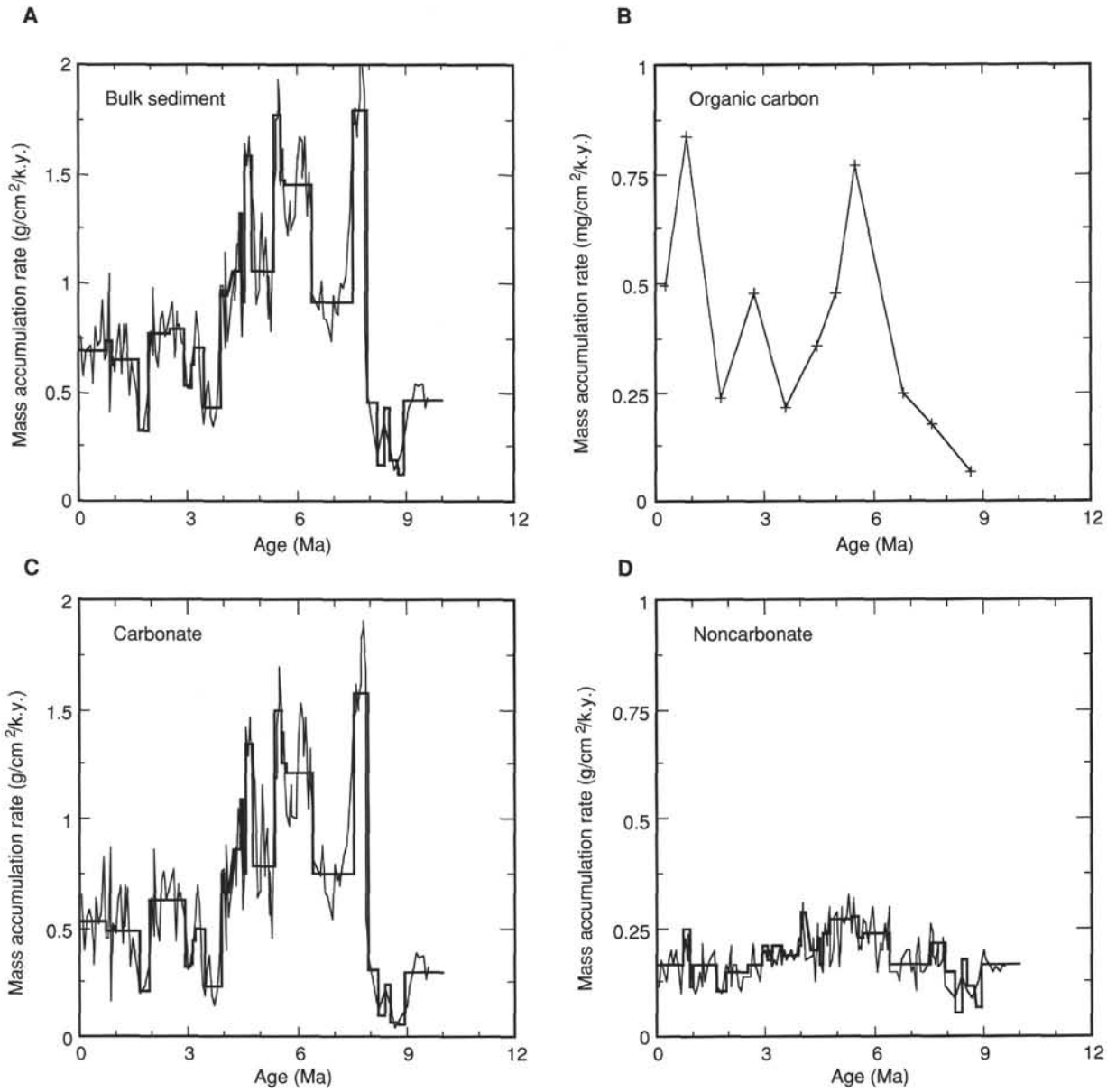

Figure 31. Accumulation rates of bulk sediment (**A**), C_{org} (**B**), $CaCO_3$ (**C**), and non-$CaCO_3$ (**D**) vs. age in sediments from Site 852. Thick line is mean value between each stratigraphic datum plane; thin line shows discrete accumulation rates calculated for each sample.

this chapter) of these reflectors are presented in Table 21. A detailed understanding of the lithologic, biostratigraphic, and, ultimately, the paleoceanographic significance of these events must await shore-based studies at this time.

SUMMARY AND CONCLUSIONS

Site 852 was the fifth site drilled along Leg 138's western transect. This transect, situated along 110°W, was designed to sample the various elements of the equatorial circulation system in an area far removed from the influence of the eastern boundary of the Pacific Ocean. The transect also serves as the eastern end-member of a series of studies (Legs 85 and 130) aimed at understanding the regional and global responses of the equatorial Pacific Ocean to changes in climate. The present location of Site 852 is near the boundary between the westward-flowing SEC and the eastward-flowing NECC. The site was selected to provide a late Neogene history of the interaction between these currents.

Site 852 is located about 900 km west of the East Pacific Rise, on crust that was generated about 11 or 12 Ma. The backtracked path of the site is straightforward and is constrained only by the movement of the Pacific Plate. Poles of rotation of the Pacific Plate were estimated on the basis of traces of hot spots (Duncan and Claque, 1985) and also by using the age distribution of sediments from DSDP sites along the equatorial sediment bulge (van Andel et al., 1975; see Fig. 2, Table 22). While the backtracked paths for Site 852 differ, depending on which of these poles of rotation is used, neither of the reconstructions shows Site 852 crossing under the equator. Thus, Site 852 is the first of the western transect sites presently north of the equator that has not passed under the equatorial divergence.

From an original ridge-crest depth of approximately 2800 m, Site 852 has subsided to its present-day depth of 3872 m and, in doing so, has

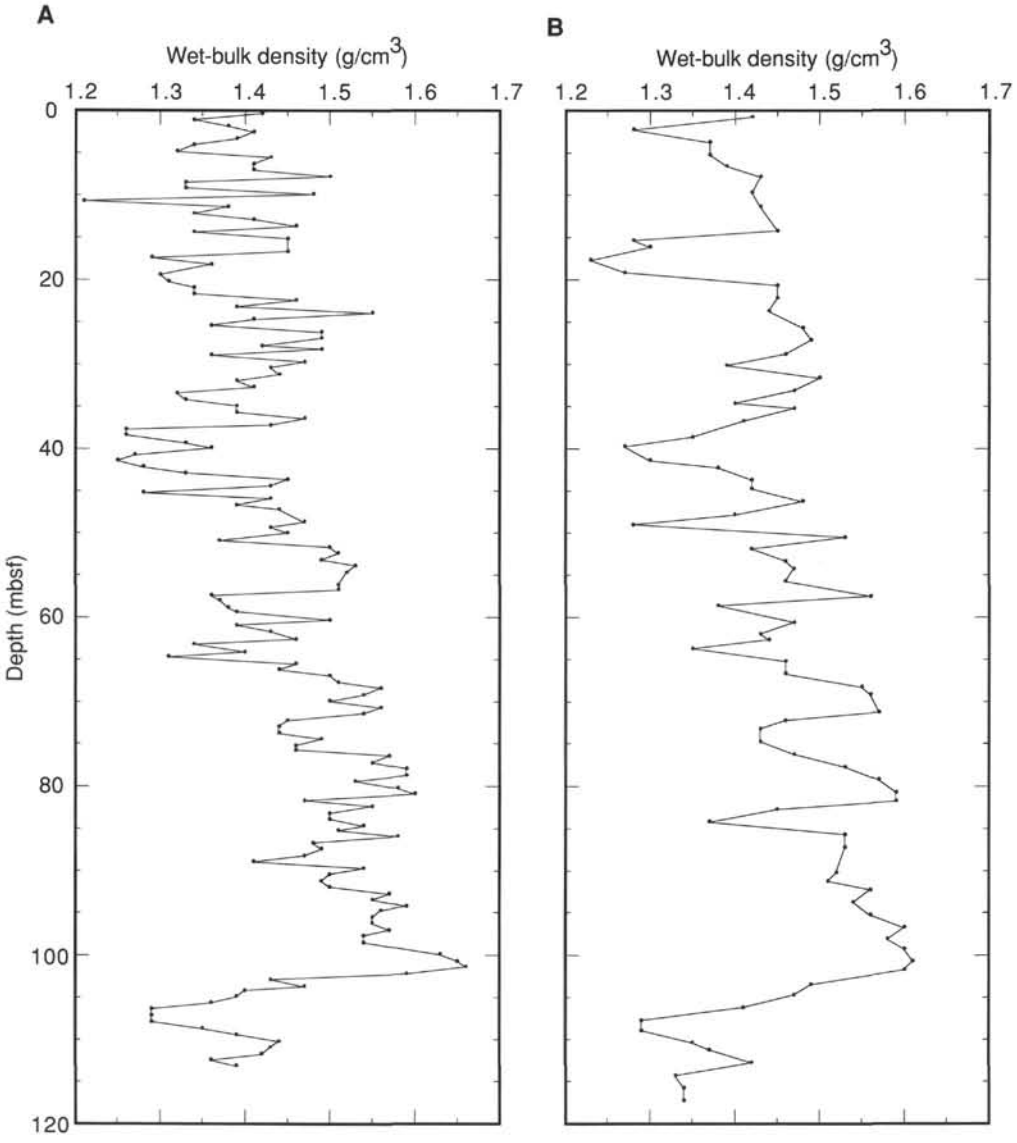

Figure 32. Plot of wet-bulk density vs. depth. **A.** Hole 852B. **B.** Hole 852C.

Table 21. Summary of traveltimes, depths, and ages for Site 852 reflectors.

Reflector	Traveltime (s)	Synthetic depth (m)	Depth (mbsf)	Depth (mcd)	Age (Ma)
R1	0.015	11.00	10.60	10.85	0.88
	0.019	14.10	14.10	14.35	1.12
R2	0.036	27.00	27.90	30.30	2.52
	0.048	36.00	35.90	38.30	3.17
R3	0.054	40.50	41.00	43.85	3.70
	0.061	45.80	43.50	46.35	3.88
R4	0.067	50.20	49.10	54.05	4.37
	0.073	54.80	52.20	57.15	4.56
R5	0.087	65.30	65.20	71.05	5.30
	0.092	69.00	66.40	73.15	5.40
R6	0.119	89.30	88.90	98.90	6.89
	0.122	91.50	90.70	100.70	7.05
R7	0.132	99.10	101.80	112.80	7.82
	0.137	103.00	107.00	119.20	8.78

Table 22. Backtracked path for Site 852.

Age (Ma)	Latitude (-°S; +°N)	Longitude (°W)
1	5.05	109.25
2	4.80	108.51
3	4.56	107.76
4	4.31	107.01
5	4.07	106.27
6	3.84	105.52
7	3.60	104.77
8	3.37	104.02
9	3.14	103.27
10	2.92	102.52
11	2.70	101.76
12	2.48	101.01
13	2.26	100.26
14	2.05	99.50
15	1.84	98.75

Note: Calculated using pole of rotation: 0–12 Ma; 67.0° N-59.0° W; angular velocity; 0.84/m.y.

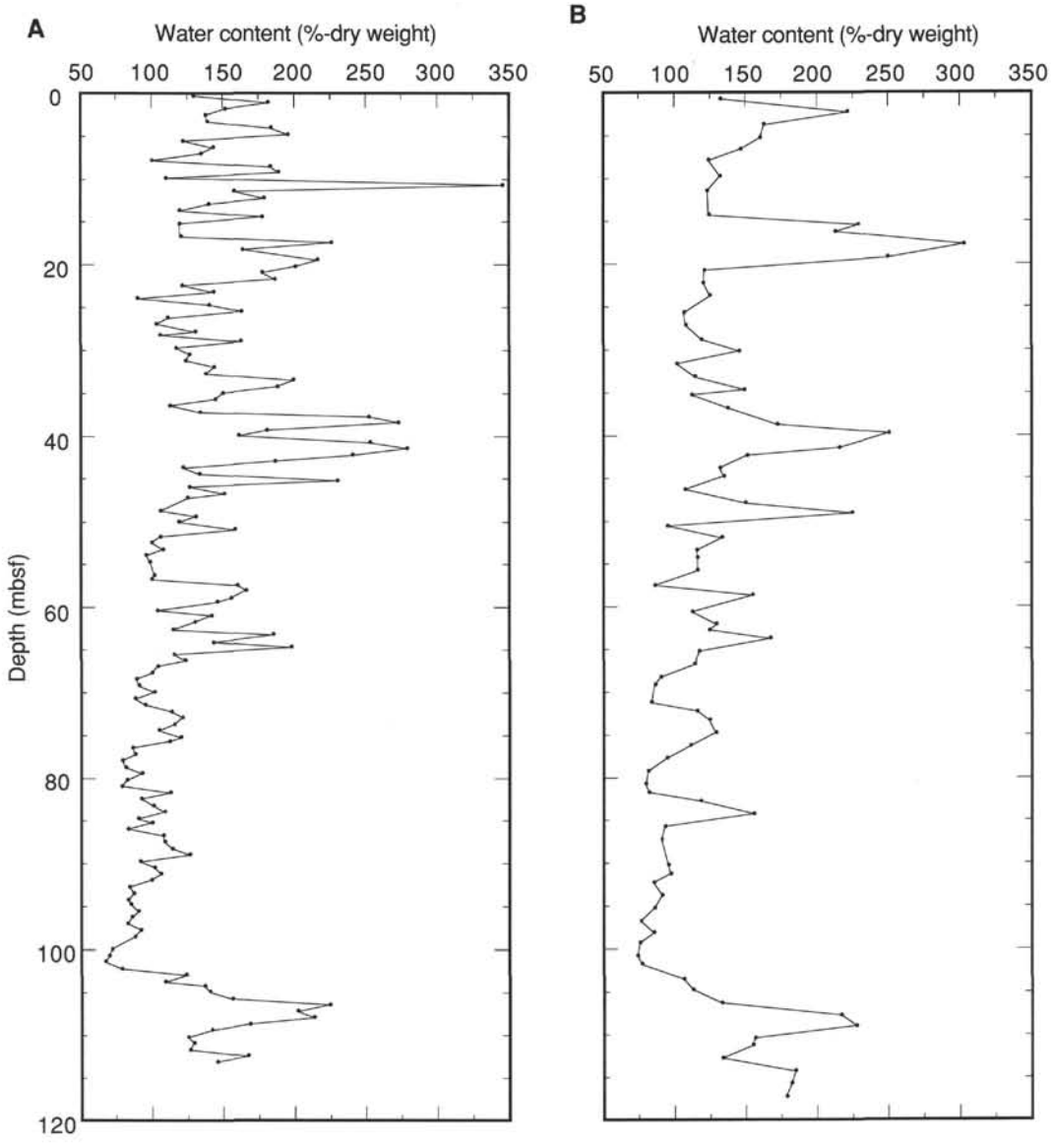

Figure 33. Plot of water content (% dry weight) vs. depth. **A.** Hole 852B. **B.** Hole 852C.

intercepted a regionally and temporally variable lysocline. The combination of triple APC- and double XCB-coring, in conjunction with the real-time monitoring of continuous core logs (GRAPE, susceptibility, and color reflectance data) has assured the continuous recovery of a 117-m-thick section. While no basement was recovered in the deepest XCB cores, we did encounter hard material in these cores at the seismically predicted depth of the basement; thus, we assume that the hole did reach basement. The sedimentary sequence spans the interval from the uppermost middle Miocene to the Pleistocene and can be described as a single lithological unit composed of varying mixtures of foraminifer nannofossil ooze, nannofossil foraminifer ooze with oxide-rich beds, and radiolarian nannofossil ooze.

Stratigraphic control at Site 852 was provided by all four of the chief planktonic microfossil groups and by an excellent magnetostratigraphy. In the upper 80 m, all reversals from the Bruhnes Chron to the top of Chron C3A were recognized, while in the lower part of the section, reversals from the upper part of Chron C4A to the top of Chron 5 were identified. Only the interval from about 6 to 8 Ma (80–110 mbsf) had magnetic intensities too low to provide a recognizable stratigraphy from shipboard analyses. This same interval also has an extremely low susceptibility signal (Fig. 47B), probably the result of dilution by calcium carbonate.

While the general shape of the sedimentation-rate curve at Site 852 (Fig. 47A) is similar to that of the previous western transect sites, rates are much lower in magnitude, and the distribution of microfossil constituents is different, which reflects the position of the site north of the equatorial high-productivity zone.

The first sediment to accumulate above the newly formed Site 852 was a radiolarian-rich nannofossil ooze that contained a substantial component of iron-oxides and clays. Initial sedimentation rates at the site were around 8 m/m.y (Fig. 47A), substantially lower than the 50 m/m.y. seen at Site 851, 380 km to the south. As with many sites in the equatorial region, sedimentation and mass accumulation rates decreased after 10 Ma. Between 10 and 8 Ma, sedimentation rates were as low as 3 m/m.y. The low carbonate contents (Fig. 47C) and relatively high percentage of radiolarians in this interval suggest that this was a time of increased dissolution of calcium carbonate. Again, this event appears to coincide with similar events seen at all Leg 138 sites and may represent a major carbonate dissolution event within the Pacific Ocean.

At about 8 Ma, an increase in sedimentation rates to around 21 m/m.y. occurred, which is reflected in a large increase in the MARs of calcium carbonate, but only a small increase is seen in the accumulation rate of noncarbonates (see Fig. 31). Sedimentation and accumulation rates

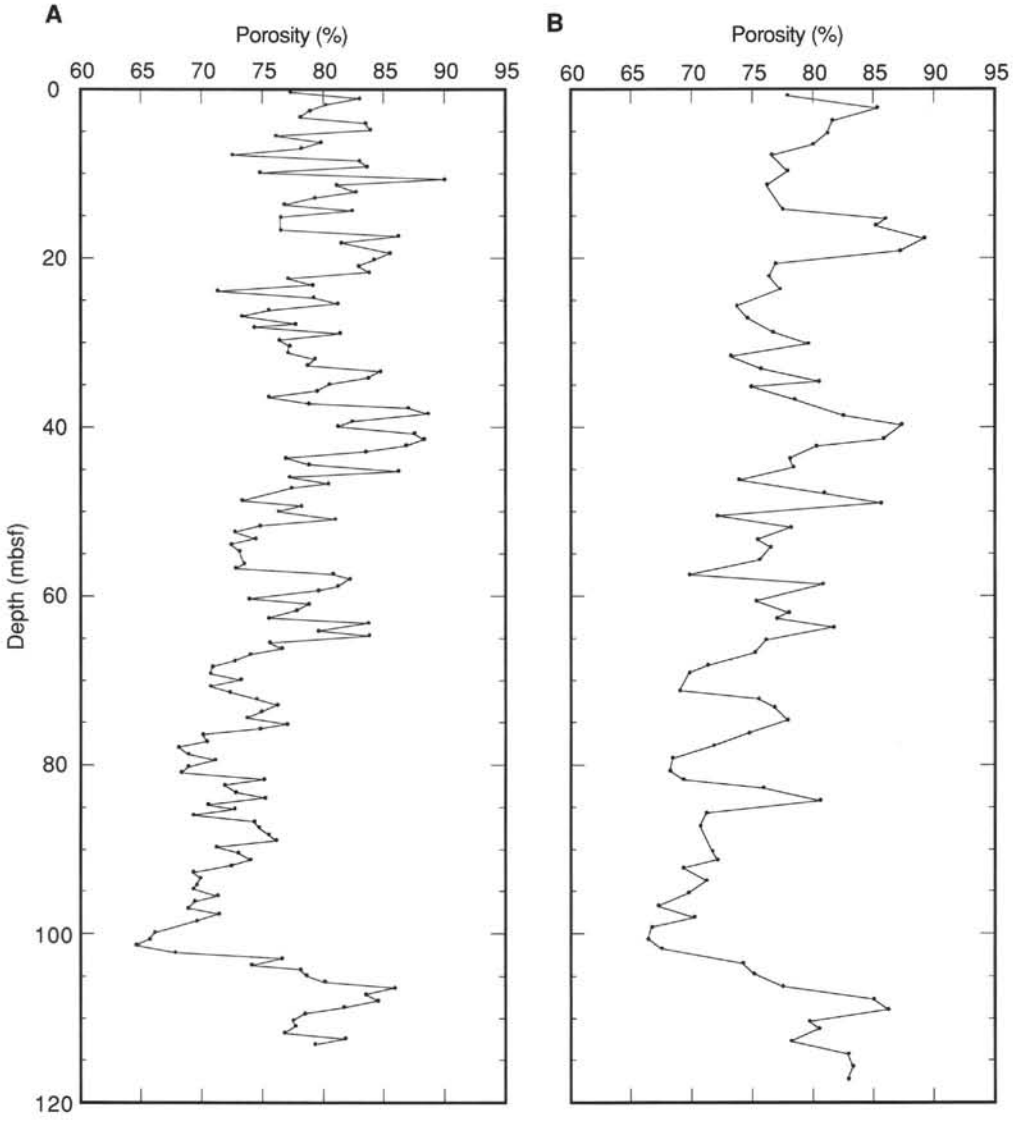

Figure 34. Plot of porosity vs. depth. **A.** Hole 852B. **B.** Hole 852C.

decline after this time (between 7.5 and 6.5 Ma), but carbonate contents remain high (Fig. 47C) through this interval, with the dominant sedimentary component being nannofossil ooze.

At about 6 Ma, the abundance of radiolarians decreased sharply. This decline in biogenic silica abundance was coincident with the movement of the site out from under the NECC and into the North Equatorial Current, assuming that present-day oceanographic boundaries apply to the late Miocene. From this point on in the history of Site 852, abundances of biogenic opal remained relatively low.

During the Pliocene and Pleistocene, sedimentation rates decreased to about 12 m/m.y. The sediment in this interval has relatively high abundances of foraminifers, greater than those seen at any other Leg 138 site. We attributed this to the relatively low flux of biogenic opal and organic carbon in the region that limited both the dilution and dissolution of carbonate.

The low organic carbon influx at Site 852 clearly is reflected in the interstitial-water chemistry, which suggests that on a macro-scale, the sediment column at Site 852 has been oxidizing throughout. Alkalinity does not change, suggesting that dissolution has been confined to the sediment/water interface, where oxygen and nitrate are being consumed to oxidize organic matter. With the relatively low sedimentation and organic carbon accumulation rates present at Site 852, all of the labile organic matter was consumed before burial.

Superimposed on these general long-term trends in sedimentation are high-frequency fluctuations in the ratios of carbonate, silica, and clay abundances. Whether these fluctuations are a response to changes in the surface current regime (and thus local) or the result of more regional changes in bottom-water chemistry will be the subject of shore-based studies. The similarity of these high-frequency variations (as expressed in the near-continous GRAPE records) between Site 852 and Site 848 (which also has never entered the high-productivity equatorial divergence zone), however, implies that the signal we are seeing represents regional carbonate dissolution events.

REFERENCES

Baker, P. A., 1986. Pore water chemistry of carbonate-rich sediments, Lord Howe Rise, Southwest Pacific Ocean. *In* Kennett, J. P., von der Borch, C. C., et al., *Init. Repts. DSDP,* 90: Washington (U.S. Govt. Printing Office), 1249–1256.

Baker, P. A., Gieskes, J. M., and Elderfield, H., 1982. Diagenesis of carbonates in deep-sea sediments-evidence from Sr/Ca ratios and interstitial dissolved Sr^{2+} data. *J. Sediment. Petrol.,* 52:71–82.

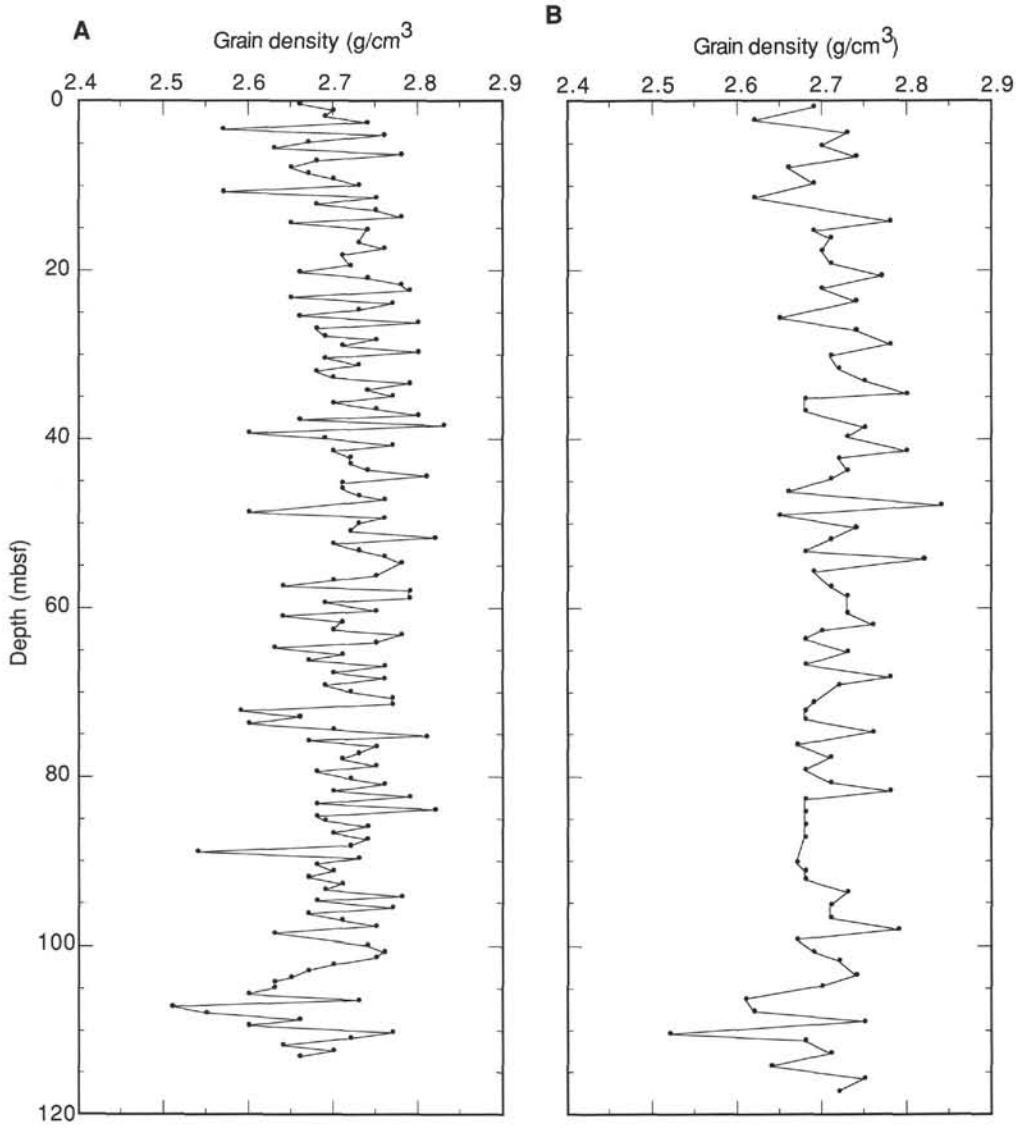

Figure 35. Plot of grain density vs. depth. **A.** Hole 852B. **B.** Hole 852C.

Duncan, R., and Clague, D., 1985. Pacific plate motion is recorded by linear volcanic chains. *In* Nairn, A.E.M., Stehli, F. G., and Uyeda, U. (Eds.), *The Ocean Basins and Margins* (Vol. 7A): New York (Plenum), 89–121.

Elderfield, H., and Gieskes, J. M., 1982. Sr isotopes in interstitial waters of marine sediments from Deep Sea Drilling Project cores. *Nature,* 333:493–497.

Froelich, P. N., Klinkhammer, G. P., Bender, M. L., Heath, G. R., Luedtke, N., Cullen, D., Daulphin, P., Hammond, D., Hartman, B., and Maynard, V., 1979. Early oxidation of organic matter in pelagic sediments of the Eastern Equatorial Atlantic: suboxic diagenesis. *Geochim. Cosmochim. Acta,* 43:1075–1090.

Gieskes, J. M., Elderfield, H., and Palmer, M. R., 1986. Strontium and its isotopic composition in interstitial waters of marine carbonate sediments. *Earth Planet. Sci. Lett.,* 77:229–235.

Johnson, D. A., and Nigrini, C. A., 1985. Synchronous and time-transgressive Neogene radiolarian datum levels in the equatorial Indian and Pacific Oceans. *Mar. Micropaleontol.,* 9:489–523.

Kastner, M., 1981. Authigenic silicates in deep-sea sediments: formation and diagenesis. *In* Emiliani, C. (Ed.), *The Sea* (Vol.7): *The Oceanic Lithosphere:* New York (Wiley), 915–980.

McDuff, R. E., 1981. Major cation gradients in DSDP interstitial waters: the role of diffusive exchange between seawater and the upper ocean crust. *Geochim. Cosmochim. Acta,* 45:1705–1713.

Mammerickx, J., 1989. *The Eastern Pacific Ocean and Hawaii.* Geol. Soc. Am., Geol. of North Am. Ser., Plate 1C.

Martini, E. 1971. Standard Tertiary and Quaternary calcareous nannoplankton zonation. *Proc. 2nd Conf. Planktonic Microfossils, Roma 1970.* Rome (Ed. Tecnoscienza), 739–785.

Mayer, L. A., 1979. The origin of fine scale acoustic stratigraphy in deep-sea carbonates. *J. Geophys. Res.,* 804:6177–6184.

Mayer, L. A., Shipley, T. H., Theyer, F., Wilkens, R. W., and Winterer, E. L., 1985. Seismic modelling and paleoceanography at DSDP Site 574. *In* Mayer, L. A., Theyer, F., Thomas, E., et al., *Init. Repts. DSDP,* 85: Washington (U.S. Govt. Printing Office), 947–970.

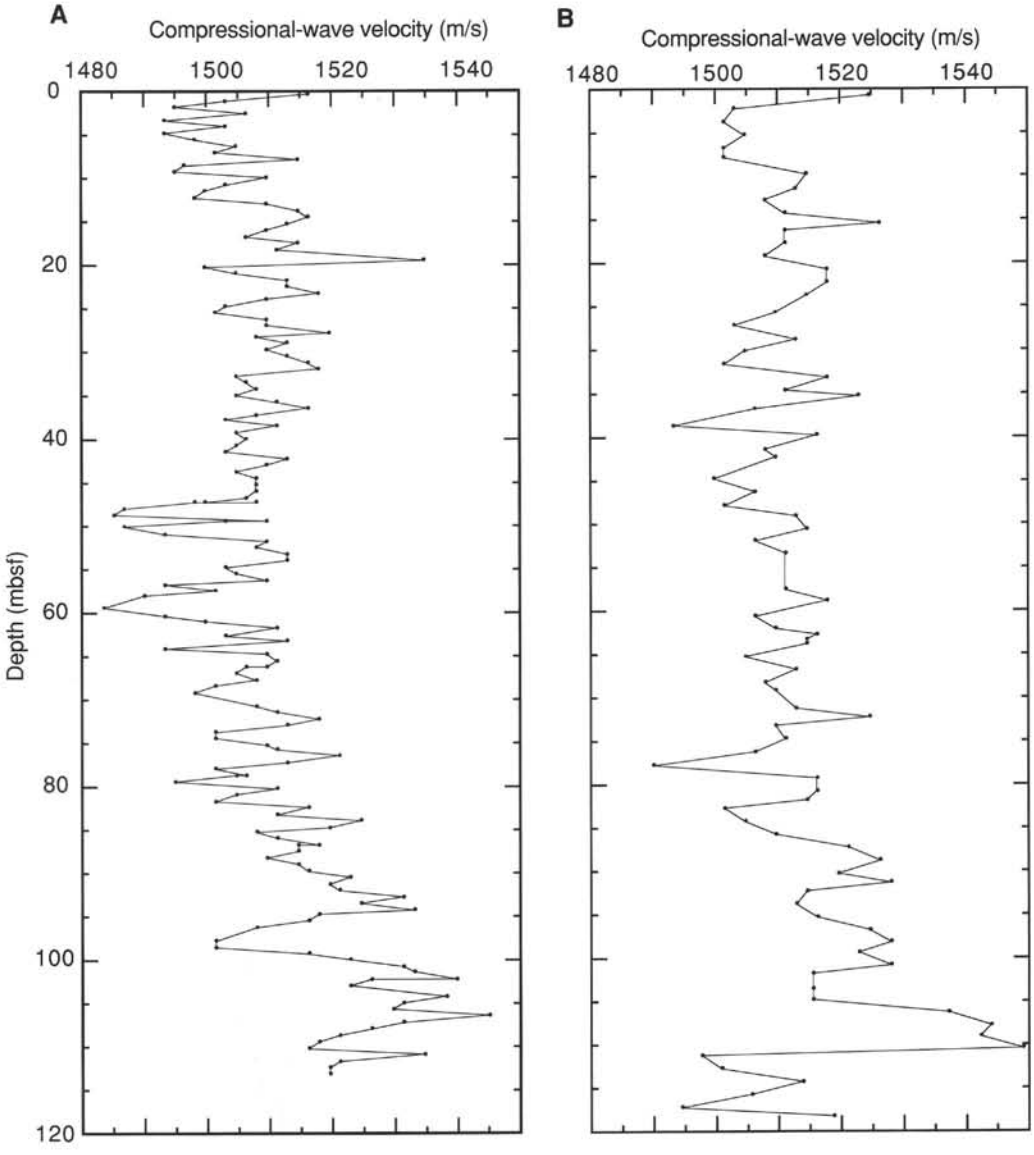

Figure 36. Plot of compressional-wave velocity vs. depth. **A.** Hole 852B. **B.** Hole 852C.

Okada, H., and Bukry, D., 1980. Supplementary modification and introduction of code numbers to the low-latitude coccolith biostratigraphic zonation (Bukry, 1973; 1975). *Mar. Micropaleontol.,* 5:321–325.

Pedersen, T. F., and Shimmield, G. B., 1991. Interstitial water chemistry, Leg 117: contrasts with the Peru Margin. *In* Prell, W. L., Niitsuma, N., et al., *Proc. ODP, Sci. Results,* College Station, TX (Ocean Drilling Program), 117:499–513.

Suess, E., von Huene, R., et al., 1988. *Proc. ODP, Init. Repts.,* 112: College Station, TX (Ocean Drilling Program).

van Andel, T. H., Heath, G. R., and Moore, T. C., Jr., 1975. Cenozoic tectonics, sedimentation, and paleoceanography of the central equatorial Pacific. *Mem.—Geol. Soc. Am.,* 143.

Ms 138A-117

NOTE: For all sites drilled, core description forms ("barrel sheets") and core photographs have been reproduced on coated paper and can be found in Section 8, beginning on page 1099. Forms containing smear-slide data can be found in Section 9, beginning on page 1435.

Formation microscanner images for this site are presented on microfiche in the back of Part 2.

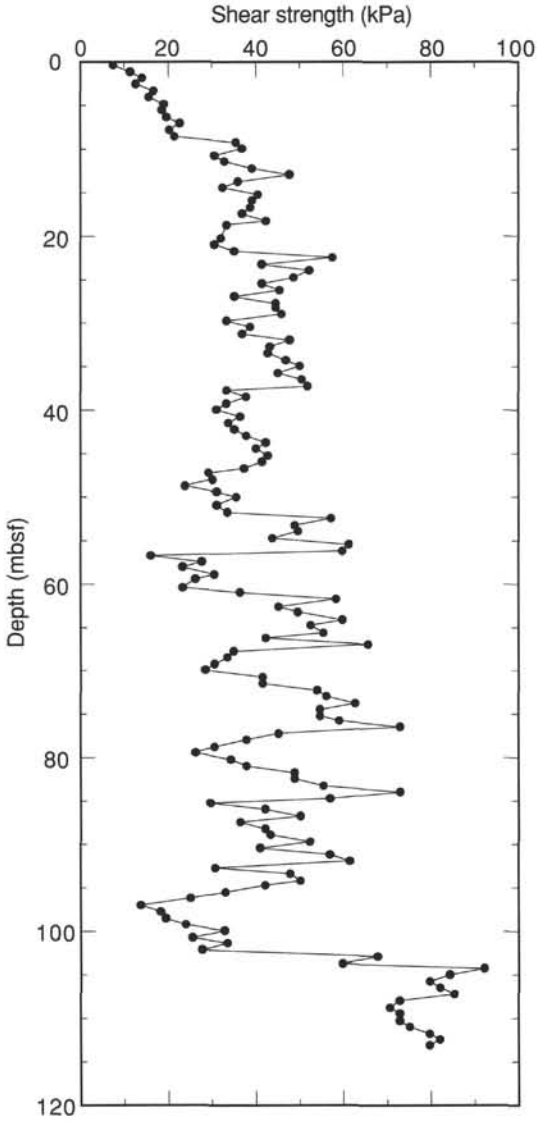

Figure 37. Plot of undrained shear strength vs. depth, Hole 852B.

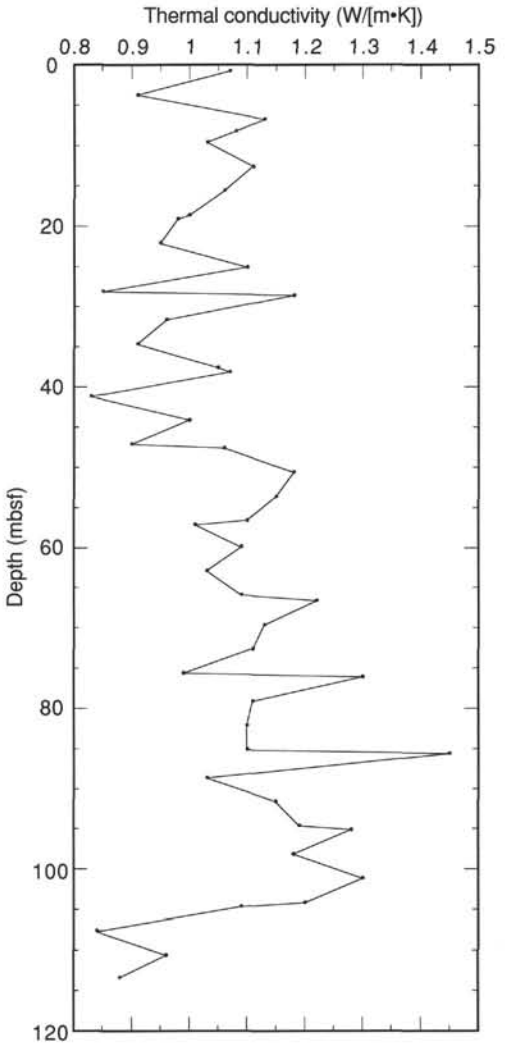

Figure 38. Plot of thermal conductivity vs. depth, Hole 852B.

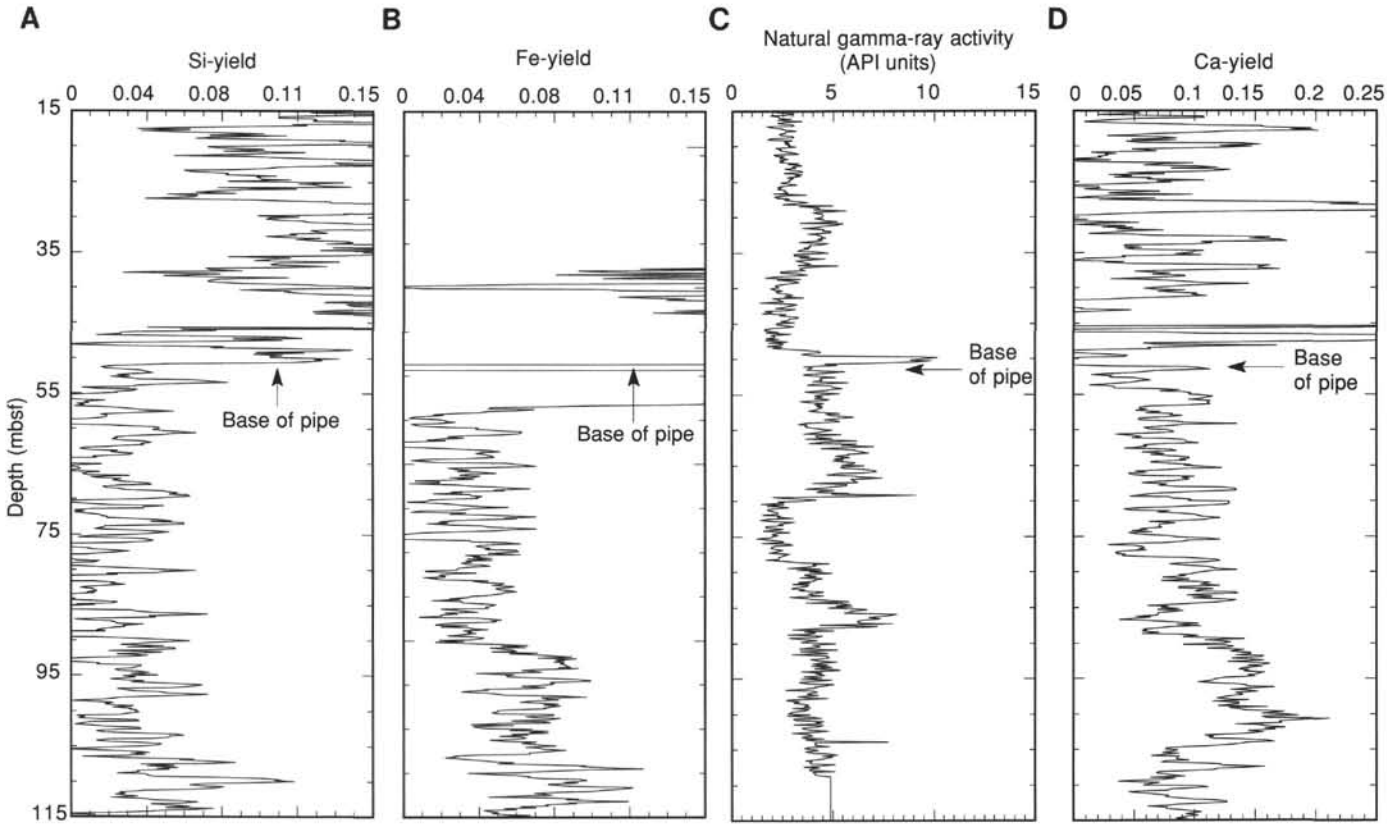

Figure 39. Profiles in Hole 852D of Si-yield (**A**), Fe-yield (**B**), natural gamma-ray activity (**C**), and Ca-yield (**D**). Base of pipe is located at 52 mbsf in these plots.

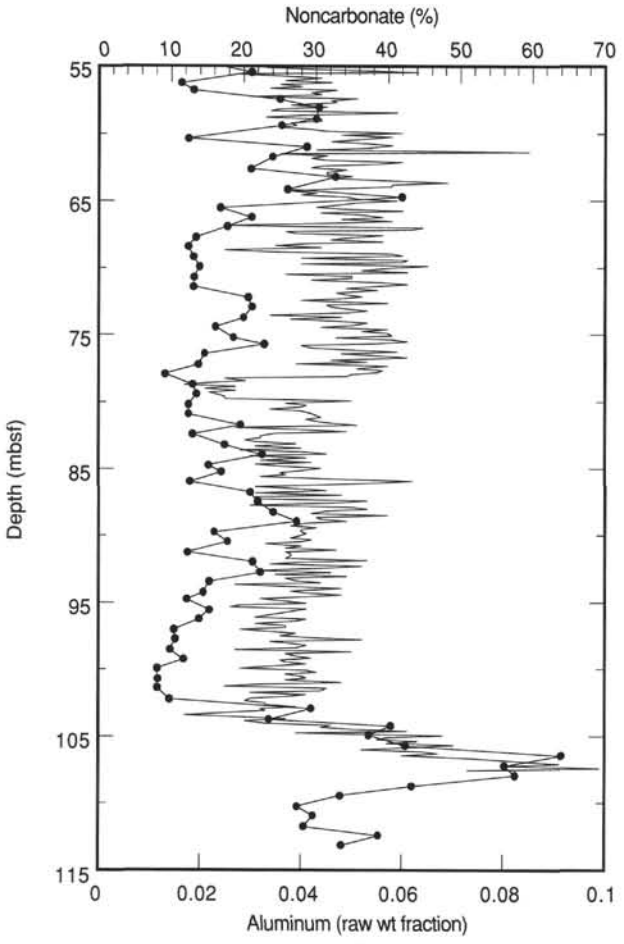

Figure 40. Comparison of noncarbonate percentage from shipboard calcite measurements (line with solid circles) with Al log (thin solid line). We used the peak centered at 106 mbsf to depth-shift log data by +2.1 m to match core.

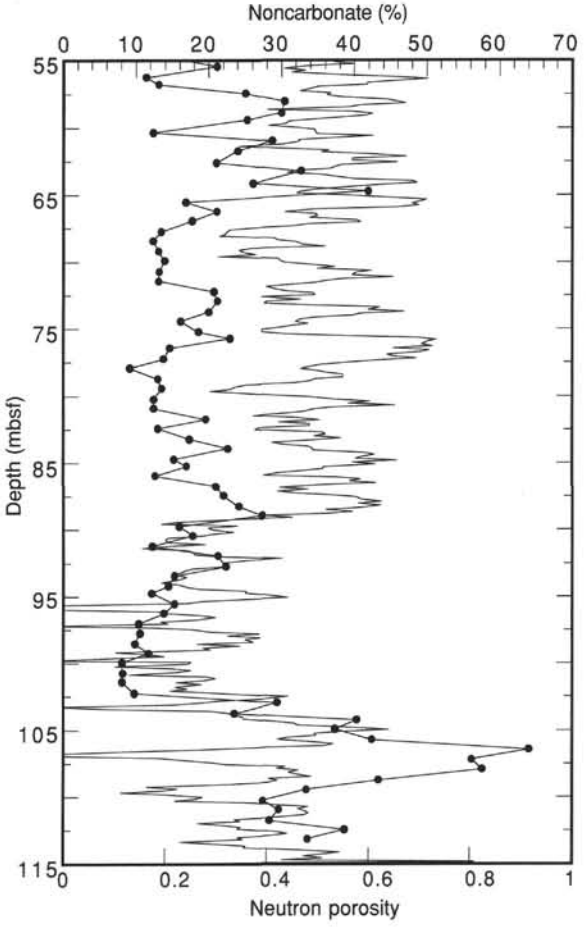

Figure 41. Comparison of noncarbonate fraction (solid line with dots) to uncalibrated neutron porosity from GST log (thin line). A reasonable correlation should be seen between the two profiles because low calcite correlates with high water content in shipboard measurements. Zero porosity measurements deep in core represent poor data intervals for the GST. Dropout at about 107 mbsf may have affected chemical yields from tool.

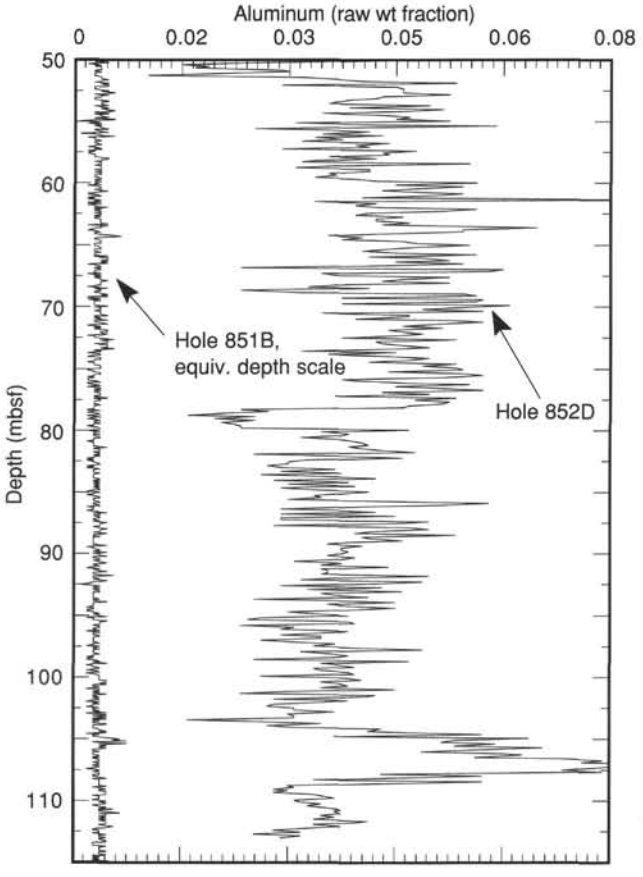

Figure 42. Comparison of Al contents in Hole 852D with those in Hole 851B in the detailed equatorial transect. Sedimentary Al contents are about an order of magnitude higher at Site 852 than at equatorial sites.

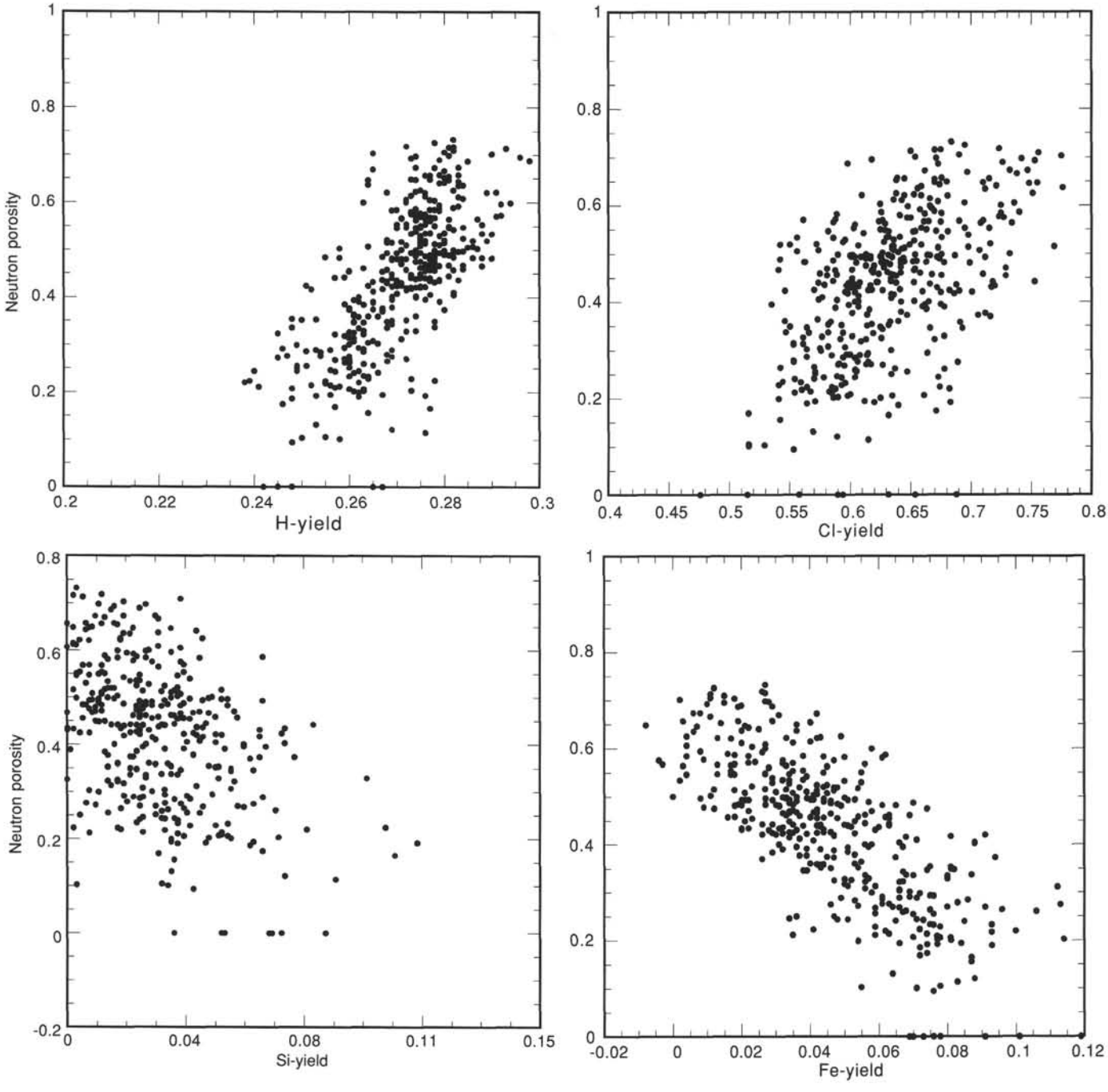

Figure 43. Crossplots of chemical yields from GST tool compared to neutron porosity. A positive correlation should exist between porosity and chemical yield for all these elements. Negative correlations for Fe and Si represent porosity effects on chemical yields for these elements.

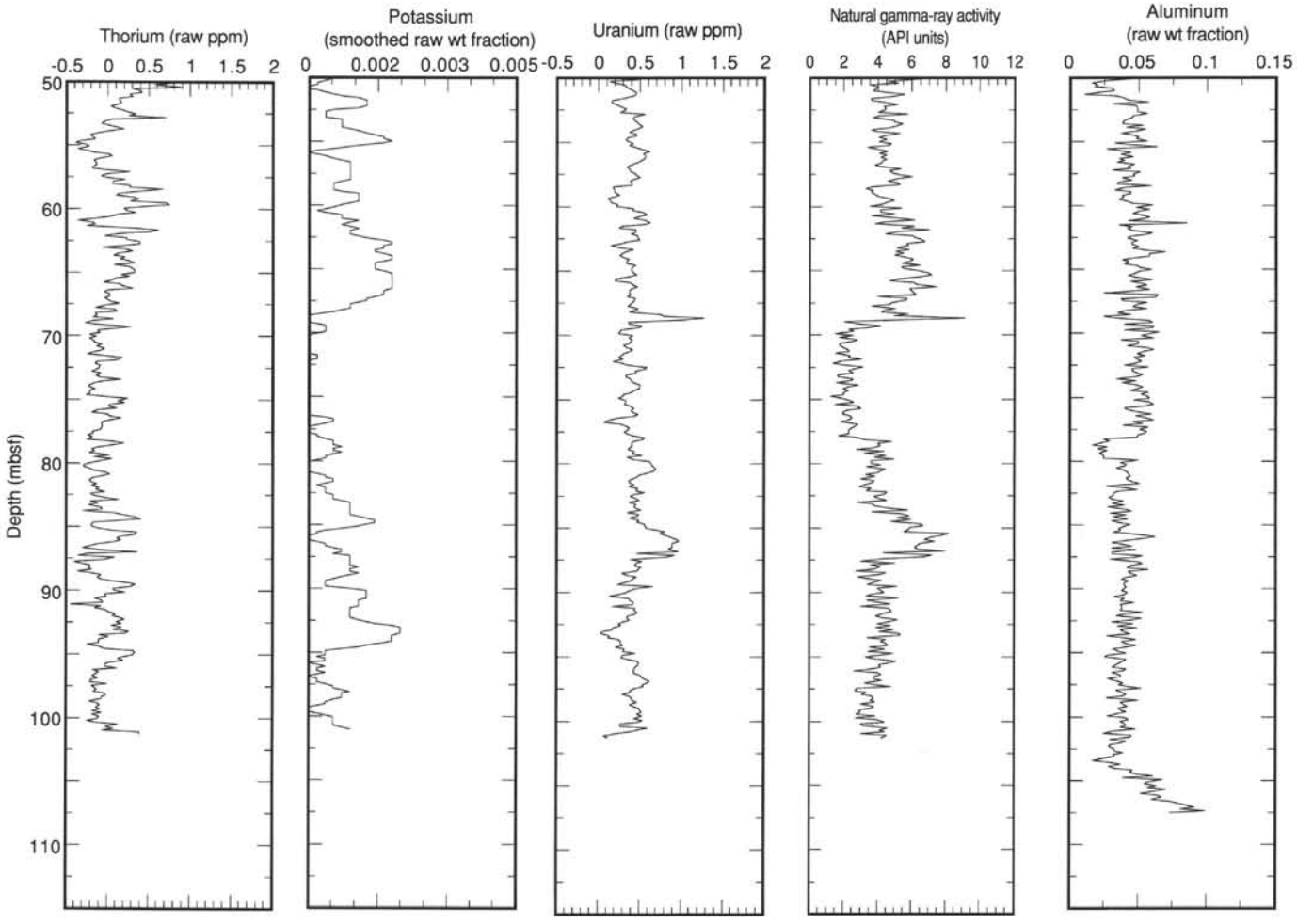

Figure 44. Concentrations of elements (Th, K, and U) and total natural gamma-ray activity from the NGT, compared to concentrations of aluminum from the ACT. Absence of correlation among the profiles underscores that at Site 852, the noncarbonate fraction was a complex, temporally variable mixture of clays, opal, and other material.

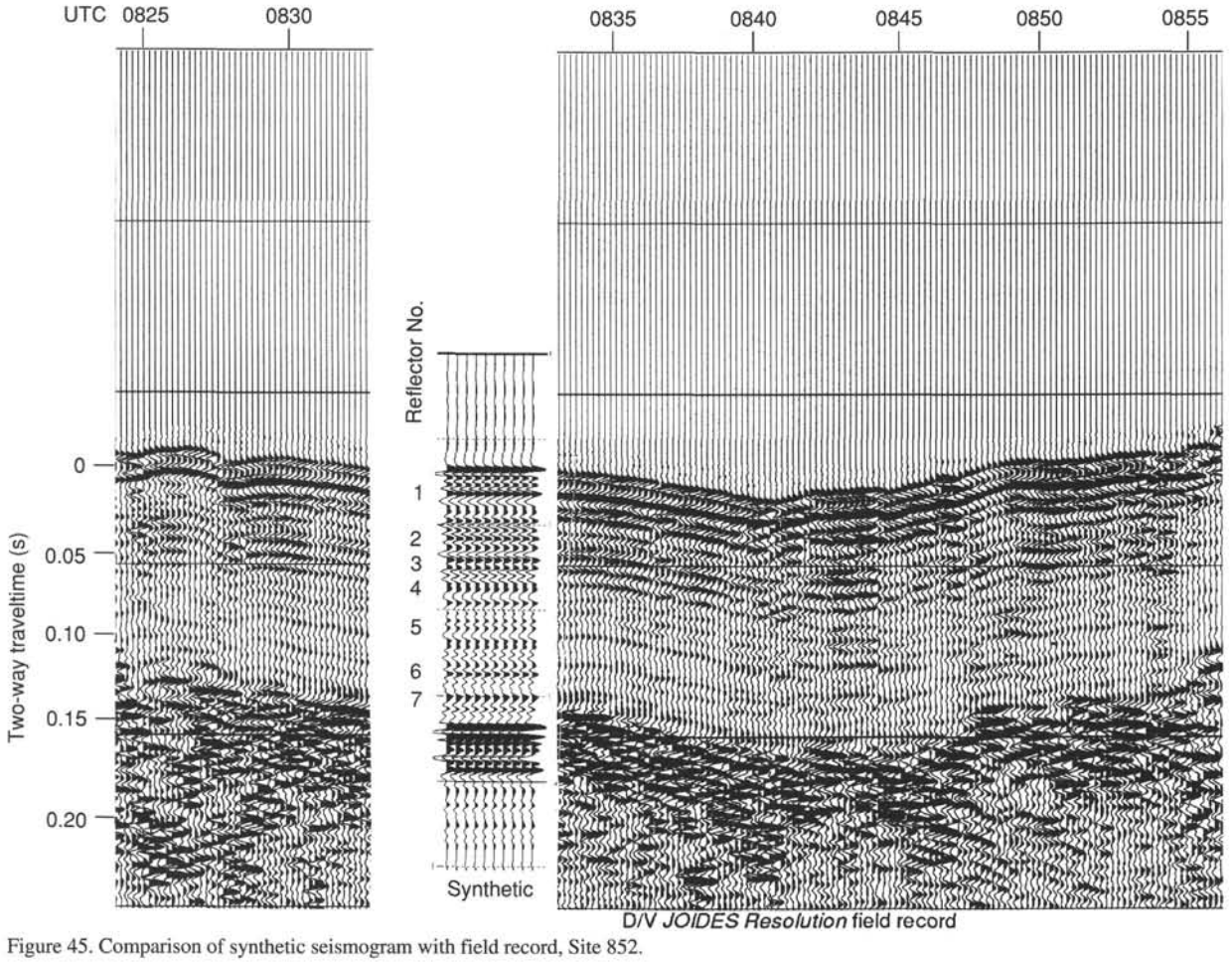

Figure 45. Comparison of synthetic seismogram with field record, Site 852.

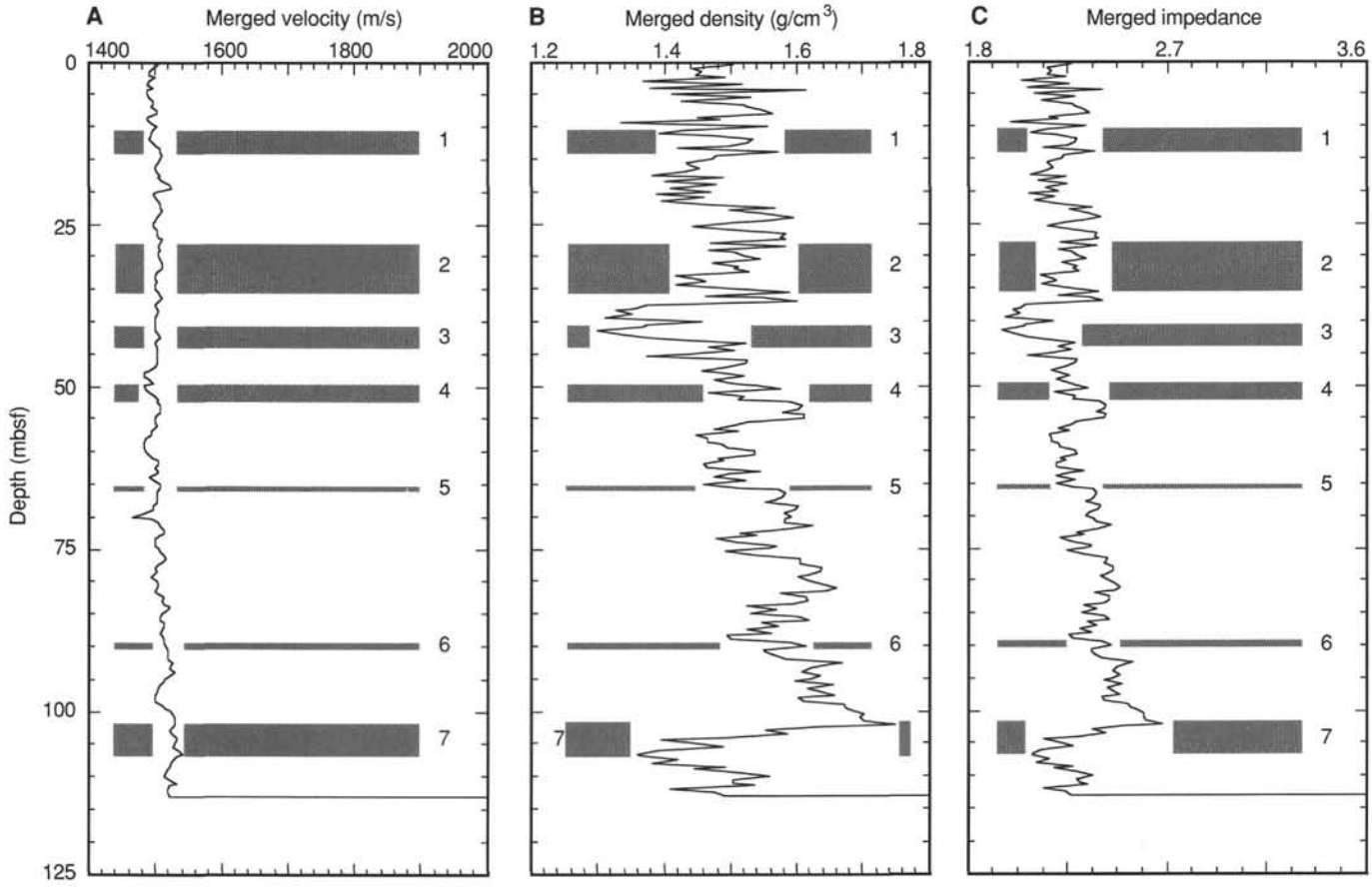

Figure 46. Velocity (**A**), density (**B**), and acoustic impedance (**c**) data used for generating Site 852 synthetic seismograms. Seven reflectors selected from synthetic seismogram are shown for comparison.

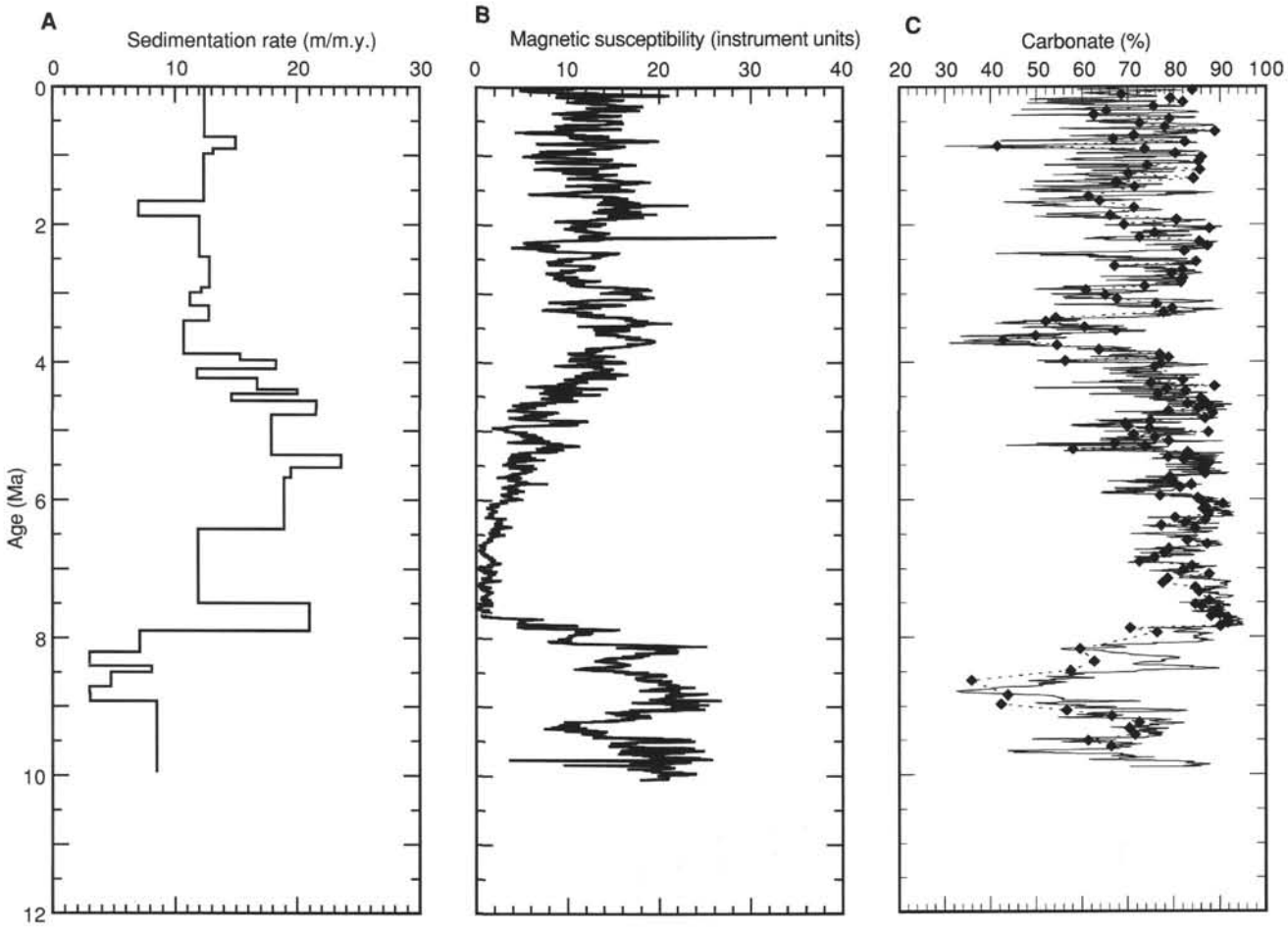

Figure 47. **A.** Sedimentation rate vs. age. **B.** Sediment magnetic susceptibility vs. age. **C.** Predicted (solid line) and measured carbonate content (dashed line with symbols) vs. age.

Hole 852D: Natural Gamma Ray Log Summary

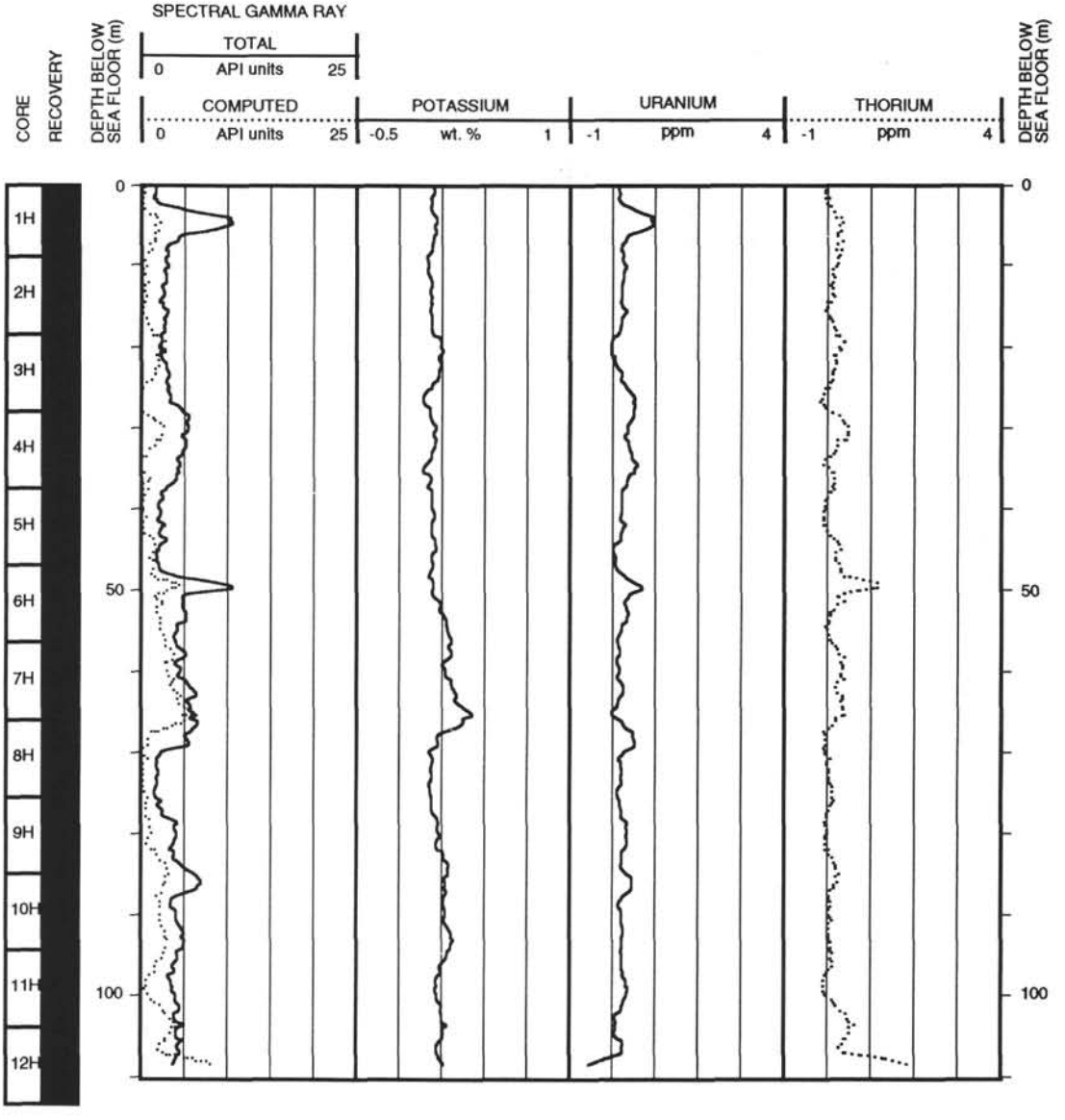

Hole 852D: Geochemical Log Summary